MASS TRANSFER AND MERGERS IN DOUBLE WHITE DWARF BINARIES.

A Dissertation

Submitted to the Graduate Faculty of the
Louisiana State University and
Agricultural and Mechanical College
in partial fulfillment of the
requirements for the degree of
Doctor of Philosophy

in

The Department of Physics and Astronomy

by
Wesley Paul Even
B.S., University of Northern Iowa, 2003
M.S., Louisiana State University, 2008
May, 2010

Dedication

For my parents, Eugene and Paula...

Acknowledgments

I would like to thank my adviser Joel Tohline for his support, guidance, and infinite patience throughout this research and my time at LSU. I would also like to thank Juhan Frank for his questions and insights, making sure that I considered the physics and didn't get lost in the computational aspects of this research. In addition, thank you to astronomy faculty members Geoff Clayton, Brad Schaeffer, Robert Hynes, and Arlo Landolt.

I would like to thank postdoctoral researchers Patrick Motl and Shangli Ou for introducing me to the codes and other computational tools that were required to conduct this research. I would also like to thank my colleagues, especially Robert Beaird, Charles Bradley, Jay Call, Andrew Collazzi, Sulakshana Thanvanthri, and Sai Vinjanampathy for their companionship and support throughout graduate school. I would also like to thank the professors and students in the IGERT on Computational Fluid Dynamics for exposing me to new fields and different ways of looking at my research, in particular my IGERT adviser Blaise Bourdin and my fellow students Luis Alvergue, Michael Crochet, Farid Harhad, Tyler Landis, and Kevin Tubbs.

I would like to thank the physics professors at the University of Northern Iowa who introduced me to physics, especially Michael Roth for initiating my computational physics research. Finally, I would like to thank my family for all their support and encouragement as I have pursued my dreams.

Table of Contents

List of Tables

List of Figures

Abstract

We have developed a self consistent field (SCF) technique similar to the one described by Hachisu, Eriguchi, & Nomoto (1986b) that can be used to construct detailed force-balanced models of synchronously rotating, double white dwarf (DWD) binaries. This SCF technique can be used to construct model sequences that mimic the last portion of the detached inspiral phase of DWD binary evolutions, and semi-detached model sequences that mimic a phase of conservative mass transfer. In addition, the SCF models can be used to provide quiet initial starts for dynamical studies of the onset of mass transfer in DWD systems. We present multiple dynamical simulations of interacting DWD binaries using these improved initial models and a modified version of the hydrodynamics code developed originally by Motl et al. (2002) to investigate the stability of mass transfer and the possibility that DWD binary mergers serve as progenitors for Type Ia supernovae. These are among the first white dwarf merger simulations carried out using a grid-based hydrodynamics technique and a realistic equation of state. Where there is overlap, our results compare favorably to simulations that have been previously published by other groups but carried out using smooth particle hydrodynamics (SPH) techniques.

1. Introduction

1.1   White Dwarfs

Energy in main sequence stars, like the sun, is generated from fusion occurring in the core of the star. Main sequence stars initially fuse hydrogen into helium. If a star has enough mass it can eventually form a region where helium is fused to form carbon and oxygen. Depending on the mass of the star this fusion process can create elements up to iron. For elements with an atomic number greater than iron the fusion process absorbs thermal energy and reduces the pressure support in the interior of the star, causing the core to collapse under the force of gravity. During the burning of elements between He and Fe the outer layers of a star can expand radially and develop instabilities. This can lead to the outer layers being ejected from the star and leaving only the dense core of heavy material behind. This exposed core is no longer undergoing fusion and is called a white dwarf. Since this core was formerly the central fusion engine of the star it will be extremely hot, but also very small in size compared to a main sequence star. Typical white dwarfs have approximately the same radius as the Earth, but a mass comparable to the sun's mass. Due to this small size white dwarfs have very low luminosity despite there high temperature. The first optically resolved white dwarf, Sirus B, was seen by Alvan Clark in 1862.

The extreme densities obtained from the calculation of mass and radius from white dwarf observations indicate that white dwarfs can not be made of an ordinary gas. After fusion in the core ends the star will begin to contract because the nuclear reactions that were previously imparting energy into the star have stopped and there is no source of energy to prevent gravitational collapse. As the ionized gas compresses the electrons become so tightly packed that quantum effects begin to play a dominate role in the structure. The

Pauli exclusion principle disallows two electrons from occupying the same quantum state and in atoms this leads to the electron shell structure. In the white dwarf the exclusion principle creates a pressure as electrons require more energy to occupy the same volumes. Even if the normal agitation of the gas is ignored - that is, even if the normal gas temperature is set to zero - this degeneracy pressure can become great enough to stop the gravitational collapse and create a stable star.

Figure 1.1 graphs several relationships for "zero-temperature" white dwarfs (ZTWDs). These are calculated using a simplified 1D version of the self consistent field code described in Chapter 2. Two physical characteristics about white dwarfs can be easily seen from these figures: the size of the white dwarf decreases as the mass increases; and there is a maximum mass for white dwarfs. The reasons for this will be discussed more in §2.1.

1.2   Binary Stars

Sirius B is in a binary system with a main sequence star Sirius A, the brightest star in the night sky. Binary systems occur when 2 stars form close enough together that they are gravitationally bound and the two stars orbit around the center of mass of the system. The existence of binary stars has been known to astronomers for over 300 years. Binary systems are very common with over half of all stars being in a binary system. Binary systems allow insight into parameters that are not obtainable by observations of single stars. In particular, the masses of stars can be calculated if there are multiple stars in a system using Kepler's laws. Most binary stars interact almost exclusively through gravitational forces. However, systems can evolve to a point where matter from one star can interact directly with the other star in the system. This can occur for example, if there are strong winds off one star or if one star overfills its so called Roche lobe.

The Roche potential is the effective potential of a binary system in a circular orbit as
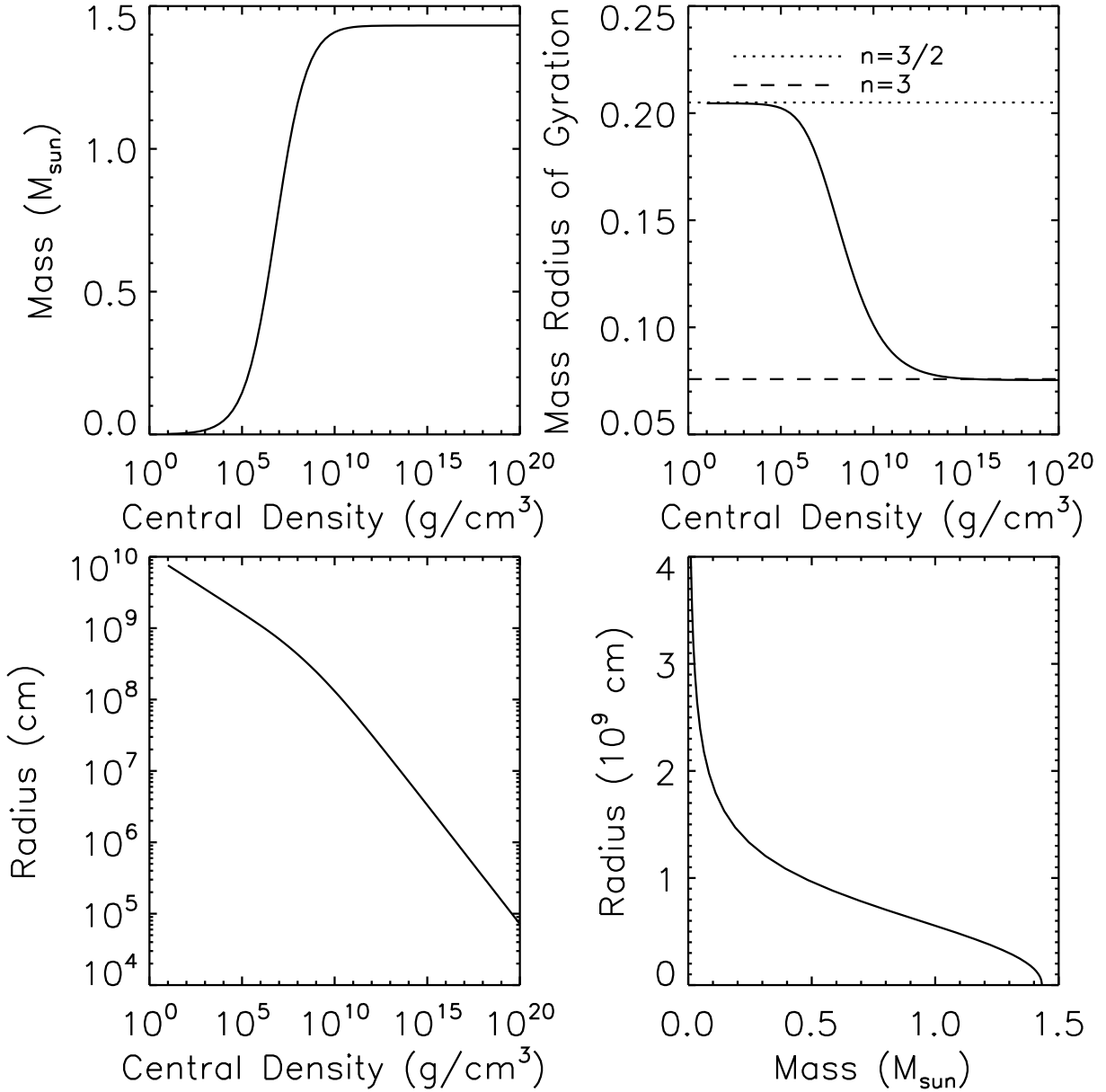
Figure 1.1 Properties of a series of single isolated non-rotating zero temperature white dwarfs. Upper left: Mass as a function of the central density. Upper right: Mass radius of gyration as a function of central density. The n=3/2 and n=3 lines represent the values for a polytropic star with a polytropic index of 3/2 and 3 respectively. Lower left: Radius as a function of central density. Lower right: Radius as a function of mass.

viewed from a frame rotating with the system's orbital frequency Ω. The equation for the Roche potential, Φ_R, for point mass stars is given by,

$$\Phi_R(\vec{r}) = -\frac{GM_1}{|\vec{r} - \vec{r_1}|} - \frac{GM_2}{|\vec{r} - \vec{r_2}|} - \frac{1}{2}\Omega^2\varpi^2, \tag{1.1}$$

where $\vec{r}$ is the position at which the potential is being evaluated, $\vec{r_1}$ is the location of the first star, $\vec{r_2}$ is the location of the second star, ϖ is the distance from the orbital axis of the binary system to the position $\vec{r}$, G is the gravitational constant, and M_1 and M_2 are the masses of the respective stars.

In Figure 1.2 equipotential contours are drawn in the equatorial plane of the binary; the final grey contour creates a figure eight shape. The volume inside this contour is known as the Roche lobe. The point of intersection of this contour has been named the first Lagrange point (L1). The L1 point is a saddle equilibrium point in the potential. Matter at this point is equally bound to both stars. If a star grows larger than its Roche lobe then it will begin to transfer mass to its companion through the L1 point.

Binary systems can be separated into three different classes based on the Roche potential. A detached system is a binary where neither star is filling its respective Roche lobe. In a semi-detached system one star (the donor) is filling it Roche lobe and transferring material to its companion (the accretor), which is not filling its Roche lobe. Contact binaries are systems where both stars have filled their Roche lobe; these can be further classified as over-contact if the stars are significantly overfilling their Roche lobe.

Stars can fill their Roche lobe through two different mechanisms: the star increases its size due to physical changes within the star, or the separation between the stars decreases, thereby reducing the size of the Roche lobe.

For main sequence stars the likely scenario for coming into contact/semi-contact is that one of the stars increases its radius to fill the Roche Lobe. This occurs when the donor leaves the main sequence and evolves onto the giant branch. Since more massive stars evolve
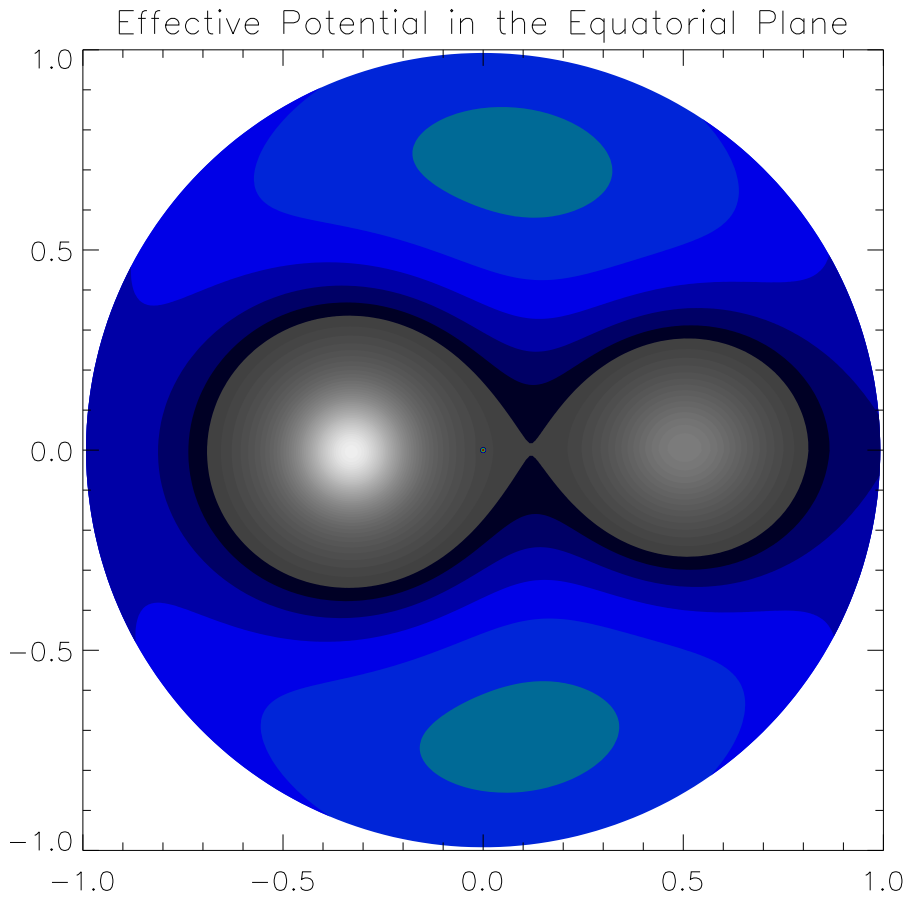
Figure 1.2 Effective Roche potential, Φ_R, in the orbital plane of a point-mass binary in a circular orbit with a mass ratio q = 2/3. The light blue contours represent the highest values of the potential, with gray going to white representing increasingly lower values of the potential. The figure 8 shaped dark gray contour represents the potential that defines the Roche lobe.

faster, the donor will be the more massive of the two stars. Eventually the outer layers of the donor can be ejected from the star, leaving behind a binary system with a main sequence star and a white dwarf. This system will no longer have Roche lobe overflow since the donor has had to decrease greatly in size to become a white dwarf, and the system will return to being a detached binary. Eventually the remaining main sequence star can also evolve to the giant branch and overflow its Roche lobe and become the new donor. During this phase material will be transfered onto the white dwarf. This class of systems is known as cataclysmic variables (CVs). After further evolution the outer layers of the new donor can be removed and a Double White Dwarf (DWD) binary system will remain.

1.3 Double White Dwarfs

Even detached DWD binaries can eventually come into contact as their separation is reduced due to the loss of angular momentum due to gravitational radiation. AM CVn systems are observed binary systems that have orbital periods of less than an hour and are blue when observed at optical wavelengths. They are also observed to be varying in brightness (Nelemans et al.2001). Based on their short periods and other observational evidence it is widely believed that AM CVn systems are semi-detached DWD binaries. The systems are theorized to have formed as detached systems that have been brought into mass transfer through gravitational wave radiation removing angular momentum from the system. There are currently 17 confirmed AM CVn systems and 2 candidate systems (Ramsey et al. 2007). While this is a relatively small number of observed systems, the number of AM CVn system in the Galaxy is calculated to be approximately 10^7.

1.4   Supernovae

Supernovae are among the most luminous astronomical events observed in the optical spectrum. Supernovae have been divided into different classifications based on their observed spectra. Type Ia supernovae have been observed to have a very predictable light curve where the decay time is strongly correlated to the maximum brightness. This makes Type Ia supernovae an excellent standard candle for determining distances. Currently there are several proposals for the progenitor systems to Type Ia supernovae. Type Ia lack hydrogen lines in there spectrum and have been observed in both young and old stellar populations where no star formation is occurring. White dwarfs will be extremely hydrogen deficient and be present in older stellar populations, but if they are isolated stars there is no mechanism available to cause them to explode and release the vast amount of energy seen in supernovae.

The leading theories for Type Ia supernovae all involve a white dwarf in a binary system. However, there is no consensus on the nature of the donor star or the chemical composition of the white dwarf (Livio 2000). The possible systems can be divided into two broad classes: double degenerate systems and single degenerate systems. In the double degenerate scenario an AM CVn system would be formed with a total mass over the Chandrasekhar mass. The Chandrasekhar mass limit, M_{Ch}, is the mass at which the electron degeneracy pressure can no longer support the star and it begins collapse due to its own gravity; for a non-rotating white dwarf this mass is approximately 1.44 $M_\odot$ (see the bottom, right-hand panel of Figure 1.1). Eventually the accretor would gain enough mass that it crosses the Chandrasekhar mass limit, either through steady accretion or rapid merger. At this point the accretor would begin to collapse. Before it collapses, rapid fusion would begin, releasing large amounts of energy. In the single degenerate case the donor would be a non-degenerate star that transfers hydrogen rich material onto the surface of the white dwarf accretor at a rate high enough to maintain steady hydrogen burning on the surface of the white dwarf. Eventually the accretor

accretes enough mass and crosses the Chandrasekhar limit resulting in a rapid fusion event as in the double degenerate case.

1.5   Previous Double White Dwarf Simulations

In an effort to understand possible progenitors of Type Ia SNe, a number of simulations of DWD binary mergers have been conducted by various groups over the last two decades. All previous simulations have been conducted using a numerical technique referred to as smoothed particle hydrodynamics (SPH). The simulations have been improved over this period with better numerical methods, more physics, and an increased number of simulation particles. However, the qualitative result of the merger has remained largely constant.

Benz et al. (1989) simulated the merger of a 0.9 $M_\odot$ and a 1.2 $M_\odot$ DWD system. The simulation was conducted using 7000 smoothed particles and non-rotating spherical white dwarfs as the initial conditions. The donor was quickly disrupted and the system merged in approximately 2.5 orbital periods. The final product of the merger was a rotating degenerate core composed mostly of material from the accretor that is surrounded by a hot semi-degenerate envelope and a non-degenerate disk.

Segretain et al. (1997) investigated the merger of a 0.6 $M_\odot$ and a 0.9 $M_\odot$ DWD binary system. Again, the initial model for the simulation was constructed by placing two non-rotating spherically symmetric stars in orbit about each other, with the donor over filling its Roche lobe. The simulation was carried out at two different resolutions: 7288 and 58,304 particles. Both simulations produced similar results. The result of the merger was an unheated uniformly rotating degenerate core surrounded by a shock heated layer. This was surrounded by an envelope of material, consisting mostly of matter from the donor. This was the hottest region in the merger and the most likely location for fusion to occur. Additionally, a rotationally supported low density disk of material forms around the merged white dwarf.

Guerrero et al. (2004) investigated 6 different binary systems ranging from a 0.4 $M_\odot$ and

$0.4 M_\odot$ system to a 0.8 $M_\odot$ and 1.0 $M_\odot$ pair. The paper focuses most of its attention on the merger of a 0.6 $M_\odot$ white dwarf with a 0.8 $M_\odot$ white dwarf. The simulations were begun with neither star initially filling its Roche lobe and a small artificial acceleration was applied to the system until mass transfer began. Approximately 50,000 particles where used in the simulations that produced configurations similar to those in Segretain et al. (1997). These simulations also included a nuclear reaction network. In the merger, fusion would begin in the shock heated region, but would quench itself and did not play a significant role in the final outcome of the merger.

Yoon et al. (2007) investigated a DWD system with a 0.6 $M_\odot$ donor and a 0.9 $M_\odot$ accretor. This simulation increased the number of particles used to 200,000 and followed the evolution for twice the time of any of the previous simulations discussed. The maximum temperature reached in the simulation was slightly above the carbon burning temperature of 10^9 K, but again the burning was limited by the expansion of the gas when heated. The final product of this merger was a slowly rotating cold core surrounded by a rapidly rotating elliptical envelope of hot material. A thick rotationally supported disk was also formed.

1.6   This Work

Here we investigate initial conditions that are closer to equilibrium than was done in the simulations discussed in Section 1.5. This is done by constructing steady state equilibrium models of synchronously rotating DWD binaries with a separation greater than a_{crit}, the separation at which one star begins to overflow its Roche lobe. These models are used to mimic the gravitational inspiral of the DWD binary and are used as initial conditions for computational fluid dynamics (CFD) simulations of mass transferring DWD systems. As described in Chapter 4, the CFD technique used here is very different from the SPH technique; it involves advecting fluid across a grid. Multiple CFD simulations are conducted

to verify our technique and to study the merger of the DWD systems as possible progenitors to type Ia supernovae.

2. Self Consistent Field Technique[1]

2.1 Zero Temperature Equation of State

The Self Consistent Field (SCF) technique was first introduced to the astrophysics community by Ostriker & Mark (1964) to create models of rapidly rotating, single stars with a polytropic equation of state. Hachisu developed a variation of the technique, improving convergence rates and extending its capabilities to include the use of a zero temperature white dwarf (ZTWD) equation of state. With his improved technique, Hachisu was able to construct two-dimensional (2D) configurations of differentially rotating, single white dwarfs (Hachisu, 1986a) and three-dimensional (3D) configurations of uniformly rotating multiple white dwarf systems in which the stars have equal mass (Hachisu, 1986b). New & Tohline (1997) employed Hachisu's 3D technique to construct inspiral sequences of equal-mass DWD binaries, including over-contact models having separations even smaller than a_{crit}. Hachisu (1986b) also applied his technique to the construction of unequal-mass binary systems using a polytropic equation of state and, after additional algorithmic innovations were introduced, Hachisu, Eriguchi, and Nomoto (1986a,b) constructed a small sample of unequal-mass DWD binaries and heavy-disk white dwarf systems to examine the likely outcome of DWD mergers. In what follows we show how Hachisu's SCF technique for constructing unequal-mass DWD binaries can be further improved and used to construct inspiral binary sequences.

---

[1]§2.1 and Chapter 3 reproduced by permission of the AAS (Even & Tohline (2009))

2.1.1 Equation of State

In the ZTWD equation of state (Chandrasekhar, 1935, 1967; Hachisu, 1986a) the electron degeneracy pressure P varies with the mass density ρ according to the relation,

$$P = A\left[x(2x^2 - 3)(x^2 + 1)^{1/2} + 3\sinh^{-1} x\right],\qquad(2.1)$$

where the dimensionless parameter,

$$x \equiv \left(\frac{\rho}{B}\right)^{1/3},\qquad(2.2)$$

and the constants A and B are (see Appendix A and Table B.1 for elaboration),

$$A \equiv \frac{\pi m_e^4 c^5}{3h^3} = 6.00228 \times 10^{22} \text{ dynes cm}^{-2},\qquad(2.3)$$

$$\frac{B}{\mu_e} \equiv \frac{8\pi m_p}{3}\left(\frac{m_e c}{h}\right)^3 = 9.81011 \times 10^5 \text{ g cm}^{-3}.\qquad(2.4)$$

According to Chandrasekhar (1967) (see again our Appendix A), a natural length scale associated with models of ZTWDs is,

$$\mu_e \ell_1 = \left(\frac{2A}{\pi G}\right)^{1/2}\frac{\mu_e}{B} = 7.71395 \times 10^8 \text{ cm} = 0.0111 R_\odot,\qquad(2.5)$$

and the associated limiting white dwarf mass is,

$$\mu_e^2 M_{\text{ch}} = 4\pi(2.01824)\left(\frac{2A}{\pi G}\right)^{3/2}\left(\frac{\mu_e}{B}\right)^2 = 1.14205 \times 10^{34} \text{ g} = 5.742 M_\odot.\qquad(2.6)$$

Throughout this work, we will assume that the average ratio of nucleons to electrons throughout each white dwarf is $\mu_e = 2$. Hence, $B = 1.96202 \times 10^6$ g cm^{-3}, $\ell_1 = 5.55 \times 10^{-3} R_\odot$, and $M_{\text{ch}} = 1.435 M_\odot$.

In terms of the enthalpy of the gas,[2]

$$H \equiv \int \frac{dP}{\rho},\qquad(2.7)$$

---

[2]As defined here, H is actually enthalpy per unit mass.

the ZTWD equation of state shown in Eq. (2.1) can also be written in the form,

$$H = \frac{8A}{B}\left[x^2 + 1\right]^{1/2}.$$ (2.8)

Inverting this gives the dependence of ρ on H, namely,

$$\frac{\rho}{B} = x^3 = \left[\left(\frac{BH}{8A}\right)^2 - 1\right]^{3/2}.$$ (2.9)

As a foundation for both constructing and understanding the structures of the synchronously rotating and tidally distorted stars in ZTWD binary systems, we have regenerated Chandraskehar's spherical white dwarf sequence using a variation of the SCF technique outlined by Hachisu (1986a) and described more fully in §2.1.3 below using both a 1D and 3D code. As is discussed in Chapter 3, Table 3.1 details key properties of the ZTWD structures that lie along this spherical model sequence. The white dwarf mass-radius relationship that is derived from the 3D models along this sequence is illustrated by the diamonds in Figure 3.1. For comparison, results from the published spherical sequence of Hachisu (1986a) are represented in this figure by asterisks and the solid curve shows the approximate, analytic mass-radius relationship, Eq. (A.14), derived for ZTWD stars by Nauenberg (1972). This can also be compared to the higher resolution 1D results presented in Figure 1.1. (As explained in Appendix A, it is more appropriate for us to compare our results to this "Nauenberg" mass-radius relation than to the more widely used "Eggleton" mass-radius relation, shown in Eq. A.16.)

2.1.2 Binary System Geometry and Governing Equations

Our objective is to determine the 3D structure of a pair of ZTWD stars that are in a tight, circular orbit under the condition that both stars are synchronously rotating with the binary orbital frequency Ω. We begin by specifying the masses M_1 and M_2 of the primary and secondary stars, respectively, such that $M_2 \leq M_1$. Alternatively, we can specify the
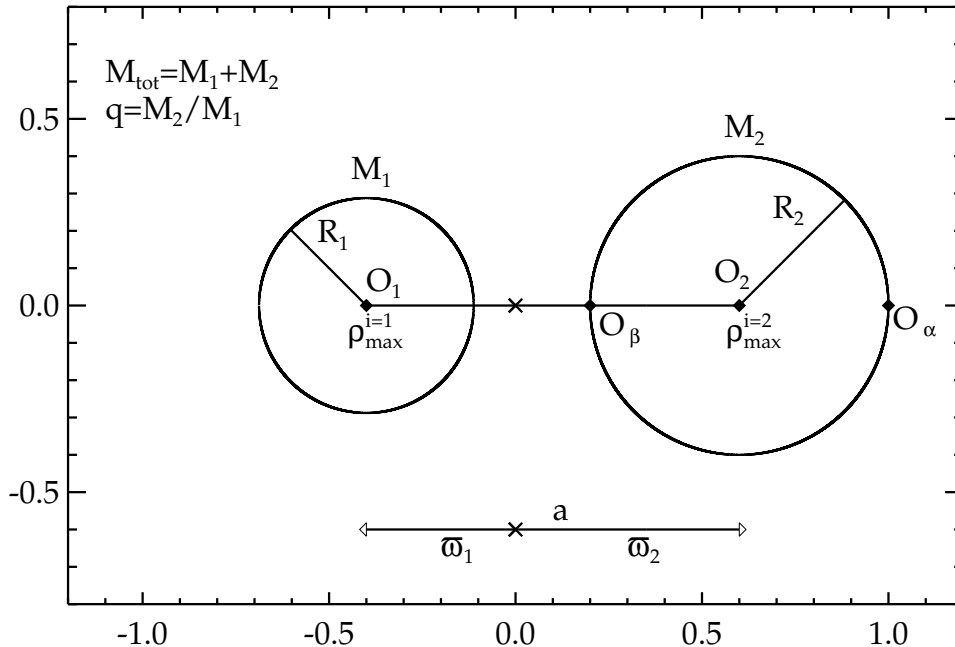
Figure 2.1 Schematic diagram illustrating the equatorial-plane structure of a binary star system. The primary star, on the left, has a mass M_1, a radius R_1, and a central density $\rho_{\max}^{i=1}$; the secondary star, on the right, has a mass $M_2 \leq M_1$, a radius R_2, and a central density $\rho_{\max}^{i=2}$. The centers of mass of the two stars (points labeled O_1 and O_2) are separated by a distance $a = \varpi_1 + \varpi_2$, and their distances from the center of mass of the system are, respectively, ϖ_1 and ϖ_2. The points labeled O_α and O_β identify, respectively, the outer edge and inner edge of the secondary star.

total system mass $M_{\text{tot}} \equiv M_1 + M_2$ and the system mass ratio $q \equiv M_2/M_1 \leq 1$, in which case,

$$M_1 = \left(\frac{1}{1+q}\right)M_{\text{tot}},$$

$$M_2 = \left(\frac{q}{1+q}\right)M_{\text{tot}}.$$

Figure 2.1 shows a slice through the equatorial plane of such a system under the assumption that both stars are spherically symmetric. For our final equilibrium models in which the effects of tidal and rotational distortions are taken into account in a fully self-consistent fashion, this figure provides only a schematic illustration of the binary system's equatorial-

plane structure. However, it provides an accurate depiction of the equatorial-plane structure of the initial stellar models that are fed into our iterative SCF scheme (see §2.1.3).

In Figure 2.1, the more massive, primary star is shown on the left and the less massive, secondary star is on the right; the centers of the stars are located a distance ϖ_1 and ϖ_2, respectively, from the center of mass of the binary system; and the binary separation $a = \varpi_1 + \varpi_2$. Because we are using a ZTWD equation of state, the central density $\rho^i_{\max}$ and radius R_i of each star ($i = 1, 2$) cannot be specified independently of each star's chosen mass. As an initial guess for our SCF technique, the values of $\rho^{i=1}_{\max}$, $\rho^{i=2}_{\max}$, R_1, and R_2 are drawn from Table 3.1, that is, they are given by values that correspond to spherical ZTWDs having masses M_1 and M_2.

For various values of the three principal system parameters M_1, M_2 and a, our specific aim is to determine in a self-consistent fashion on a cylindrical coordinate mesh (ϖ, θ, Z), the values and spatial distribution of the scalar fields $\rho^i(\varpi, \theta, Z)$, $H^i(\varpi, \theta, Z)$, and $P^i(\varpi, \theta, Z)$, for both stars ($i = 1, 2$) in synchronously rotating, ZTWD binaries. Following Hachisu (1986a,b), in order to construct these desired binary configurations we need to solve the following five equations simultaneously:

$$\nabla^2 \Phi(\varpi, \theta, z) = 4\pi G \sum_i \rho^i(\varpi, \theta, z) , \tag{2.10}$$

$$C^i = H^i(\varpi, \theta, z) + \Phi(\varpi, \theta, z) - \frac{1}{2}\Omega^2 \varpi^2 , \tag{2.11}$$

$$\rho^i(\varpi, \theta, z) = B[x^i(\varpi, \theta, z)]^3 = B\left\{ \left[\frac{B}{8A} H^i(\varpi, \theta, z) \right]^2 - 1 \right\}^{3/2} , \tag{2.12}$$

where $\Phi(\varpi, \theta, Z)$ is the Newtonian gravitational potential of the combined stellar system, and $C^{i=1}$ and $C^{i=2}$ are constants that specify the conditions of the Bernoulli flow inside each star.

Because the surfaces of both stars will be defined by the condition $\rho^i = x^i = 0$, it is clear from Eq. (2.8) that both surfaces will be associated with identical values of the enthalpy, specifically, $H^{i=1}_{\mathrm{surf}} = H^{i=2}_{\mathrm{surf}} = 8A/B$. However, because the maximum (central) density $\rho^i_{\max}$

in the two stars generally will not be the same (they will be the same only if the mass ratio $q = 1$), the enthalpy at the centers of the two stars generally will be different, namely,

$$H^i_{\max} = \frac{8A}{B}\left[(x^i_{\max})^2 + 1\right]^{1/2}, \tag{2.13}$$

where,

$$x^i_{\max} \equiv \left(\frac{\rho^i_{\max}}{B}\right)^{1/3}. \tag{2.14}$$

Following Hachisu (1986a), we choose to work in terms of the following dimensionless variables,

$$\hat{\varpi} \equiv \frac{\varpi}{\varpi_*}, \quad \hat{z} \equiv \frac{z}{\varpi_*}, \tag{2.15}$$

$$\hat{\rho}^i \equiv \frac{\rho^i}{\rho_*}, \tag{2.16}$$

$$\hat{P}^i \equiv \frac{P^i}{G\varpi_*^2\rho_*^2}, \tag{2.17}$$

$$\hat{H}^i \equiv \frac{H^i}{G\varpi_*^2\rho_*}, \tag{2.18}$$

$$\hat{\phi} \equiv \frac{\Phi}{G\varpi_*^2\rho_*}, \tag{2.19}$$

$$\hat{\Omega} \equiv \frac{\Omega}{(G\rho_*)^{1/2}}, \tag{2.20}$$

where $\varpi_* = \varpi_\alpha$ is the distance from the orbital axis to the outer edge of the secondary star (point O_α in Figure 2.1) as measured in the equatorial plane of the system, and $\rho_* \equiv \rho^{i=2}_{\max}$ is the maximum density of the secondary star. In terms of these dimensionless variables, the key equations (2.10), (2.11), and (2.12) become,

$$\nabla^2\hat{\phi}(\hat{\varpi}, \theta, \hat{z}) = 4\pi\sum_i \hat{\rho}^i(\hat{\varpi}, \theta, \hat{z}), \tag{2.21}$$

$$\hat{C}^i = \hat{H}^i(\hat{\varpi}, \theta, \hat{z}) + \hat{\phi}(\hat{\varpi}, \theta, \hat{z}) - \frac{1}{2}\hat{\Omega}^2\hat{\varpi}^2, \tag{2.22}$$

$$\hat{\rho}^i(\hat{\varpi}, \theta, \hat{z}) = \left[\frac{x^i(\hat{\varpi}, \theta, \hat{z})}{x_*}\right]^3, \tag{2.23}$$

where, $x_* \equiv (\rho_*/B)^{1/3}$. In order to relate x^i in Eq. (2.23) back to $\hat{H}^i$ in Eq. (2.22) we note that, via Eqs. (2.8) and (2.13),

$$\left(\frac{\hat{H}^i}{\hat{H}^i_{\max}}\right)^2 = \left(\frac{H^i}{H^i_{\max}}\right)^2 = \frac{(x^i)^2 + 1}{(x^i_{\max})^2 + 1}. \tag{2.24}$$

Hence, taking into consideration the natural limits on x^i inside both stars (namely, $x^i_{\max} \geq x^i > 0$), we deduce,

$$x^i = \left\{\left(\frac{\hat{H}^i}{\hat{H}^i_{\max}}\right)^2 [(x^i_{\max})^2 + 1] - 1\right\}^{1/2} \quad \text{for} \quad \frac{\hat{H}^i}{\hat{H}^i_{\max}} > [(x^i_{\max})^2 + 1]^{-1/2} \tag{2.25}$$

$$= 0 \quad \text{for} \quad \frac{\hat{H}^i}{\hat{H}^i_{\max}} < [(x^i_{\max})^2 + 1]^{-1/2}.$$

2.1.3 Solution Strategy

Our solution strategy is as follows. A "guess" is made for the density distribution $\hat{\rho}^i(\hat{\varpi}, \theta, \hat{z})$ inside both stars. The Poisson Eq. (2.21) is then solved in order to obtain a quantitative description of the gravitational potential $\hat{\phi}(\hat{\varpi}, \theta, \hat{z})$ throughout the computational domain that is consistent with the trial density distribution. With this knowledge of $\hat{\phi}(\hat{\varpi}, \theta, \hat{z})$, Eq. (2.22) is used to determine the two constants $\hat{C}^{i=2}$ and Ω by specifying a value for the entropy at two "boundary" points — points at two different locations on the surface of the secondary star. By specifying a value for the enthalpy at an additional "boundary" point at the center of the primary star, Eq. (2.22) also can be used to determine $\hat{C}^{i=1}$. From the calculated values of $\hat{C}^{i=2}$ and Ω, Eq. (2.22) (with i set to "2") is used to determine $\hat{H}^{i=2}$ throughout the secondary star; and from the calculated values of $\hat{C}^{i=1}$ and Ω, the same equation (with $i = 1$) is used to determine $\hat{H}^{i=1}$ throughout the primary star. Finally, from a knowledge of $\hat{H}^i$, Eq. (2.25) is used to determine x^i, then Eq. (2.23) is used to determine $\hat{\rho}^i$ throughout the interiors of both stars. This revised density profile for both stars is used as an improved "guess" for our iteration scheme and all of the outlined steps are repeated until a converged solution is reached.

Although our ultimate desire is to construct a model of a binary system that has a specified total mass and mass ratio, the values of the individual stellar masses are not constrained to remain constant throughout the cycles of our iteration scheme. Instead, we fix the values of $x_{\max}^{i=1}$ and $x_{\max}^{i=2}$ throughout the iteration until a converged solution has been reached. This proves to be an effective approach because, as pointed out by Hachisu (1986a,b), this type of SCF scheme converges more rapidly if the maximum density rather than the mass is held fixed. Also, for the ZTWD equation of state, we know that $x_{\max}$ is correlated with the stellar mass (see Table 3.1 and the upper left panel of Figure 1.1). In practice, if the mass of either star in a converged model does not match some desired value, we simply rerun the iteration scheme using an appropriately adjusted value of $x_{\max}$. In what follows, each of the steps in our SCF iteration scheme is described in more detail.

Initial Guess for $\hat{\rho}^i$ and Determination of $\hat{\phi}$

As with most successful iterative solution schemes, our SCF technique can converge relatively quickly to a desired solution if the initial guess for the relevant scalar fields is a good one. As mentioned earlier, our initial guess is two spherical white dwarfs having masses M_1 and M_2 in a circular orbit with a separation a (as depicted in Figure 2.1) and an orbital frequency, $\Omega = (GM_{\mathrm{tot}}/a^3)^{1/2}$, that is, $\hat{\Omega} = [M_{\mathrm{tot}}/(a^3 \rho_*)]^{1/2}$. For all but perhaps the smallest allowed separations, this should provide an excellent starting condition. For the specified pair of masses, Table 3.1 provides the appropriate values of various physical parameters, such as R_i, $\rho_{\max}^i$, and $x_{\max}^i$, for both stars. In addition, the spherical models from which the data in Table 3.1 were derived provide an initial guess for the density structure $\rho^i(\varpi, \theta, z)$ throughout the interiors of both stars. In order to transform these density arrays into the dimensionless densities $\hat{\rho}^i$ defined by Eq. (2.16), the profiles for both stars are normalized to $\rho_* \equiv \rho_{\max}^{i=2}$ before they are introduced into the cylindrical coordinate grid.

To be consistent with the dimensionless length scale defined by Eq. (2.15), the two

spherical stars are initially placed on the computational grid in such a way that the center of mass of the system falls at the origin of the coordinate system and the outer edge of the secondary star (point O_α in Figure 2.1) is at $\hat{\varpi} = 1$. The centers of the stars are therefore located, respectively, at

$$\hat{\varpi}_1 \equiv \frac{\varpi_1}{\varpi_\alpha} = \frac{q}{1 + \ell(1+q)}, \tag{2.26}$$

$$\hat{\varpi}_2 \equiv \frac{\varpi_2}{\varpi_\alpha} = \frac{1}{1 + \ell(1+q)}, \tag{2.27}$$

where the dimensionless ratio $\ell \equiv R_2/a$ is known once M_2 and a have been chosen. These two expressions make sense because $\varpi_\alpha = (\varpi_2 + a\ell) = [\varpi_2 + (\varpi_2 + \varpi_1)\ell]$ and, for a point-mass binary whose center of mass is at the origin of the grid, $\varpi_1 = q\varpi_2$.

With $\hat{\rho}^i$ defined everywhere on the grid, $\hat{\phi}(\hat{\varpi}, \theta, \hat{z})$ is calculated via Eq. (2.21). In this work the boundary values for $\hat{\phi}$ are calculated using the compact cylindrical Green's function expansion described in Cohl & Tohline (1999), and the values of the potential throughout the interior volume of the computational grid are calculated using the Krylov subspace methods provided by the PETSc software library (Balay et al (2004)). See further discussions in §2.2.

Secondary Star

During the iteration cycles we calculate new or updated values of the two constants $\hat{C}^{i=2}$ and $\hat{\Omega}$ by enforcing boundary conditions at the inner and outer edges of the secondary star – the points marked O_β and O_α in Figure 2.1 – and the coordinate locations of these two points are held fixed. Pinning down the location of points O_α and O_β prevents the geometric structure of the binary from varying dramatically from the initial configuration during the iterations. Because these two points lie on the surface of the secondary star and, hence, $\hat{H}_\alpha = \hat{H}_\beta = \hat{H}_{\text{surf}}^{i=2}$, an evaluation of Eq. (2.22) at these points gives,

$$\hat{\Omega}^2 = \frac{2[\hat{\phi}_\alpha - \hat{\phi}_\beta]}{[1 - \hat{\varpi}_\beta^2]}, \tag{2.28}$$

where the subscripts α and β imply that the variables have been evaluated at points O_α and O_β, respectively.

Knowledge of $\hat{\Omega}^2$ permits us to calculate values of the function,

$$\hat{F} \equiv -\hat{\phi} + \frac{1}{2}\hat{\Omega}^2\hat{\varpi}^2, \tag{2.29}$$

across the entire computational domain. From Eq. (2.22) we realize that this function also may be written as,

$$\hat{F} = (\hat{H}^i - \hat{C}^i), \tag{2.30}$$

that is, it differs from the enthalpy by only a constant. Therefore, in the region occupied by the secondary star, $\hat{H}^{i=2}$, $\hat{\rho}^{i=2}$, and $\hat{x}^{i=2}$ should all assume their maximum values at the same coordinate location where the function $\hat{F}$ reaches a local maximum, that is, at the location of $\hat{F}_{\max}^{i=2}$. This, then, becomes the updated position for point O_2 (see Figure 2.1). Using Eq. (2.30) in conjunction with Eq. (2.24) evaluated at point O_α (where $x = x_\alpha^{i=2} = 0$) allows us to determine the value of the constant $\hat{C}^{i=2}$. Specifically,

$$\frac{\hat{H}_\alpha}{\hat{H}_{\max}^{i=2}} = \frac{\hat{F}_\alpha + \hat{C}^{i=2}}{\hat{F}_{\max}^{i=2} + \hat{C}^{i=2}} = \left[\frac{1}{(x_{\max}^{i=2})^2 + 1}\right]^{1/2}. \tag{2.31}$$

Hence,

$$\hat{C}^{i=2} = \left\{\frac{\hat{F}_{\max}^{i=2} - [1 + (x_{\max}^{i=2})^2]^{1/2}\hat{F}_\alpha}{[1 + (x_{\max}^{i=2})^2]^{1/2} - 1}\right\}. \tag{2.32}$$

With the value of the constant $\hat{C}^{i=2}$ in hand, we can determine the value of the enthalpy everywhere inside the secondary star via the expression,

$$\hat{H}^{i=2} = \hat{C}^{i=2} + \hat{F}^{i=2}, \tag{2.33}$$

and, in particular,

$$\hat{H}_{\max}^{i=2} = \hat{C}^{i=2} + \hat{F}_{\max}^{i=2}. \tag{2.34}$$

Finally, then, from equations (2.23) and (2.25) we obtain an updated "guess" for the normalized density distribution inside the secondary star, that is,

$$\hat{\rho}^{i=2} \quad = \quad \frac{1}{x_*^3}\left\{\left(\frac{\hat{H}^{i=2}}{\hat{H}_{\max}^{i=2}}\right)^2 [(x_{\max}^{i=2})^2 + 1] - 1\right\}^{3/2}. \tag{2.35}$$

Primary Star

Using Eq. (2.13), we can determine the value of the normalized enthalpy at the center of the primary star from the values of $x_{\max}^i$ selected for both stars and the value of $\hat{H}_{\max}^{i=2}$ just derived for the secondary star. Specifically,

$$\hat{H}_{\max}^{i=1} \quad = \quad \hat{H}_{\max}^{i=2}\left[\frac{(x_{\max}^{i=1})^2 + 1}{(x_{\max}^{i=2})^2 + 1}\right]^{1/2}. \tag{2.36}$$

In the vicinity of the original center of the primary star, that is, in the vicinity of point O_1 as illustrated in Figure 2.1, the function $\hat{F}$ should exhibit a local maximum. We associate the location of this local maximum with the updated position of point O_1 and we set $\hat{F}_{\max}^{i=1}$ equal to the value of the function at this local maximum. We therefore deduce from Eq. (2.30) that,

$$\hat{C}^{i=1} \quad = \quad \hat{H}_{\max}^{i=1} - \hat{F}_{\max}^{i=1}. \tag{2.37}$$

With this constant in hand, the normalized enthalpy throughout the primary star can be determined via the expression,

$$\hat{H}^{i=1} \quad = \quad \hat{C}^{i=1} + \hat{F}^{i=1}, \tag{2.38}$$

and, by analogy with equation (2.35), we obtain an updated "guess" for the normalized density distribution inside the primary star via the expression,

$$\hat{\rho}^{i=1} \quad = \quad \frac{1}{x_*^3}\left\{\left(\frac{\hat{H}^{i=1}}{\hat{H}_{\max}^{i=1}}\right)^2 [(x_{\max}^{i=1})^2 + 1] - 1\right\}^{3/2}. \tag{2.39}$$

Global Properties and Convergence

Our iterative scheme is judged to be operating well if various calculated model parameters — such as the dimensionless stellar masses $\hat{M}^i$ and Bernoulli constants $\hat{C}^i$ — converge toward well-defined values. We also have found it useful to track the convergence of various global energy parameters. Specifically, at the end of each iteration cycle we calculate the dimensionless rotational kinetic energy $\hat{K}$, gravitational potential energy $\hat{W}$, total internal energy $\hat{U}$ (see, for example, Eq. (75') in Chapter XI of Chandrasekhar (1967)), and globally averaged pressure $\hat{\Pi}$ of the model, defined as follows:

$$\hat{K} \equiv \int \frac{1}{2}\hat{\Omega}^2 \hat{\varpi}^2 \hat{\rho} d\hat{V}\,, \tag{2.40}$$

$$\hat{W} \equiv \int \frac{1}{2}\hat{\phi}\hat{\rho} d\hat{V}\,, \tag{2.41}$$

$$\hat{U} \equiv \int \left[\left(\hat{H} - \frac{8A}{B}\right)\hat{\rho} - \hat{P}\right] d\hat{V}\,, \tag{2.42}$$

$$\hat{\Pi} \equiv \int \hat{P} d\hat{V}\,. \tag{2.43}$$

where $d\hat{V} = \hat{\varpi} d\hat{\varpi} d\theta d\hat{z}$ is the dimensionless differential volume element on our cylindrical grid. Then the system's dimensionless total energy is given by the sum,

$$\hat{E}_{\text{tot}} \equiv \frac{E_{\text{tot}}}{G\rho_*^2 \varpi_*^5} = \hat{K} + \hat{W} + \hat{U}\,, \tag{2.44}$$

and, if the model has converged to a proper equilibrium state, according to the virial theorem we should expect,

$$2\hat{K} + \hat{W} + 3\hat{\Pi} = 0\,. \tag{2.45}$$

In general, at each iteration step the condition of virial equilibrium, Eq. (2.45), will not be satisfied, but if our iteration scheme is well behaved, convergence toward the virial condition should be achieved. With this in mind, we have found that the virial error,

$$VE \equiv \left|\frac{2\hat{K} + \hat{W} + 3\hat{\Pi}}{\hat{W}}\right|\,, \tag{2.46}$$

Table 2.1.   Convergence of SCF Method: Binary Model B3

N_ϖ	N_θ	N_z	δ	VE
64	128	33	1.0×10^{-2}	4.5×10^{-3}
			1.0×10^{-3}	2.6×10^{-3}
			1.4×10^{-4}	2.2×10^{-3}
128	256	65	1.0×10^{-2}	4.0×10^{-3}
			1.0×10^{-3}	9.1×10^{-4}
			1.0×10^{-4}	5.7×10^{-4}
			3.5×10^{-5}	5.4×10^{-4}

provides a meaningful measure of the quality of each model.

We declare that satisfactory convergence to a given model has been achieved when the absolute value of the fractional change between iterations has dropped below a specified convergence criterion, $\delta \sim 10^{-4}$, for all of the following quantities: $\hat{C}^i$, $\hat{M}^i$, $\hat{\Omega}$, $\hat{K}$, $\hat{W}$, $\hat{\Pi}$, and the physical value of ϖ_α.

In addition, the converged model is judged to be a good equilibrium state if the virial error, VE, is sufficiently small. Table 2.1 illustrates how we were able to achieve a lower virial error and, hence, a more accurate representation of an equilibrium configuration, by improving the grid resolution and/or by specifying a tighter convergence criterion. Specifically, the table shows that as we were constructing binary model B3 (see discussion associated with Table 3.5, below) we were able to push the VE down from a value $\sim 5 \times 10^{-3}$ to a value $\sim 5 \times 10^{-4}$ by increasing the grid resolution from (64,128,33) to (128,256,65) zones in $(\hat{\varpi}, \theta, \hat{z})$ and by pushing δ from 10^{-2} to 3.5×10^{-5}.

After the SCF code has converged to the desired equilibrium model, the various dimensionless variables are converted back to proper physical units following, for example, the scalings presented in expressions (2.15) through (2.20). We note in particular that the value of the scale length $\varpi_* = \varpi_\alpha$ is obtained by evaluating Eq. (2.13) for $i = 2$ in combination

with Eq. (2.18), which gives,

$$\varpi_* = \left[\frac{8A/B}{G\rho_*}\right]^{1/2} (\hat{H}_{max}^{i=2})^{-1/2} \left[(x_{max}^{i=2})^2 + 1\right]^{1/4} . \tag{2.47}$$

In addition to the physical variables already identified, for each converged model we have found it useful to evaluate the system's total angular momentum,

$$J_{\text{tot}} \equiv \int \varpi^2 \Omega \rho dV , \tag{2.48}$$

as well as the spin angular momentum of each component star, J_{spin}^i, and each star's Roche-lobe filling factor, f_{RL}^i. As with the determination of quantities such as M^i and R^i, these latter two quantities are obtained by performing volume integrals over appropriate sub-domains of the computational grid, determined as follows. Let the origin of a Cartesian grid coincide with the center of mass of the binary system and align the x-axis of that grid with the line that connects the centers of the two stars as illustrated in Figure 2.1. Between points O_1 and O_2 along this axis, the effective potential,

$$\Phi_{\text{eff}}(x) \equiv \Phi(x) - \frac{1}{2}\Omega^2 x^2 , \tag{2.49}$$

will exhibit a maximum at position x_{L1} associated with the inner "$L1$" Lagrange point. We define sub-domain $\mathcal{D}_*^{i=2}$ as the volume of the grid for which $x \equiv \varpi \cos\theta \geq x_{L1}$ and $\rho > 0$, that is, the region occupied by the secondary star; and we define sub-domain $\mathcal{D}_*^{i=1}$ as the volume of the grid for which $x < x_{L1}$ and $\rho > 0$, that is, the region occupied by the primary star. Then the mass of each star is determined by the integral,

$$M^i = \int_{\mathcal{D}_*^i} \rho^i dV , \tag{2.50}$$

the volume occupied by each star is,

$$\mathcal{V}_*^i = \int_{\mathcal{D}_*^i} dV , \tag{2.51}$$

and the spin angular momentum of each star is given by the expression,

$$J^i_{\text{spin}} \equiv \int_{\mathcal{D}^i_*} \left[\varpi^2 \sin^2\theta + (\varpi\cos\theta - \varpi_i)^2 \right] \Omega\rho^i dV . \tag{2.52}$$

Having determined the volumes $\mathcal{V}^i$ occupied by both rotationally flattened and tidally distorted stars, we define the mean radius of each star as,

$$R^i = \left(\frac{3\mathcal{V}^i_*}{4\pi} \right)^{1/3} . \tag{2.53}$$

We furthermore define sub-domain $\mathcal{D}^{i=2}_{\text{RL}}$ as the volume of the grid for which $x \geq x_{L1}$ and $\Phi_{\text{eff}} \leq \Phi_{\text{eff}}(x_{L1})$, and sub-domain $\mathcal{D}^{i=1}_{\text{RL}}$ as the volume of the grid for which $x < x_{L1}$ and $\Phi_{\text{eff}} \leq \Phi_{\text{eff}}(x_{L1})$. Then the Roche-lobe volume surrounding each star is,

$$\mathcal{V}^i_{\text{RL}} = \int_{\mathcal{D}^i_{\text{RL}}} dV , \tag{2.54}$$

and each star's Roche-lobe filling factor is obtained from the ratio,

$$f^i_{\text{RL}} = \frac{\mathcal{V}^i_*}{\mathcal{V}^i_{\text{RL}}} . \tag{2.55}$$

2.2 Numerical Solutions for the Gravitational Potential

The self-gravity of the binary system is one of the most dominate phenomena driving the evolution of the binary. In order to obtain accurate numerical results in a CFD simulation, the gravitational potential must be reevaluated at every step in the time integration. The gravitational potential, Φ, is defined as

$$\Phi(\vec{r}) = -\int_0^\infty \frac{G\rho(\vec{r}')d^3r'}{|\vec{r} - \vec{r}'|}, \tag{2.56}$$

where ρ is the mass density, and $\vec{r}'$ is position vector that is integrated over all space. The gravitational potential is more commonly calculated by solving the Poisson equation,

$$\nabla^2\Phi = 4\pi G\rho. \tag{2.57}$$

The solution to this elliptic equation requires that all cells in the grid have knowledge of the value of ρ and Φ at all other cells. In contrast, the hyberbolic equations used to update the fluid quantities require only knowledge of their neighboring cells. This need to know the value of the potential everywhere requires extra design consideration when developing a solver that is going to be implemented in parallel because each CPU in the cluster will only have local access to the small subset of data on which it is operating. A communication between the processors allows the nodes on the cluster to share this information with one another, but inter-processor communication must be kept to a minimum because it is slow compared to calculations.

In the existing version of our group's hydrocode (see Chapter 4) and SCF code, an efficient solver has been developed for the gravitational potential. However, this solver is limited to coordinate systems in which there is a periodic coordinate because it requires a Fourier transform. Until the present time all simulations done within the group have been done in cylindrical coordinate systems, but a more flexible solver is desired so that simulations are no longer limited to certain coordinate systems. Additionally, the Fourier transform method is not extensible to adaptive meshes. A variety of numerical packages have been developed by other groups to solve elliptic equations in parallel environments. For this work, we have chosen to use elliptic solvers within The Portable Extensible Toolkit for Scientific Computing (PETSc) and to link these solvers with our hydrodynamics code to solve for the gravitational potential (Balay et al. 2004).

2.2.1 Numerical Discretization

The Poisson equation in cylindrical coordinates is given by

$$\frac{\partial^2 \Phi}{\partial \varpi^2} + \frac{1}{\varpi}\frac{\partial \Phi}{\partial \varpi} + \frac{1}{\varpi^2}\frac{\partial^2 \Phi}{\partial \theta^2} + \frac{\partial^2 \Phi}{\partial z^2} = 4\pi G \rho, \tag{2.58}$$

where ϖ is the radial coordinate, θ is the azimuthal coordinate, and z is the vertical coordinate.

Using a second order finite difference scheme for each derivative we obtain the following formulation:

$$\frac{\Phi_{i+1} - 2\Phi + \Phi_{i-1}}{(\Delta\varpi)^2} + \frac{\Phi_{i+1} - \Phi_{i-1}}{2\varpi\Delta\varpi} + \frac{\Phi_{j+1} - 2\Phi + \Phi_{j-1}}{\varpi^2 (\Delta\theta)^2} + \frac{\Phi_{k+1} - 2\Phi + \Phi_{k-1}}{(\Delta z)^2} = 4\pi G\rho. \quad (2.59)$$

Collecting the coefficients on Φ,

$$\left(-\frac{2}{(\Delta\varpi)^2} - \frac{2}{\varpi^2 (\Delta\theta)^2} - \frac{2}{(\Delta z)^2} \right) \Phi + \left(\frac{1}{(\Delta\varpi)^2} + \frac{1}{2\varpi\Delta\varpi} \right) \Phi_{i+1}$$
$$+ \left(\frac{1}{(\Delta\varpi)^2} - \frac{1}{2\varpi\Delta\varpi} \right) \Phi_{i-1} + \frac{1}{\varpi^2 (\Delta\theta)^2}\Phi_{j+1} + \frac{1}{\varpi^2 (\Delta\theta)^2}\Phi_{j-1}$$
$$+ \frac{1}{(\Delta z)^2}\Phi_{k+1} + \frac{1}{(\Delta z)^2}\Phi_{k-1} = 4\pi G\rho. \quad (2.60)$$

These coefficients can then be put into a two-dimensional, $N \times N$ sparse matrix $\mathbf{A}$, where N is the product of the number of radial, azimuthal and vertical divisions. Each row in A has a maximum of seven non-zero elements. The gravitational potential and density are stored in 1D arrays and the Poisson equation can be written as,

$$\mathbf{A}\Phi = 4\pi G\rho. \quad (2.61)$$

2.2.2 Test Problems

The solver was tested using two different cases with known analytic solutions: a uniform density sphere, also known as an n=0 polytrope, and a spherical n=1 polytrope. Polytropes are stellar structures that have been constructed using the so-called polytropic equation of state, Eq. (4.9). In the first case, the analytic form of the potential and density are

$$\rho(r_{sp}) = \rho_c \qquad\qquad r_{sp} \leq R_{sp} \qquad (2.62)$$
$$\rho(r_{sp}) = 0 \qquad\qquad r_{sp} > R_{sp} \qquad (2.63)$$
$$\Phi(r_{sp}) = -2\pi G\rho_c \left(R_{sp}^2 - \frac{r_{sp}^2}{3} \right) \qquad r_{sp} \leq R_{sp} \qquad (2.64)$$
$$\Phi(r_{sp}) = -\frac{4}{3}\pi G\rho_c \frac{R_{sp}^3}{r_{sp}} \qquad r_{sp} > R_{sp}, \qquad (2.65)$$

where r_{sp} is the distance from the center of the spherical object and R_{sp} is the total radius of the object. The density distribution and potential for a spherical n=1 polytrope are defined as

$$\rho(r_{sp}) = \frac{\rho_c R_{sp} \sin(\frac{\pi r_{sp}}{R_{sp}})}{\pi r_{sp}} \qquad\qquad r_{sp} \leq R_{sp} \qquad\qquad (2.66)$$

$$\rho(r_{sp}) = 0 \qquad\qquad r_{sp} > R_{sp} \qquad\qquad (2.67)$$

$$\Phi(r_{sp}) = \frac{-4GR_{sp}^2\rho_c}{\pi}\left[\frac{R_{sp}}{r_{sp}\pi}\sin\left(\frac{\pi r_{sp}}{R_{sp}}\right) + 1\right] \qquad r_{sp} \leq R_{sp} \qquad\qquad (2.68)$$

$$\Phi(r) = \frac{-GM}{r_{sp}} \qquad\qquad r_{sp} > R_{sp}, \qquad\qquad (2.69)$$

where $M = 4R_{sp}^3\rho_c/\pi$ is the total mass of the spherical object.

The numeric and analytic solutions are compared below for n=0 and n=1 polytropes. Example configurations are shown in Figure 2.2. The analytic solution used in these comparisons was calculated by different methods in the interior and exterior of the star. In the interior the mass was calculated by solving the exact analytic solutions in the preceding sections. However, in the exterior region the potential was calculated for a point mass at the center of the sphere. Instead of using the analytically integrated mass, the mass of the individual cells was summed to obtain the total mass. This mass was chosen because it more closely resembles the mass that will be used by the numeric solver for the Poisson equation. The errors shown in Table 2.2 are percent differences between the numeric and analytic solutions.
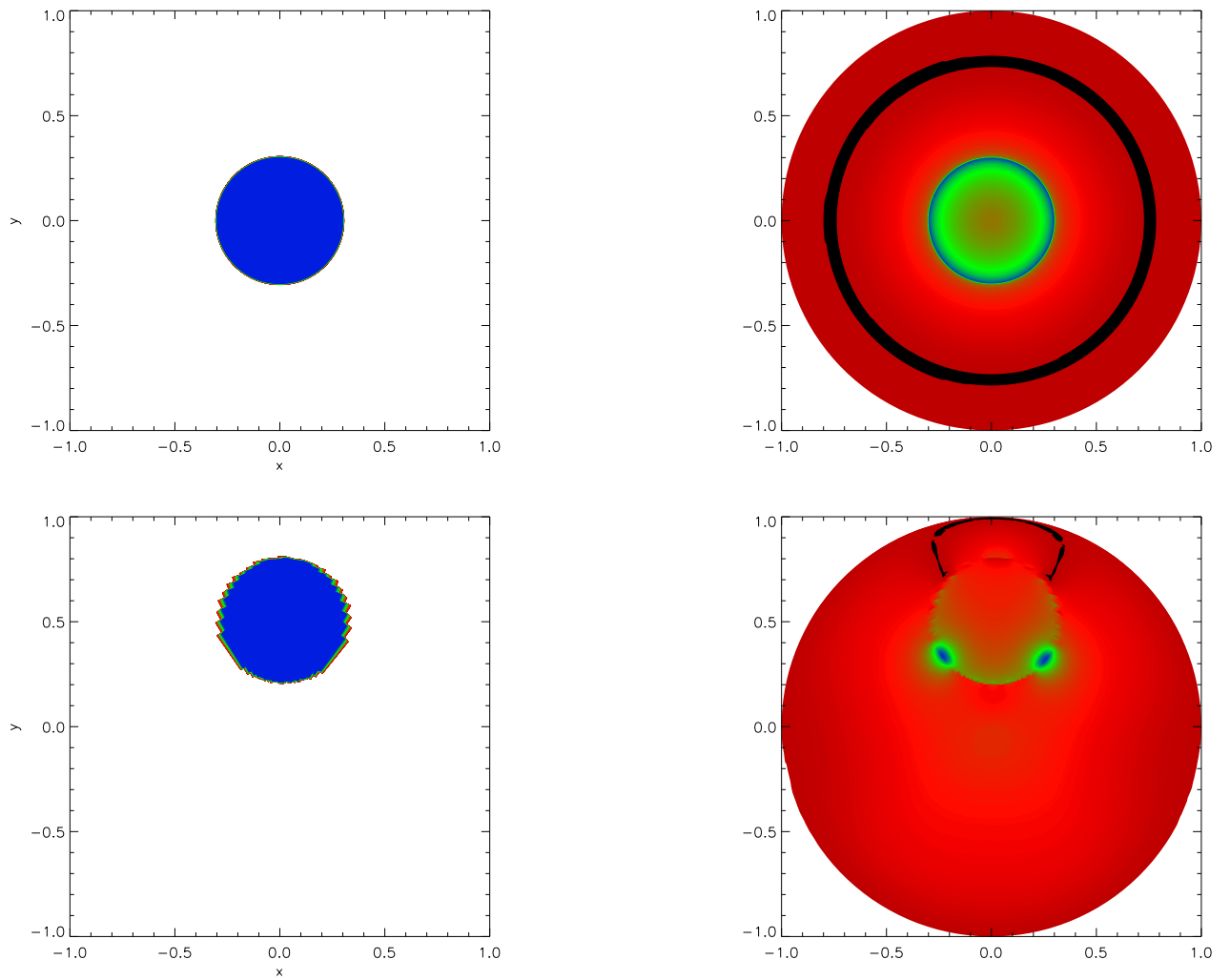
Figure 2.2 An n = 0 spherical polytrope. The left plots are the density distributions and the right plots are the error between the numerical and analytic solutions. In the top diagrams the sphere is centered on the cylindrical axis. On the bottom the center of the sphere has been displaced by 0.5 on the y axis. Blue represents regions of maximum density (left) and error (right) and dark red represents minimum values. These correspond to the values given in Table 2.2 for 128^3 resolution.

Table 2.2.   Error of Poisson solver for spherical polytropes

n	ϖ	z	θ	y displacement	Min Error	Max Error	Avg Error
0	64	64	64	0	1.10×10^{-4}	1.41	2.85×10^{-1}
1	64	64	64	0	2.40×10^{-3}	4.98×10^{-1}	2.71×10^{-1}
0	64	64	64	0.5	0.00	8.87×10^{-1}	7.35×10^{-2}
1	64	64	64	0.5	0.00	4.10×10^{-1}	8.46×10^{-2}
0	128	128	128	0	1.24×10^{-4}	4.10×10^{-1}	8.46×10^{-2}
1	128	128	128	0	1.11×10^{-4}	1.69×10^{-1}	5.52×10^{-2}
0	128	128	128	0.5	6.05×10^{-5}	7.02×10^{-1}	9.61×10^{-2}
1	128	128	128	0.5	0.00	1.52	6.05×10^{-2}

3. Steady State Binary Sequences[1]

As mentioned earlier, we initially used a simplified version of our SCF code to construct a large number of single, nonrotating white dwarfs in order to compare our solutions with previous results (see Figure 3.1) and to provide initial guesses for the density distributions inside both stars in each binary system. Table 3.1 details the properties of single, nonrotating white dwarfs that have central densities ranging from $10^{4.5}$ g cm^{-3} to 10^{10} g cm^{-3} as determined from our model calculations; the 23 selected models are equally spaced in units of $\log \rho_{\max}$.

These spherical models were constructed on a uniform cylindrical mesh with resolution $(128, 128, 128)$ in $(\hat{\varpi}, \theta, \hat{z})$ using a convergence criterion $\delta = 10^{-4}$. For each converged model, the first six columns of Table 3.1 list, respectively, the star's mass M in solar masses, radius R in units of 10^8 cm, central density $\rho_{\max}$ in g cm^{-3}, corresponding value of $x_{\max} = (\rho_{\max}/B)^{1/3}$, moment of inertia,

$$I = \int \varpi^2 \rho \, dV \, , \tag{3.1}$$

in units of 10^{50} g cm^2, and the radius of gyration, $k \equiv I/(MR^2)$. As shown in the last column of Table 3.1, a typical virial error for these converged models was $10^{-4} - 10^{-5}$. The values tabulated for the radius of gyration vary smoothly from $k = 0.2036$ for $M = 0.0844 M_\odot$ to $k = 0.1013$ for $M = 1.4081 M_\odot$. (See also the upper right panel of Figure 1.1.) This is consistent with our understanding that low-mass white dwarfs have structures similar to $n = 3/2$ polytropes for which $k = 0.205$ (Ruciński, 1988), while high-mass white dwarfs display structures similar to $n = 3$ polytropes for which $k = 0.0758$ (Ruciński, 1988). Our values of k over this range of stellar masses are also consistent with the analytic function for $k(M)$ that Marsh et al. (2004) fit through similar spherical model data. Knowledge of the

---

[1]§2.1 and Chapter 3 reproduced by permission of the AAS (Even & Tohline (2009))

Table 3.1. Sequence of single, nonrotating ZTWDs.

M $(M_\odot)$	R (10^8 cm)	$\rho_{\max}$ (g cm^{-3})	$x_{\max}$	I (10^{50} g cm^2)	k	VE
0.0844	19.7673	3.1623×10^4	0.2526	1.3317	0.2036	1.4×10^{-5}
0.1113	17.9368	5.6234×10^4	0.3060	1.4422	0.2031	6.1×10^{-5}
0.1460	16.2672	1.0000×10^5	0.3708	1.5508	0.2024	1.4×10^{-5}
0.1903	14.7421	1.7783×10^5	0.4492	1.6517	0.2015	5.8×10^{-5}
0.2457	13.3464	3.1623×10^5	0.5442	1.7360	0.2001	1.4×10^{-5}
0.3134	12.0666	5.6234×10^5	0.6593	1.7936	0.1983	5.8×10^{-5}
0.3938	10.8906	1.0000×10^6	0.7988	1.8133	0.1958	5.9×10^{-5}
0.4859	9.8078	1.7783×10^6	0.9678	1.7852	0.1926	1.6×10^{-5}
0.5873	8.8097	3.1623×10^6	1.1725	1.7051	0.1887	6.1×10^{-5}
0.6942	7.8896	5.6234×10^6	1.4205	1.5754	0.1839	5.8×10^{-5}
0.8018	7.0419	1.0000×10^7	1.7209	1.4058	0.1783	7.6×10^{-5}
0.9058	6.2628	1.7783×10^7	2.0850	1.2122	0.1721	6.6×10^{-5}
1.0022	5.5487	3.1623×10^7	2.5260	1.0111	0.1653	5.1×10^{-5}
1.0882	4.8961	5.6234×10^7	3.0603	0.8176	0.1581	6.3×10^{-5}
1.1624	4.3023	1.0000×10^8	3.7076	0.6429	0.1507	6.3×10^{-5}
1.2246	3.7643	1.7783×10^8	4.4919	0.4929	0.1433	7.0×10^{-5}
1.2753	3.2793	3.1623×10^8	5.4421	0.3698	0.1360	7.4×10^{-5}
1.3155	2.8443	5.6234×10^8	6.5932	0.2723	0.1290	9.0×10^{-5}
1.3469	2.4560	1.0000×10^9	7.9879	0.1972	0.1225	1.1×10^{-4}
1.3708	2.1116	1.7783×10^9	9.6775	0.1410	0.1164	1.2×10^{-4}
1.3887	1.8078	3.1623×10^9	11.7246	0.0997	0.1108	1.3×10^{-4}
1.4020	1.5414	5.6234×10^9	14.2047	0.0699	0.1058	1.4×10^{-4}
1.4116	1.3092	1.0000×10^{10}	17.2094	0.0486	0.1013	1.4×10^{-4}
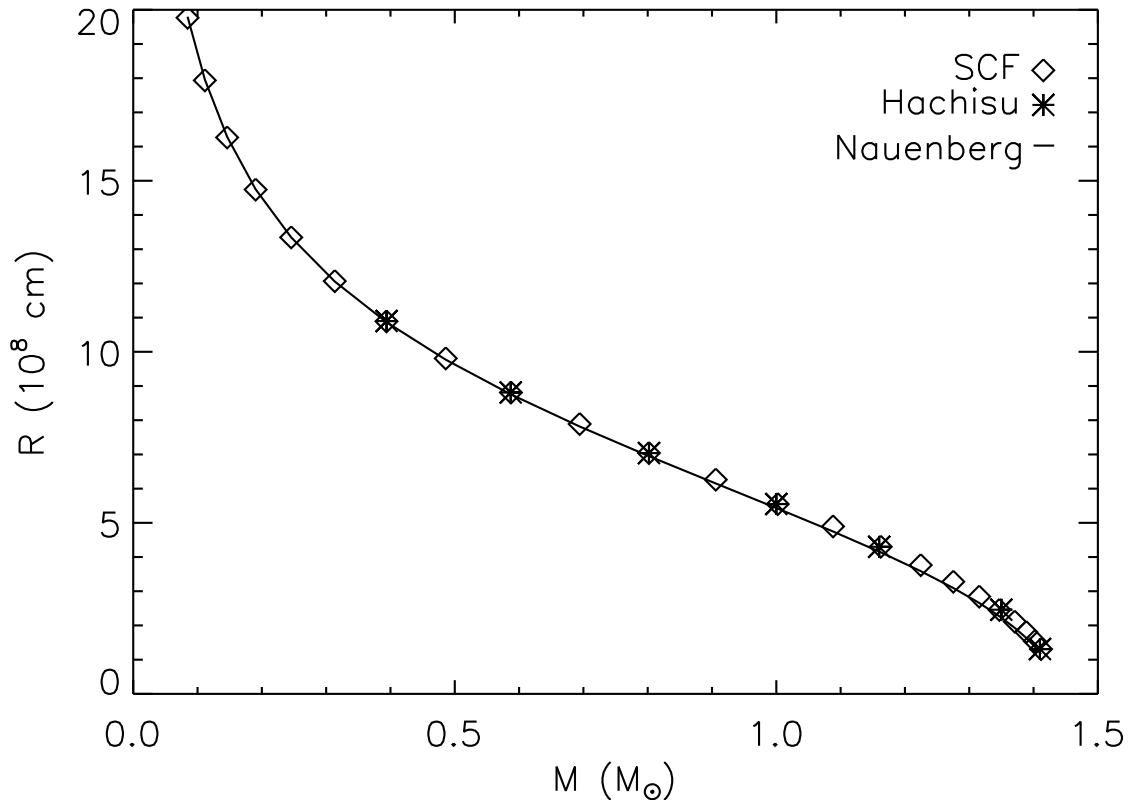
Figure 3.1 The mass-radius relationship is shown for spherical stars with our adopted ZTWD equation of state. Diamonds represent results derived using our three-dimensional SCF scheme applied to nonrotating, isolated configurations (see Table 3.1); asterisks show previously published results for the same equation of state taken from Hachisu (1986a); the solid curve shows the analytic mass-radius relation, Eq. (A.14), derived by Nauenberg (1972).

radius of gyration of these spherical ZTWD models has assisted us in analyzing the tidally distorted structures that arise in our models of synchronously rotating white dwarfs in close binary systems (see further discussion, below).

Using this same 3D, cylindrical coordinate grid we constructed nonrotating models with central densities above 10^{10} g cm^{-3}, that is, with masses above $1.4 M_\odot$. We have not included these higher mass models in Table 3.1 or Figure 3.1, however, because they did not converge to satisfactorily accurate structures. In particular, as the mass was steadily increased above

$1.4 M_\odot$, the models converged to structures with steadily increasing (rather than decreasing) values of k. By contrast, as shown in Figure 1.1 models constructed using a one-dimensional spherical code with much higher spatial resolution displayed values of k that decreased steadily to a value of 0.0755 at masses approaching M_{ch}. If desired, the three-dimensional computational grid resolution could be increased to produce more accurate models of the white dwarf structure near the Chandrasekhar mass limit.

3.1 Inspiral White Dwarf Binary Sequences

The slow inspiral evolution of a DWD binary can be mimicked by constructing a sequence of detached binaries having fixed M_{tot} and fixed q but varying separation, down to the separation, a_{crit}, at which the less massive star first makes contact with its Roche lobe. In an effort to illustrate the capabilities of our SCF code, we have constructed three binary sequences having the same total mass — namely, $M_{\mathrm{tot}} = 1.5 M_\odot$ — but three separate mass ratios. Specifically, sequence 'A' has $q = 1$, sequence 'B' has $q = 2/3$, and sequence 'C' has $q = 1/2$. As detailed in Table 3.2, spherical models were constructed with the desired primary and secondary masses for these three sequences — specifically, $M = 0.5 M_\odot, 0.6 M_\odot, 0.75 M_\odot, 0.9 M_\odot$ and $1.0 M_\odot$ — to provide good "guesses" for the initial binary star density distributions to start each SCF iteration. In addition to listing the values of M, R, ρ_{max}, x_{max}, and k for each of these converged spherical models, as was done for a wider range of spherical models in Table 3.1, Table 3.2 also lists values for the global energies W, U, and Π in units of 10^{50} ergs.

Along each sequence, all the binary models were constructed using a uniform cylindrical grid with (128,256,65) zones in $(\hat{\varpi}, \theta, \hat{z})$; by implementing reflection symmetry through the equatorial plane, only half as many zones were needed in the vertical direction as in the radial direction to achieve the same resolution in both. No additional symmetries were assumed in constructing the sequence, although, for the models shown here, symmetry through the x-z

Table 3.2. Selected single, nonrotating ZTWDs.

M ($M_\odot$)	R (10^8 cm)	ρ_{max} (g cm^{-3})	x_{max}	k	W (10^{50} ergs)	U (10^{50} ergs)	Π (10^{50} ergs)
0.5019	9.6383	1.9536×10^6	0.9979	0.1923	-0.6130	0.3326	0.2044
0.6022	8.6713	3.4341×10^6	1.2043	0.1889	-0.9932	0.5526	0.3311
0.7522	7.4244	7.6648×10^6	1.5739	0.1813	-1.8512	1.0757	0.6171
0.9028	6.2847	1.7483×10^7	2.0718	0.1726	-3.2433	1.9860	1.0812
1.0025	5.5456	3.1703×10^7	2.5265	0.1655	-4.6465	2.9644	1.5490

plane also could have been implemented for additional savings. The convergence criterion was set to $\delta = 2.5 \times 10^{-4}$; in most models, $\hat{\Omega}$ was the last variable to converge to this desired level. We note that, because the same number of grid zones was used for each model and each binary was scaled to fit entirely within the grid, the effective resolution of each star decreased as the binary separation a increased along each sequence.

Two tables have been produced for each DWD inspiral sequence in order to detail the properties of the models that lie along each sequence. For sequence 'A' ($q = 1$), for example, Table 3.3 lists the values of six global binary system parameters (a, Ω, M_{tot}, q, J_{tot}, E_{tot}) and the virial error obtained for thirty-five models (numbered $A1$ through $A35$) whose binary separations vary from 2.0956×10^9 cm at contact (model $A1$) to 3.0911×10^9 cm (model $A35$). For this same group of models, Table 3.4 lists calculated values of five parameters (M_i, R_i, ρ_{max}^i, f_{RL}^i, J_{spin}^i) for the individual stellar components ($i = 1, 2$). Tables 3.5 and 3.6 provide the same detailed information for models along sequence 'B' ($q = 2/3$), and Tables 3.7 and 3.8 provide this information for models along sequence 'C' ($q = 1/2$).

The equatorial-plane density distributions displayed in Figures 3.2, 3.3, and 3.4 illustrate the degree to which both white dwarf components are distorted by tides for various binary separations along each sequence. Labels in the upper-right-hand corner of each figure panel identify each binary system according to its corresponding position along each sequence, as

Table 3.3. DWD Inspiral Sequence 'A': $M_{\text{tot}} = 1.5 M_\odot$; $q = 1$

Model	a (10^9 cm)	Ω (10^{-2} s^{-1})	M_{tot} ($M_\odot$)	q	J_{tot} (10^{50} cgs)	E_{tot} (10^{50} erg)	VE
$A1$	2.0956	14.8480	1.5045	1.0000	5.3879	-1.8624	2.7×10^{-4}
$A2$	2.0970	14.8317	1.5043	1.0000	5.3881	-1.8618	2.8×10^{-4}
$A3$	2.1042	14.7493	1.5036	1.0000	5.3882	-1.8589	2.8×10^{-4}
$A4$	2.1099	14.6847	1.5030	1.0000	5.3886	-1.8567	2.9×10^{-4}
$A5$	2.1162	14.6156	1.5031	1.0000	5.3915	-1.8566	2.7×10^{-4}
$A6$	2.1239	14.5339	1.5031	1.0000	5.3954	-1.8560	2.7×10^{-4}
$A7$	2.1428	14.3360	1.5032	1.0000	5.4059	-1.8549	2.8×10^{-4}
$A8$	2.1544	14.2154	1.5030	1.0000	5.4112	-1.8532	2.9×10^{-4}
$A9$	2.1671	14.0863	1.5029	1.0000	5.4180	-1.8519	2.9×10^{-4}
$A10$	2.1809	13.9475	1.5028	1.0000	5.4254	-1.8508	2.6×10^{-4}
$A11$	2.1960	13.7990	1.5027	1.0000	5.4337	-1.8490	2.7×10^{-4}
$A12$	2.2292	13.4849	1.5030	1.0000	5.4554	-1.8471	2.6×10^{-4}
$A13$	2.2479	13.3121	1.5027	1.0000	5.4665	-1.8448	2.7×10^{-4}
$A14$	2.2669	13.1429	1.5032	1.0000	5.4814	-1.8447	2.7×10^{-4}
$A15$	2.2880	12.9570	1.5030	1.0000	5.4944	-1.8421	2.7×10^{-4}
$A16$	2.3103	12.7655	1.5027	1.0000	5.5082	-1.8392	2.8×10^{-4}
$A17$	2.3572	12.3804	1.5029	1.0000	5.5423	-1.8359	2.8×10^{-4}
$A18$	2.3828	12.1772	1.5027	1.0000	5.5597	-1.8329	2.8×10^{-4}
$A19$	2.4092	11.9748	1.5028	1.0000	5.5792	-1.8307	2.8×10^{-4}
$A20$	2.4362	11.7751	1.5032	1.0000	5.6013	-1.8298	2.8×10^{-4}
$A21$	2.4652	11.5645	1.5030	1.0000	5.6221	-1.8265	2.9×10^{-4}
$A22$	2.5261	11.1442	1.5030	1.0000	5.6684	-1.8215	2.8×10^{-4}
$A23$	2.5584	10.9314	1.5030	1.0000	5.6928	-1.8185	2.9×10^{-4}
$A24$	2.5920	10.7176	1.5028	1.0000	5.7185	-1.8151	3.1×10^{-4}
$A25$	2.6264	10.5057	1.5029	1.0000	5.7457	-1.8127	3.0×10^{-4}
$A26$	2.6624	10.2904	1.5028	1.0000	5.7729	-1.8093	3.0×10^{-4}
$A27$	2.6991	10.0786	1.5029	1.0000	5.8016	-1.8068	2.9×10^{-4}
$A28$	2.7376	9.8598	1.5028	1.0000	5.8286	-1.8039	1.5×10^{-4}
$A29$	2.8175	9.4479	1.5031	1.0000	5.8981	-1.7984	3.2×10^{-4}
$A30$	2.8597	9.2377	1.5031	1.0000	5.9315	-1.7951	3.2×10^{-4}
$A31$	2.8784	9.1459	1.5027	1.0000	5.9440	-1.7925	3.2×10^{-4}
$A32$	2.9478	8.8242	1.5032	1.0000	6.0024	-1.7892	3.3×10^{-4}
$A33$	2.9940	8.6120	1.5031	1.0000	6.0336	-1.7860	1.9×10^{-4}
$A34$	3.0420	8.4102	1.5031	1.0000	6.0738	-1.7827	2.1×10^{-4}
$A35$	3.0911	8.2099	1.5032	1.0000	6.1135	-1.7797	2.2×10^{-4}

Table 3.4.   Individual Stellar Components along DWD Inspiral Sequence 'A'

Model	M_1 ($M_\odot$)	R_1 (10^9 cm)	$\rho_{\mathrm{max}}^{i=1}$ (10^9 cgs)	$f_{\mathrm{RL}}^{i=1}$	$J_{\mathrm{spin}}^{i=1}$ (10^{50} cgs)	M_2 ($M_\odot$)	R_2 (10^9 cm)	$\rho_{\mathrm{max}}^{i=2}$ (10^9 cgs)	$f_{\mathrm{RL}}^{i=2}$	$J_{\mathrm{spin}}^{i=2}$ (10^{50} cgs)
$A1$	0.7522	0.7841	6.745	1.0000	0.2562	0.7522	0.7841	6.745	1.0000	0.2562
$A2$	0.7522	0.7840	6.745	0.9969	0.2559	0.7522	0.7840	6.745	0.9969	0.2559
$A3$	0.7518	0.7835	6.745	0.9838	0.2540	0.7518	0.7835	6.745	0.9838	0.2540
$A4$	0.7515	0.7831	6.745	0.9736	0.2526	0.7515	0.7831	6.745	0.9736	0.2526
$A5$	0.7516	0.7825	6.758	0.9614	0.2509	0.7516	0.7825	6.758	0.9615	0.2509
$A6$	0.7516	0.7817	6.771	0.9471	0.2489	0.7516	0.7817	6.771	0.9471	0.2489
$A7$	0.7516	0.7798	6.805	0.9134	0.2441	0.7516	0.7798	6.805	0.9134	0.2441
$A8$	0.7515	0.7790	6.820	0.8942	0.2414	0.7515	0.7790	6.820	0.8942	0.2414
$A9$	0.7514	0.7780	6.837	0.8739	0.2384	0.7514	0.7780	6.837	0.8739	0.2384
$A10$	0.7514	0.7769	6.855	0.8523	0.2353	0.7514	0.7769	6.855	0.8523	0.2353
$A11$	0.7513	0.7759	6.876	0.8303	0.2320	0.7513	0.7758	6.876	0.8303	0.2320
$A12$	0.7515	0.7735	6.924	0.7838	0.2250	0.7515	0.7735	6.924	0.7838	0.2250
$A13$	0.7514	0.7724	6.944	0.7602	0.2213	0.7514	0.7724	6.944	0.7602	0.2213
$A14$	0.7516	0.7711	6.977	0.7367	0.2176	0.7516	0.7711	6.977	0.7367	0.2176
$A15$	0.7515	0.7701	6.992	0.7131	0.2138	0.7515	0.7701	6.992	0.7131	0.2138
$A16$	0.7513	0.7692	7.013	0.6903	0.2099	0.7513	0.7692	7.013	0.6903	0.2099

Table 3.4—Continued

Model	M_1 $(M_\odot)$	R_1 (10^9 cm)	$\rho_{\max}^{i=1}$ (10^9 cgs)	$f_{\text{RL}}^{i=1}$	$J_{\text{spin}}^{i=1}$ (10^{50} cgs)	M_2 $(M_\odot)$	R_2 (10^9 cm)	$\rho_{\max}^{i=2}$ (10^9 cgs)	$f_{\text{RL}}^{i=2}$	$J_{\text{spin}}^{i=2}$ (10^{50} cgs)
$A17$	0.7515	0.7668	7.062	0.6440	0.2020	0.7515	0.7668	7.062	0.6440	0.2020
$A18$	0.7514	0.7658	7.083	0.6215	0.1980	0.7514	0.7658	7.083	0.6215	0.1980
$A19$	0.7514	0.7650	7.103	0.5998	0.1940	0.7514	0.7650	7.103	0.5998	0.1940
$A20$	0.7516	0.7637	7.137	0.5779	0.1901	0.7516	0.7637	7.137	0.5779	0.1901
$A21$	0.7515	0.7629	7.153	0.5568	0.1861	0.7515	0.7629	7.153	0.5567	0.1861
$A22$	0.7515	0.7611	7.198	0.5160	0.1781	0.7515	0.7611	7.198	0.5160	0.1781
$A23$	0.7515	0.7603	7.214	0.4964	0.1742	0.7515	0.7603	7.214	0.4964	0.1742
$A24$	0.7514	0.7596	7.234	0.4774	0.1703	0.7514	0.7596	7.234	0.4774	0.1703
$A25$	0.7515	0.7585	7.251	0.4583	0.1664	0.7515	0.7585	7.251	0.4583	0.1664
$A26$	0.7514	0.7579	7.271	0.4404	0.1625	0.7514	0.7579	7.271	0.4404	0.1625
$A27$	0.7514	0.7571	7.290	0.4231	0.1587	0.7514	0.7571	7.290	0.4231	0.1587
$A28$	0.7514	0.7562	7.309	0.4057	0.1548	0.7514	0.7562	7.309	0.4057	0.1548
$A29$	0.7516	0.7548	7.349	0.3733	0.1476	0.7516	0.7548	7.349	0.3733	0.1476
$A30$	0.7515	0.7541	7.363	0.3575	0.1440	0.7515	0.7541	7.363	0.3576	0.1440
$A31$	0.7513	0.7540	7.363	0.3478	0.1424	0.7513	0.7541	7.363	0.3518	0.1424
$A32$	0.7516	0.7529	7.397	0.3282	0.1369	0.7516	0.7529	7.397	0.3282	0.1369
$A33$	0.7515	0.7522	7.412	0.3142	0.1333	0.7515	0.7522	7.412	0.3142	0.1333
$A34$	0.7516	0.7517	7.425	0.3005	0.1299	0.7516	0.7517	7.425	0.3005	0.1299
$A35$	0.7516	0.7511	7.438	0.2874	0.1265	0.7516	0.7510	7.440	0.2873	0.1265

Table 3.5.   DWD Inspiral Sequence 'B': $M_{\text{tot}} = 1.5 M_\odot$; $q = 2/3$

Model	a (10^9 cm)	Ω (10^{-2} s^{-1})	M_{tot} $(M_\odot)$	q	J_{tot} (10^{50} cgs)	E_{tot} (10^{50} erg)	VE
$B1$	2.6679	10.2944	1.5042	0.6671	5.5888	-1.9460	6.0×10^{-4}
$B2$	2.6743	10.2576	1.5043	0.6667	5.5931	-1.9460	6.1×10^{-4}
$B3$	2.6819	10.2106	1.5037	0.6667	5.5951	-1.9436	6.0×10^{-4}
$B4$	2.6923	10.1491	1.5033	0.6664	5.6001	-1.9419	6.1×10^{-4}
$B5$	2.7039	10.0831	1.5036	0.6663	5.6090	-1.9420	6.0×10^{-4}
$B6$	2.7177	10.0040	1.5034	0.6665	5.6174	-1.9401	6.1×10^{-4}
$B7$	2.7487	9.8330	1.5035	0.6665	5.6403	-1.9383	6.2×10^{-4}
$B8$	2.7687	9.7249	1.5035	0.6664	5.6542	-1.9372	6.2×10^{-4}
$B9$	2.7902	9.6104	1.5033	0.6665	5.6684	-1.9348	6.3×10^{-4}
$B10$	2.8138	9.4879	1.5033	0.6664	5.6851	-1.9333	6.3×10^{-4}
$B11$	2.8388	9.3609	1.5033	0.6663	5.7034	-1.9318	6.4×10^{-4}
$B12$	2.8654	9.2290	1.5032	0.6665	5.7224	-1.9295	6.4×10^{-4}
$B13$	2.9196	8.9712	1.5034	0.6665	5.7638	-1.9267	6.5×10^{-4}
$B14$	2.9514	8.8246	1.5033	0.6665	5.7864	-1.9241	6.8×10^{-4}
$B15$	2.9850	8.6746	1.5031	0.6665	5.8108	-1.9215	6.8×10^{-4}
$B16$	3.0199	8.5240	1.5034	0.6664	5.8380	-1.9201	6.9×10^{-4}
$B17$	3.0567	8.3680	1.5031	0.6665	5.8638	-1.9170	7.0×10^{-4}
$B18$	3.0949	8.2123	1.5032	0.6665	5.8928	-1.9147	7.0×10^{-4}
$B19$	3.1350	8.0548	1.5034	0.6663	5.9238	-1.9132	7.2×10^{-4}
$B20$	3.1766	7.8955	1.5031	0.6665	5.9543	-1.9097	7.4×10^{-4}
$B21$	3.2199	7.7355	1.5032	0.6666	5.9870	-1.9074	7.5×10^{-4}
$B22$	3.2653	7.5743	1.5034	0.6664	6.0218	-1.9056	7.8×10^{-4}
$B23$	3.3554	7.2699	1.5033	0.6667	6.0905	-1.9002	8.1×10^{-4}
$B24$	3.4062	7.1070	1.5034	0.6666	6.1285	-1.8978	8.1×10^{-4}
$B25$	3.4590	6.9440	1.5034	0.6665	6.1681	-1.8951	8.5×10^{-4}
$B26$	3.5133	6.7821	1.5032	0.6666	6.2078	-1.8917	8.6×10^{-4}
$B27$	3.5700	6.6211	1.5033	0.6665	6.2506	-1.8893	8.8×10^{-4}
$B28$	3.6285	6.4611	1.5034	0.6665	6.2948	-1.8867	9.2×10^{-4}
$B29$	3.6892	6.3010	1.5032	0.6666	6.3387	-1.8832	9.3×10^{-4}
$B30$	3.7520	6.1432	1.5033	0.6666	6.3860	-1.8809	9.6×10^{-4}
$B31$	3.8171	5.9860	1.5034	0.6665	6.4340	-1.8783	9.9×10^{-4}
$B32$	3.8846	5.8298	1.5032	0.6667	6.4828	-1.8747	1.0×10^{-3}
$B33$	3.9544	5.6759	1.5034	0.6666	6.5344	-1.8724	1.0×10^{-3}

Table 3.5—Continued

Model	a $(10^9$ cm$)$	Ω $(10^{-2}$ s$^{-1})$	M_{tot} $(M_\odot)$	q	J_{tot} $(10^{50}$ cgs$)$	E_{tot} $(10^{50}$ erg$)$	VE
$B34$	4.0270	5.5225	1.5034	0.6665	6.5874	-1.8698	1.1×10^{-3}
$B35$	4.1030	5.3681	1.5027	0.6666	6.6380	-1.8645	1.1×10^{-3}
$B36$	4.1801	5.2199	1.5031	0.6666	6.6951	-1.8628	1.1×10^{-3}
$B37$	4.2601	5.0741	1.5034	0.6666	6.7548	-1.8611	1.2×10^{-3}
$B38$	4.2667	5.0582	1.5030	0.6668	6.7529	-1.8596	1.1×10^{-3}
$B39$	4.3502	4.9129	1.5031	0.6667	6.8124	-1.8570	1.2×10^{-3}
$B40$	4.4375	4.7683	1.5032	0.6664	6.8739	-1.8548	1.2×10^{-3}
$B41$	4.5270	4.6269	1.5030	0.6666	6.9357	-1.8513	1.3×10^{-3}
$B42$	4.6192	4.4889	1.5032	0.6668	7.0011	-1.8487	1.3×10^{-3}
$B43$	4.7160	4.3508	1.5034	0.6666	7.0680	-1.8467	1.4×10^{-3}
$B44$	4.8164	4.2143	1.5031	0.6667	7.1344	-1.8429	1.4×10^{-3}
$B45$	4.9203	4.0808	1.5029	0.6668	7.2039	-1.8395	1.5×10^{-3}
$B46$	5.0281	3.9494	1.5029	0.6668	7.2752	-1.8366	1.5×10^{-3}
$B47$	5.1405	3.8227	1.5033	0.6665	7.3562	-1.8352	1.7×10^{-3}
$B48$	5.1467	3.8136	1.5032	0.6669	7.3567	-1.8347	1.6×10^{-3}
$B49$	5.2630	3.6870	1.5033	0.6670	7.4330	-1.8320	1.7×10^{-3}

Table 3.6. Individual Stellar Components along DWD Inspiral Sequence 'B'

Model	M_1 $(M_\odot)$	R_1 $(10^9$ cm$)$	$\rho_{max}^{i=1}$ $(10^9$ cgs$)$	$f_{RL}^{i=1}$	$J_{spin}^{i=1}$ $(10^{50}$ cgs$)$	M_2 $(M_\odot)$	R_2 $(10^9$ cm$)$	$\rho_{max}^{i=2}$ $(10^9$ cgs$)$	$f_{RL}^{i=2}$	$J_{spin}^{i=2}$ $(10^{50}$ cgs$)$
$B1$	0.9023	0.6345	17.049	0.1913	0.1289	0.6019	0.9117	3.076	1.0001	0.2004
$B2$	0.9026	0.6344	17.049	0.1898	0.1283	0.6017	0.9113	3.076	0.9908	0.1995
$B3$	0.9022	0.6345	17.049	0.1881	0.1278	0.6015	0.9108	3.076	0.9805	0.1982
$B4$	0.9022	0.6343	17.049	0.1856	0.1270	0.6012	0.9101	3.076	0.9667	0.1966
$B5$	0.9023	0.6343	17.047	0.1832	0.1261	0.6013	0.9090	3.083	0.9504	0.1948
$B6$	0.9021	0.6343	17.059	0.1803	0.1250	0.6013	0.9078	3.089	0.9314	0.1927
$B7$	0.9022	0.6340	17.082	0.1737	0.1228	0.6013	0.9056	3.108	0.8916	0.1882
$B8$	0.9022	0.6336	17.085	0.1694	0.1213	0.6012	0.9043	3.115	0.8677	0.1854
$B9$	0.9020	0.6336	17.100	0.1654	0.1198	0.6012	0.9029	3.123	0.8430	0.1825
$B10$	0.9021	0.6334	17.112	0.1610	0.1182	0.6011	0.9017	3.134	0.8181	0.1795
$B11$	0.9022	0.6334	17.121	0.1565	0.1165	0.6011	0.9003	3.144	0.7917	0.1764
$B12$	0.9020	0.6332	17.139	0.1520	0.1148	0.6012	0.8987	3.153	0.7650	0.1732
$B13$	0.9022	0.6329	17.162	0.1432	0.1114	0.6013	0.8963	3.175	0.7172	0.1670
$B14$	0.9021	0.6326	17.177	0.1383	0.1095	0.6012	0.8950	3.184	0.6907	0.1636
$B15$	0.9020	0.6324	17.195	0.1335	0.1076	0.6011	0.8935	3.194	0.6644	0.1602
$B16$	0.9022	0.6323	17.203	0.1288	0.1056	0.6012	0.8925	3.203	0.6403	0.1568
$B17$	0.9020	0.6323	17.222	0.1241	0.1036	0.6011	0.8914	3.213	0.6158	0.1534
$B18$	0.9020	0.6318	17.241	0.1192	0.1016	0.6012	0.8902	3.223	0.5916	0.1500
$B19$	0.9022	0.6316	17.246	0.1145	0.0995	0.6012	0.8887	3.233	0.5675	0.1465
$B20$	0.9019	0.6315	17.268	0.1099	0.0975	0.6012	0.8879	3.242	0.5448	0.1431
$B21$	0.9020	0.6311	17.287	0.1053	0.0955	0.6012	0.8866	3.251	0.5219	0.1397
$B22$	0.9022	0.6311	17.294	0.1009	0.0933	0.6012	0.8856	3.261	0.5003	0.1364
$B23$	0.9020	0.6307	17.340	0.0928	0.0895	0.6013	0.8837	3.280	0.4605	0.1301
$B24$	0.9021	0.6304	17.353	0.0885	0.0874	0.6013	0.8829	3.285	0.4408	0.1268

Table 3.6—Continued

Model	M_1 $(M_\odot)$	R_1 $(10^9$ cm$)$	$\rho_{\max}^{i=1}$ $(10^9$ cgs$)$	$f_{\mathrm{RL}}^{i=1}$	$J_{\mathrm{spin}}^{i=1}$ $(10^{50}$ cgs$)$	M_2 $(M_\odot)$	R_2 $(10^9$ cm$)$	$\rho_{\max}^{i=2}$ $(10^9$ cgs$)$	$f_{\mathrm{RL}}^{i=2}$	$J_{\mathrm{spin}}^{i=2}$ $(10^{50}$ cgs$)$
$B25$	0.9021	0.6302	17.362	0.0844	0.0853	0.6012	0.8823	3.294	0.4219	0.1235
$B26$	0.9019	0.6303	17.384	0.0806	0.0833	0.6013	0.8814	3.301	0.4029	0.1203
$B27$	0.9021	0.6301	17.398	0.0767	0.0812	0.6012	0.8804	3.309	0.3846	0.1171
$B28$	0.9021	0.6297	17.409	0.0729	0.0792	0.6013	0.8791	3.316	0.3661	0.1140
$B29$	0.9019	0.6298	17.432	0.0694	0.0772	0.6013	0.8790	3.323	0.3500	0.1109
$B30$	0.9021	0.6292	17.445	0.0657	0.0752	0.6013	0.8780	3.330	0.3334	0.1078
$B31$	0.9021	0.6293	17.457	0.0624	0.0732	0.6013	0.8772	3.336	0.3174	0.1048
$B32$	0.9019	0.6288	17.480	0.0591	0.0712	0.6013	0.8768	3.343	0.3024	0.1019
$B33$	0.9020	0.6289	17.495	0.0560	0.0693	0.6013	0.8762	3.349	0.2879	0.0990
$B34$	0.9021	0.6291	17.504	0.0531	0.0674	0.6013	0.8753	3.355	0.2734	0.0961
$B35$	0.9017	0.6287	17.504	0.0501	0.0655	0.6011	0.8749	3.355	0.2597	0.0932
$B36$	0.9019	0.6285	17.531	0.0473	0.0636	0.6012	0.8746	3.365	0.2469	0.0905
$B37$	0.9021	0.6283	17.542	0.0447	0.0617	0.6013	0.8739	3.371	0.2344	0.0878
$B38$	0.9017	0.6284	17.542	0.0445	0.0616	0.6013	0.8739	3.371	0.2334	0.0875
$B39$	0.9018	0.6280	17.572	0.0419	0.0598	0.6013	0.8732	3.378	0.2212	0.0848
$B40$	0.9021	0.6276	17.572	0.0394	0.0579	0.6011	0.8728	3.378	0.2096	0.0822
$B41$	0.9018	0.6273	17.601	0.0371	0.0562	0.6012	0.8723	3.387	0.1984	0.0796
$B42$	0.9018	0.6274	17.631	0.0350	0.0545	0.6014	0.8712	3.392	0.1875	0.0771
$B43$	0.9021	0.6267	17.645	0.0328	0.0527	0.6013	0.8710	3.398	0.1774	0.0746
$B44$	0.9019	0.6272	17.645	0.0309	0.0510	0.6012	0.8709	3.398	0.1677	0.0722
$B45$	0.9017	0.6272	17.682	0.0290	0.0494	0.6012	0.8704	3.407	0.1583	0.0698
$B46$	0.9017	0.6265	17.682	0.0271	0.0478	0.6012	0.8699	3.407	0.1491	0.0674
$B47$	0.9020	0.6266	17.697	0.0254	0.0462	0.6012	0.8696	3.416	0.1405	0.0652
$B48$	0.9018	0.6266	17.726	0.0254	0.0461	0.6014	0.8695	3.419	0.1400	0.0650
$B49$	0.9018	0.6260	17.758	0.0237	0.0445	0.6015	0.8691	3.421	0.1318	0.0628

Table 3.7. DWD Inspiral Sequence 'C': $M_{\text{tot}} = 1.5M_{\odot}$; $q = 1/2$

Model	a (10^9 cm)	Ω (10^{-2} s^{-1})	M_{tot} ($M_{\odot}$)	q	J_{tot} (10^{50} cgs)	E_{tot} (10^{50} erg)	VE
$C1$	3.1807	7.9054	1.5043	0.5001	5.5568	-2.1635	1.2×10^{-3}
$C2$	3.1814	7.9025	1.5044	0.5001	5.5574	-2.1638	1.2×10^{-3}
$C3$	3.1865	7.8822	1.5039	0.5002	5.5582	-2.1615	1.2×10^{-3}
$C4$	3.2070	7.8041	1.5033	0.4997	5.5671	-2.1594	1.2×10^{-3}
$C5$	3.2208	7.7539	1.5038	0.4997	5.5780	-2.1605	1.2×10^{-3}
$C6$	3.2376	7.6922	1.5036	0.4998	5.5883	-2.1584	1.2×10^{-3}
$C7$	3.2573	7.6213	1.5034	0.4999	5.6009	-2.1566	1.2×10^{-3}
$C8$	3.2800	7.5404	1.5035	0.4998	5.6150	-2.1561	1.2×10^{-3}
$C9$	3.3051	7.4547	1.5038	0.4996	5.6329	-2.1566	1.2×10^{-3}
$C10$	3.3321	7.3618	1.5033	0.4999	5.6489	-2.1529	1.2×10^{-3}
$C11$	3.3617	7.2631	1.5032	0.4999	5.6680	-2.1511	1.2×10^{-3}
$C12$	3.4235	7.0659	1.5036	0.4999	5.7108	-2.1497	1.3×10^{-3}
$C13$	3.4601	6.9530	1.5036	0.4998	5.7349	-2.1483	1.3×10^{-3}
$C14$	3.4985	6.8369	1.5032	0.4999	5.7590	-2.1448	1.3×10^{-3}
$C15$	3.5391	6.7190	1.5033	0.5000	5.7867	-2.1432	1.3×10^{-3}
$C16$	3.5823	6.5967	1.5035	0.4998	5.8157	-2.1426	1.4×10^{-3}
$C17$	3.6274	6.4733	1.5035	0.4998	5.8463	-2.1405	1.4×10^{-3}
$C18$	3.6747	6.3467	1.5032	0.5000	5.8765	-2.1370	1.4×10^{-3}
$C19$	3.7245	6.2193	1.5032	0.4999	5.9102	-2.1353	1.4×10^{-3}
$C20$	3.7764	6.0914	1.5036	0.4998	5.9468	-2.1349	1.5×10^{-3}
$C21$	3.8311	5.9605	1.5034	0.4998	5.9826	-2.1320	1.5×10^{-3}
$C22$	3.8878	5.8291	1.5032	0.5001	6.0197	-2.1286	1.5×10^{-3}
$C23$	3.9475	5.6967	1.5032	0.4999	6.0592	-2.1266	1.6×10^{-3}
$C24$	4.0093	5.5658	1.5036	0.4998	6.1025	-2.1261	1.6×10^{-3}
$C25$	4.0742	5.4324	1.5034	0.4999	6.1443	-2.1232	1.7×10^{-3}
$C26$	4.1412	5.2995	1.5031	0.5001	6.1874	-2.1194	1.7×10^{-3}
$C27$	4.2115	5.1674	1.5031	0.5000	6.2340	-2.1173	1.8×10^{-3}
$C28$	4.2844	5.0359	1.5035	0.4999	6.2833	-2.1166	1.8×10^{-3}
$C29$	4.3605	4.9039	1.5035	0.4999	6.3327	-2.1146	1.9×10^{-3}
$C30$	4.4396	4.7723	1.5031	0.5001	6.3821	-2.1100	1.9×10^{-3}
$C31$	4.5218	4.6425	1.5031	0.5001	6.4355	-2.1076	2.0×10^{-3}
$C32$	4.6077	4.5130	1.5033	0.5000	6.4912	-2.1066	2.0×10^{-3}
$C33$	4.6142	4.5018	1.5040	0.4996	6.4939	-2.1098	2.0×10^{-3}
$C34$	4.7030	4.3735	1.5033	0.5001	6.5480	-2.1038	2.1×10^{-3}
$C35$	4.7960	4.2462	1.5030	0.5001	6.6056	-2.1003	2.2×10^{-3}
$C36$	4.8938	4.1186	1.5027	0.5000	6.6642	-2.0972	2.2×10^{-3}

Table 3.8.   Individual Stellar Components along DWD Inspiral Sequence 'C'

Model	M_1 $(M_\odot)$	R_1 $(10^9$ cm$)$	$\rho_{max}^{i=1}$ $(10^9$ cgs$)$	$f_{RL}^{i=1}$	$J_{spin}^{i=1}$ $(10^{50}$ cgs$)$	M_2 $(M_\odot)$	R_2 $(10^9$ cm$)$	$\rho_{max}^{i=2}$ $(10^9$ cgs$)$	$f_{RL}^{i=2}$	$J_{spin}^{i=2}$ $(10^{50}$ cgs$)$
$C1$	1.0028	0.5542	31.824	0.0627	0.0800	0.5015	1.0110	1.767	1.0000	0.1613
$C2$	1.0029	0.5541	31.824	0.0626	0.0799	0.5015	1.0108	1.767	0.9987	0.1613
$C3$	1.0025	0.5544	31.824	0.0624	0.0798	0.5014	1.0104	1.767	0.9927	0.1607
$C4$	1.0025	0.5546	31.824	0.0612	0.0790	0.5009	1.0093	1.767	0.9703	0.1586
$C5$	1.0027	0.5541	31.806	0.0602	0.0784	0.5010	1.0081	1.772	0.9536	0.1571
$C6$	1.0025	0.5543	31.812	0.0593	0.0778	0.5011	1.0068	1.776	0.9334	0.1553
$C7$	1.0023	0.5547	31.834	0.0583	0.0771	0.5011	1.0051	1.780	0.9109	0.1534
$C8$	1.0024	0.5541	31.845	0.0568	0.0762	0.5010	1.0035	1.786	0.8873	0.1512
$C9$	1.0028	0.5540	31.823	0.0554	0.0753	0.5010	1.0021	1.791	0.8634	0.1489
$C10$	1.0023	0.5544	31.847	0.0542	0.0744	0.5010	1.0007	1.796	0.8375	0.1464
$C11$	1.0022	0.5541	31.878	0.0527	0.0734	0.5010	0.9993	1.801	0.8112	0.1438
$C12$	1.0024	0.5537	31.901	0.0497	0.0713	0.5011	0.9961	1.814	0.7593	0.1388
$C13$	1.0025	0.5537	31.901	0.0480	0.0701	0.5010	0.9943	1.819	0.7309	0.1360
$C14$	1.0022	0.5539	31.934	0.0465	0.0689	0.5010	0.9933	1.824	0.7048	0.1332
$C15$	1.0022	0.5537	31.965	0.0448	0.0677	0.5011	0.9919	1.829	0.6777	0.1303
$C16$	1.0025	0.5533	31.971	0.0431	0.0664	0.5010	0.9905	1.836	0.6507	0.1274
$C17$	1.0024	0.5533	31.982	0.0415	0.0651	0.5010	0.9887	1.841	0.6239	0.1245

t

Table 3.8—Continued

Model	M_1 ($M_\odot$)	R_1 (10^9 cm)	$\rho_{\max}^{i=1}$ (10^9 cgs)	$f_{\mathrm{RL}}^{i=1}$	$J_{\mathrm{spin}}^{i=1}$ (10^{50} cgs)	M_2 ($M_\odot$)	R_2 (10^9 cm)	$\rho_{\max}^{i=2}$ (10^9 cgs)	$f_{\mathrm{RL}}^{i=2}$	$J_{\mathrm{spin}}^{i=2}$ (10^{50} cgs)
$C18$	1.0021	0.5534	32.020	0.0399	0.0639	0.5010	0.9873	1.847	0.5983	0.1216
$C19$	1.0022	0.5532	32.053	0.0383	0.0625	0.5010	0.9861	1.852	0.5728	0.1187
$C20$	1.0025	0.5530	32.057	0.0366	0.0612	0.5011	0.9850	1.857	0.5488	0.1158
$C21$	1.0024	0.5530	32.072	0.0351	0.0598	0.5010	0.9834	1.863	0.5242	0.1129
$C22$	1.0021	0.5525	32.115	0.0335	0.0585	0.5011	0.9827	1.867	0.5012	0.1100
$C23$	1.0021	0.5530	32.152	0.0320	0.0572	0.5010	0.9815	1.873	0.4788	0.1072
$C24$	1.0025	0.5528	32.158	0.0305	0.0558	0.5011	0.9804	1.877	0.4571	0.1044
$C25$	1.0024	0.5522	32.175	0.0290	0.0544	0.5010	0.9793	1.882	0.4357	0.1015
$C26$	1.0020	0.5524	32.223	0.0276	0.0531	0.5011	0.9786	1.886	0.4154	0.0988
$C27$	1.0021	0.5523	32.267	0.0262	0.0517	0.5011	0.9775	1.891	0.3951	0.0960
$C28$	1.0024	0.5515	32.281	0.0248	0.0503	0.5011	0.9761	1.895	0.3755	0.0933
$C29$	1.0024	0.5515	32.291	0.0235	0.0489	0.5011	0.9753	1.899	0.3572	0.0906
$C30$	1.0020	0.5518	32.342	0.0223	0.0476	0.5011	0.9746	1.903	0.3393	0.0879
$C31$	1.0020	0.5516	32.397	0.0211	0.0463	0.5011	0.9739	1.907	0.3219	0.0853
$C32$	1.0022	0.5510	32.425	0.0199	0.0450	0.5011	0.9727	1.911	0.3049	0.0827
$C33$	1.0029	0.5505	32.425	0.0197	0.0448	0.5011	0.9727	1.911	0.3041	0.0825
$C34$	1.0021	0.5511	32.462	0.0187	0.0435	0.5011	0.9722	1.915	0.2883	0.0800
$C35$	1.0019	0.5508	32.522	0.0176	0.0422	0.5011	0.9720	1.919	0.2735	0.0775
$C36$	1.0018	0.5508	32.522	0.0166	0.0409	0.5009	0.9711	1.919	0.2582	0.0750

itemized in Tables 3.3 - 3.8. Along sequence 'A' (Figure 3.2), both components of the binary system are of equal size and display identical degrees of tidal distortion because the mass ratio $q = 1$. Along sequences 'B' and 'C' (Figures 3.3 and 3.4, respectively), however, the primary star (on the left in each figure panel) is noticeably smaller and less distorted than the secondary star.
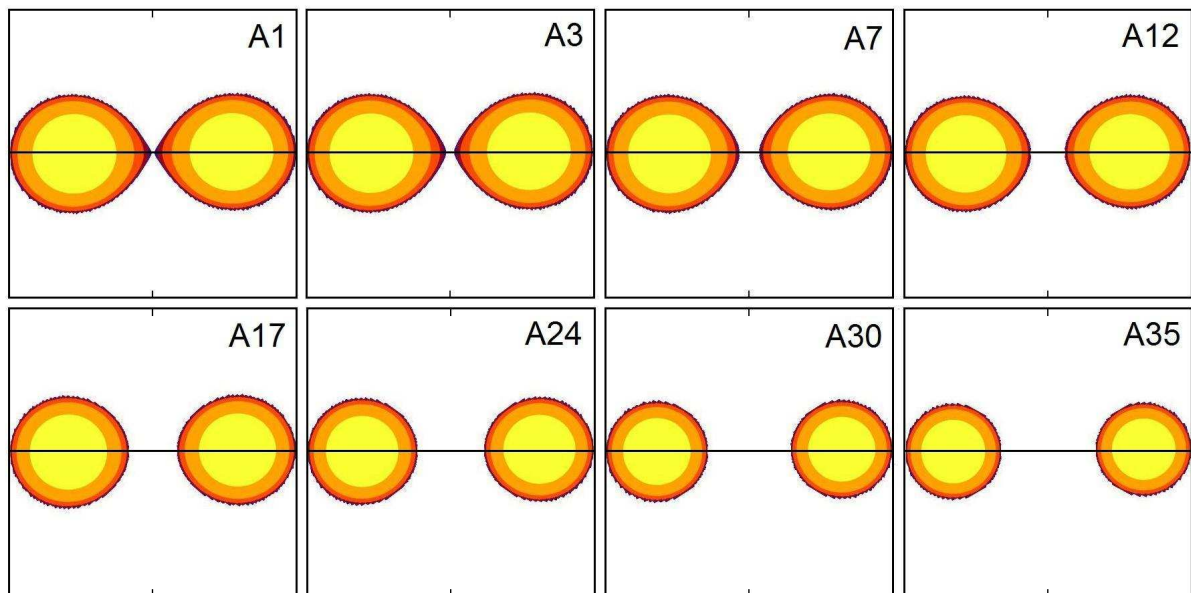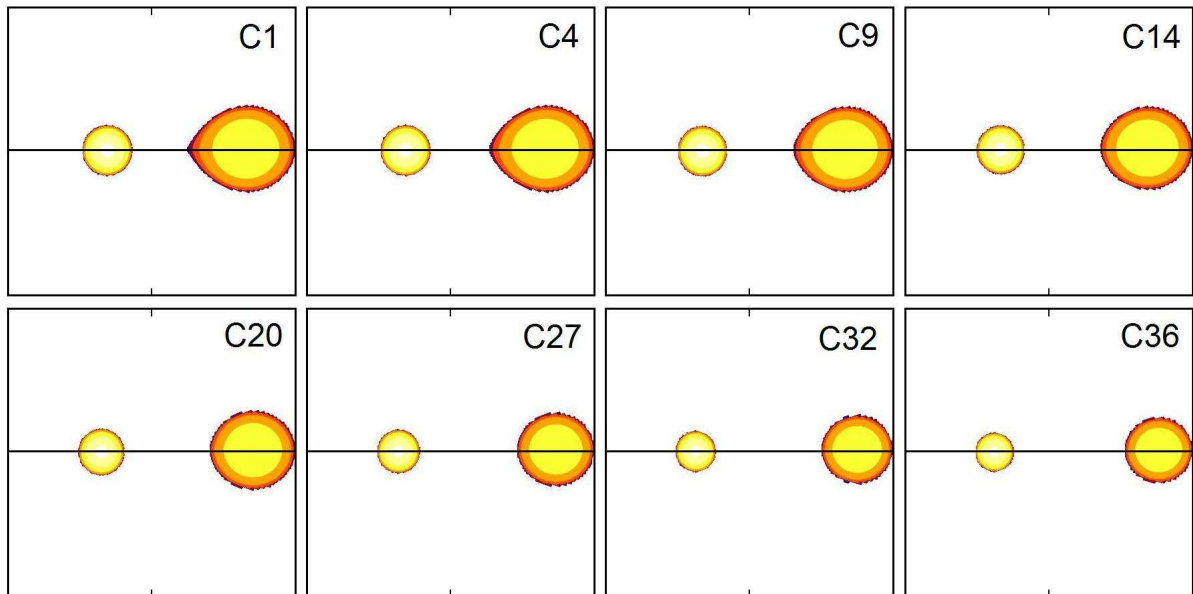

Figure 3.2 Density contours in the equatorial plane are shown for eight separate ZTWD binary models with increasing separation along inspiral sequence 'A' ($M_{\text{tot}} = 1.5 M_{\odot}$; $q = 1$). Labels in the upper-right-hand corner of each panel identify each model by number according to its corresponding position along the sequence as itemized in Tables 3.3 and 3.4.

Figure 3.5 has been constructed from the data detailed in Tables 3.3 and 3.4 for binary sequence 'A.' Specifically, the diamond symbols in the top two panels and in the bottom panel of this figure show, respectively, how the binary system's total angular momentum, J_{tot}, total energy, E_{tot}, and orbital angular velocity, Ω, vary with orbital separation along this sequence; and the third panel from the top shows how the Roche-lobe filling factor, f_{RL}^{i}, varies with orbital separation for both the primary star (diamonds) and the secondary
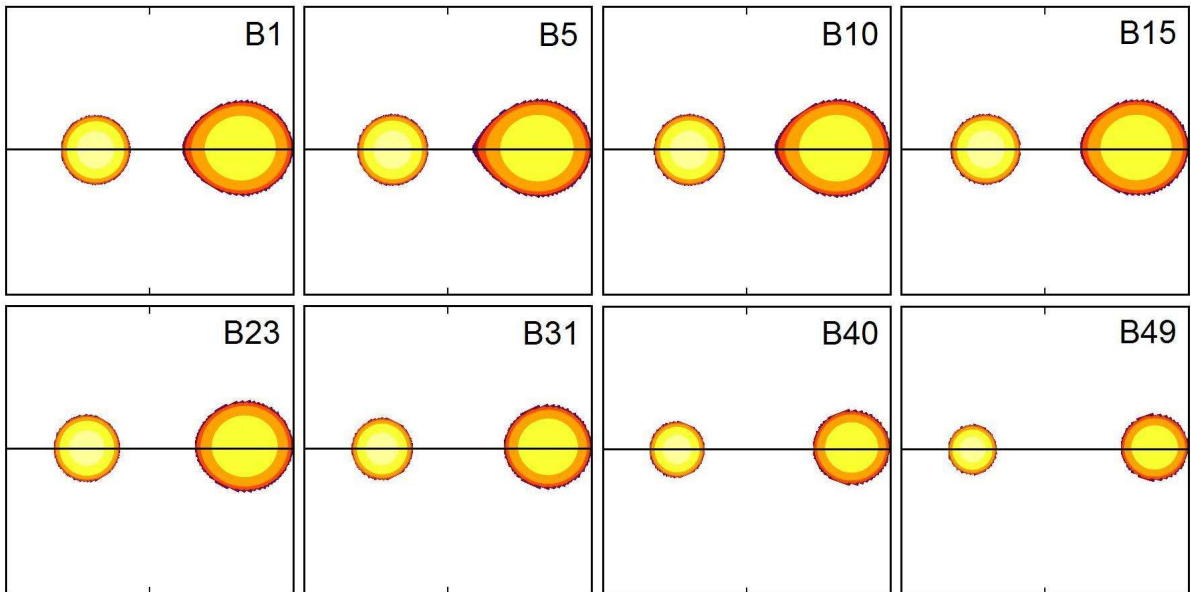
Figure 3.3 Density contours in the equatorial plane are shown for eight separate ZTWD binary models with increasing separation along inspiral sequence 'B' ($M_{\text{tot}} = 1.5 M_\odot$; $q = 2/3$). Labels in the upper-right-hand corner of each panel identify each model by number according to its corresponding position along the sequence as itemized in Tables 3.5 and 3.6.

star (asterisks). Figures 3.6 and 3.7 have been similarly constructed from the data detailed, respectively, in Tables 3.5 and 3.6, and in Tables 3.7 and 3.8.

Following the lead of New & Tohline (1997), in constructing Figures 3.5 - 3.7 we have normalized our tabulated values of J_{tot} and E_{tot} to the quantities,

$$J_{\text{norm}} \equiv (GM_{0.75}^3 R_{0.75})^{1/2} = 4.0735 \times 10^{50} \text{ g cm}^2 \text{ s}^{-1}, \tag{3.2}$$

$$E_{\text{norm}} \equiv \frac{GM_{0.75}^2}{R_{0.75}} = 2.0119 \times 10^{50} \text{ erg}, \tag{3.3}$$

where $R_{0.75} = 7.4244 \times 10^8$ cm is the radius of a spherical ZTWD whose mass is $M_{0.75} = 0.7522 \ M_\odot$ as tabulated in Table 3.2. Also, at each separation our tabulated values of Ω have been normalized to the Keplerian orbital frequency,

$$\Omega_{\text{K}} = \left(\frac{2GM_{0.75}}{a^3} \right)^{1/2}. \tag{3.4}$$

Figure 3.4 Density contours in the equatorial plane are shown for eight separate ZTWD binary models with increasing separation along inspiral sequence 'C' ($M_{\text{tot}} = 1.5 M_\odot$; $q = 1/2$). Labels in the upper-right-hand corner of each panel identify each model by number according to its corresponding position along the sequence as itemized in Tables 3.7 and 3.8.

In all three figures, values of the orbital separation have been specified (bottom horizontal axis) in units of 10^9 cm and (top horizontal axis) as normalized to the radius of a spherical ZTWD having the mass of the system's secondary star as tabulated in Table 3.2, that is, $R_{0.75} \equiv 7.424 \times 10^8$ cm, $R_{0.60} = 8.671 \times 10^8$ cm and $R_{0.50} = 9.638 \times 10^8$ cm.

New & Tohline (1997) have previously constructed inspiral sequences for *equal-mass* DWD binary systems in which the structure of the individual component stars is governed by the Chandrasekhar ZTWD equation of state (2.1). The sequences published by New & Tohline (1997) cover a wide range of total masses. The one that most closely resembles our sequence 'A' (our only equal-mass sequence) has $M_{\text{tot}} = 1.63 M_\odot$; the functional behavior of $E_{\text{tot}}(a)$ and $J_{\text{tot}}(a)$ for this sequence is presented in Figure 16 of New & Tohline (1997). Along this $M_{\text{tot}} = 1.63 M_\odot$ sequence, the two stars first make contact with their respective Roche lobes at a normalized separation of approximately 2.825 (see also Figure 5 of New &

Tohline 1997). This is completely consistent with the behavior of our sequence 'A,' where contact occurs (model A1) when $a/R_{0.75} = 2.823$.

The DWD sequences constructed by New & Tohline (1997) all extend to separations smaller than the point of first contact, as their SCF technique allowed them to build over-contact (common envelope) equal-mass binaries. Their functions $E_{\text{tot}}(a)$ and $J_{\text{tot}}(a)$ display a quadratic behavior along the over-contact segment of each sequence, passing through a minimum at a binary separation smaller than the point of first contact. None of our three sequences show this behavior because we have not attempted to construct models past the initial point of contact. Indeed, it seems unlikely that equilibrium configurations exist at smaller separations except when the system mass ratio is precisely $q = 1$.

For each of our DWD binary sequences, it is useful to compare the displayed functional behavior of $J_{\text{tot}}(a)$ from our numerical models against the behavior predicted by two simplified models. In the case of two point masses in circular orbit, the total angular momentum J_{pm} is given simply by the system's orbital angular momentum, that is,

$$
\begin{aligned}
J_{\text{pm}} = J_{\text{orb}} &= M_1 \varpi_1^2 \Omega_{\text{K}} + M_2 \varpi_2^2 \Omega_{\text{K}} \\
&= \frac{q}{(1+q)^2} \Big[G M_{\text{tot}}^3 a \Big]^{1/2}
\end{aligned}
\tag{3.5}
$$

This function, normalized to J_{norm}, is displayed by the solid curve in the top panels of Figures 3.5 - 3.7. An even more realistic representation of the function $J_{\text{tot}}(a)$ can be obtained by adding an approximate representation for the spin angular momentum, $I_i \Omega$, of both stars to the point-mass expression for J_{orb}. If we assume that both stars retain a spherical structure while spinning at the Keplerian orbital frequency, Ω_{K}, the appropriate expression for the total "spinning sphere" system angular momentum is,

$$
\begin{aligned}
J_{ss} &= J_{\text{orb}} + (I_1 + I_2)\Omega_{\text{K}} = J_{\text{orb}} + \Big(k_1 M_1 R_1^2 + k_2 M_2 R_2^2 \Big) \Omega_{\text{K}} \\
&= J_{\text{pm}} \left\{ 1 + \frac{(1+q)}{q} \Big[k_1 \Big(\frac{R_1}{a} \Big)^2 + q k_2 \Big(\frac{R_2}{a} \Big)^2 \Big] \right\},
\end{aligned}
\tag{3.6}
$$

where, in addition to q, values of (the constants) R_i and k_i appropriate for each binary sequence can be obtained from Table 3.2. Function (3.6), normalized to J_{norm}, is displayed by the dot-dashed curve in the top panels of Figures 3.5 - 3.7. Analytic expression (3.5) predicts that $J_{\mathrm{tot}} \propto a^{1/2}$. Through a correction factor, Eq. (3.6) displays a somewhat more complex behavior. Overall, our SCF model sequences match Eq. (3.6) particularly well. The largest deviation arises in all cases at the smallest separations; the slope of the SCF-generated $J_{\mathrm{tot}}(a)$ function flattens somewhat as the secondary star approaches contact with its Roche lobe, that is, as $f_{\mathrm{RL}}^{i=2} \to 1$.

The functional dependence of each system's total energy, $E_{\mathrm{tot}}(a)$, can be understood in a similar fashion. Considering only the kinetic and gravitational potential energy of two point masses in circular orbit, we obtain,

$$E_{\mathrm{orb}} \;=\; K_{\mathrm{orb}} + W_{\mathrm{orb}} = -K_{\mathrm{orb}} = -\frac{1}{2}\left[\frac{q}{(1+q)^2}\right]\frac{GM_{\mathrm{tot}}^2}{a}\,, \tag{3.7}$$

where we have used the virial relation $(2K_{\mathrm{orb}} + W_{\mathrm{orb}}) = 0$. While this a^{-1} functional dependence explains the general $E_{\mathrm{tot}}(a)$ behavior exhibited in Figures 3.5 - 3.7 by our numerically constructed model sequences, expression (3.7) is missing a nontrivial shift in the overall energy scale that is set by the binding energies of the two stars, namely,

$$E_{\mathrm{b}} \;=\; \sum_{i=1}^{2}\left(W^i + U^i\right). \tag{3.8}$$

Based on the properties of the spherical stellar models provided in Table 3.2, the appropriate energy shift for sequences 'A,' 'B,' and 'C' is, respectively, $E_b = -1.551 \times 10^{50}$ ergs, -1.698×10^{50} ergs, and -1.963×10^{50} ergs. Adding E_{b} to E_{orb} provides what we will refer to as the "point mass" total system energy,

$$E_{\mathrm{pm}} \;=\; -\frac{1}{2}\left[\frac{q}{(1+q)^2}\right]\frac{GM_{\mathrm{tot}}^2}{a} + E_{\mathrm{b}}\,. \tag{3.9}$$

This analytic function, normalized to E_{norm}, is displayed as a solid curve in the plots of E_{tot} versus a shown in Figures 3.5 - 3.7. An improved approximation that we will refer to as

the "spinning sphere" total system energy can be obtained by adding the rotational kinetic energy of both stars, assuming they remain spherically symmetric and spin uniformly with the Keplerian orbital frequency. Specifically,

$$
\begin{aligned}
E_{\text{ss}} &= E_{\text{pm}} + \sum_{i=1}^{2}\left(\frac{1}{2}I_i\Omega_{\text{K}}^2\right) \\
&= E_{\text{b}} + E_{\text{orb}}\left\{1 - \frac{(1+q)}{q}\left[k_1\left(\frac{R_1}{a}\right)^2 + qk_2\left(\frac{R_2}{a}\right)^2\right]\right\}.
\end{aligned} \tag{3.10}
$$

This function, normalized to E_{norm}, is displayed as a dot-dashed curve in the plots of E_{tot} versus a shown in Figures 3.5 - 3.7. Expression (3.10) describes particularly well the variation of E_{tot} with separation displayed by our numerically constructed binary sequences 'B' and 'C.' We note, however, that all three of our sequences show that the total system energy drops slightly below the behavior predicted by Eq. (3.10) at the smallest separations.

The curve outlined by asterisks in the third panel from the top of Figures 3.5 - 3.7 shows that $f_{\text{RL}}^{i=2}$ steadily increases from a value ~ 0.2 to a value of 1.0 at the smallest separation along all three inspiral sequences, implying that the secondary star has made contact with its Roche lobe. For comparison, the curve outlined by diamonds in the same panel of these three figures shows how the Roche-lobe filling factor of the primary star varies along each sequence. The value of $f_{\text{RL}}^{i=1}$ does not climb above 0.063 for sequence 'C' or above 0.191 for sequence 'B,' reflecting the fact that in both cases the primary star is significantly more massive — and, hence, it has a significantly smaller radius — than the secondary star. For inspiral sequence 'A,' $f_{\text{RL}}^{i=1}(a)$ displays an identical behavior to $f_{\text{RL}}^{i=2}(a)$ because the primary and secondary stars have equal masses.

The bottom panel of Figures 3.5 - 3.7 displays the behavior of the normalized orbital frequency Ω/Ω_{K} as a function of binary separation derived from our three numerically constructed inspiral sequences. At the smallest separations, our models show that the orbital frequency is always $\sim 0.5\%$ higher than predicted by the "point-mass" Keplerian frequency. Our equal-mass sequence exhibits the largest deviation at contact; specifically, for model

'A1,' we find $\Omega = 1.0085\,\Omega_{\mathrm{K}}$. As the separation is increased along each sequence, the figures show that $\Omega/\Omega_{\mathrm{K}}$ approaches unity, as expected. However, at a sufficiently wide separation, each of our sequences displays a tiny discontinuous drop in the orbital frequency, followed by further decline that ultimately falls below the local Keplerian value. We suspect this odd behavior at wide separations arises from the discrete nature of our grid calculations coupled with progressively fewer grid zones falling inside both stars — resulting in progressively poorer numerical resolution — at wider separations.

3.2 Contact Sequences

During a phase of stable mass transfer, a DWD binary system will evolve in such a way that the secondary star remains in marginal contact with its Roche lobe while it slowly transfers mass to the primary star. If the total mass of the system is conserved, then the evolution should proceed along a sequence of synchronously rotating configurations in which M_{tot} is constant, $f_{\mathrm{RL}}^{i=2} = 1$, and q is steadily decreasing. Models $A1$, $B1$ and $C1$ can be viewed as representing three such configurations along a sequence whose total system mass is $M_{\mathrm{tot}} = 1.5 M_\odot$. In evolving from an initially equal-mass, contact configuration (model $A1$) to a semi-detached configuration with $q = 2/3$ (model $B1$), then on to a semi-detached configuration with $q = 1/2$ (model $C1$), the separation of such a system (measured in units of 10^9 cm) will increase from $a_9 = 2.10$, to $a_9 = 2.67$, then to $a_9 = 3.18$; and the system's orbital period ($P_{\mathrm{orb}} = 2\pi/\Omega$) will increase from 42.3 s to 61.0 s, then to 79.5 s.

It is clear, therefore, that our new SCF code can be used to construct model sequences that mimic the evolution of DWD systems undergoing slow, conservative mass-transfer. The models detailed in Tables 3.9 (sequence 'D') and 3.10 (sequence 'E') trace two such semi-detached sequences as the system mass ratio evolves from $q = 1$ to $q \lesssim 0.5$. For sequence 'D,' $M_{\mathrm{tot}} = 1.5 M_\odot$ and for sequence 'E,' $M_{\mathrm{tot}} = 1.0 M_\odot$. In the top two panels of Figures 3.8 and 3.9, data from Tables 3.9 and 3.10 have been plotted as diamond symbols to illustrate

Table 3.9. Semi-detached DWD Sequence 'D'; $M_{\text{tot}} = 1.5 M_\odot$

M_{tot} ($M_\odot$)	q	a (10^9 cm)	Ω (10^{-2} s^{-1})	J_{tot} (10^{50} cgs)	E_{tot} (10^{50} erg)	VE
1.5048	1.0000	2.1010	14.8472	5.3866	-1.8636	1.5×10^{-4}
1.5034	0.9508	2.1638	14.1787	5.4116	-1.8566	1.8×10^{-4}
1.5045	0.8994	2.2336	13.4444	5.4491	-1.8611	9.5×10^{-5}
1.5034	0.8507	2.3102	12.8287	5.4797	-1.8628	1.4×10^{-4}
1.5033	0.8007	2.3961	12.1414	5.5141	-1.8736	2.2×10^{-4}
1.5034	0.7504	2.4919	11.4431	5.5460	-1.8925	3.1×10^{-4}
1.5034	0.7004	2.5987	10.7442	5.5702	-1.9194	4.0×10^{-4}
1.5034	0.6504	2.7188	10.0382	5.5871	-1.9572	5.5×10^{-4}
1.5032	0.6004	2.8550	9.3217	5.5914	-2.0072	7.2×10^{-4}
1.5033	0.5503	3.0109	9.0670	5.5804	-2.0741	9.1×10^{-4}
1.5031	0.5004	3.1914	7.8907	5.5484	-2.1587	1.2×10^{-3}

how a and Ω vary with q while $f_{\text{RL}}^{i=2}$ is held to a value of unity (definition of a semi-detached binary) along these two fixed-mass sequences.

Up to now, the community has relied upon some relatively simple analytic expressions to approximate the behavior of, for example, $a(q)$ along conservative mass-transfer evolutionary trajectories. For example, by setting the radius of the secondary star as given by the Nauenberg mass-radius relation (A.14) equal to the Roche-lobe radius R_{RL} as defined in terms of a and q by the approximate relation provided by Eggleton (1983), namely,

$$R_{\text{RL}} = a\left[\frac{0.49q^{2/3}}{0.6q^{2/3} + \ln(1 + q^{1/3})}\right], \tag{3.11}$$

one obtains,

$$\frac{a}{R_\odot} \approx 0.0229(n_2 q^2)^{-1/3}(1 - n_2^{4/3})^{1/2}\left[0.6q^{2/3} + \ln(1 + q^{1/3})\right], \tag{3.12}$$

where,

$$n_2 \equiv \frac{q}{(1 + q)}\left(\frac{M_{\text{tot}}}{M_{\text{ch}}}\right). \tag{3.13}$$

Table 3.10.   Semi-detached DWD Sequence 'E'; $M_{\mathrm{tot}} = 1.0 M_\odot$

M_{tot} ($M_\odot$)	q	a (10^9 cm)	Ω (10^{-2} s^{-1})	J_{tot} (10^{50} cgs)	E_{tot} (10^{50} erg)	VE
1.0030	1.0000	2.7109	8.2477	3.3579	-0.6657	1.7×10^{-4}
1.0024	0.9504	2.7778	7.9369	3.3687	-0.6642	1.6×10^{-4}
1.0019	0.9001	2.8641	7.5710	3.3850	-0.6636	2.1×10^{-4}
1.0022	0.8508	2.9380	7.2829	3.3983	-0.6659	2.2×10^{-4}
1.0024	0.8003	3.0161	6.9993	3.4073	-0.6698	2.2×10^{-4}
1.0024	0.7503	3.1165	6.6609	3.4163	-0.6751	2.6×10^{-4}
1.0024	0.7003	3.2294	6.3129	3.4212	-0.6828	3.3×10^{-4}
1.0023	0.6502	3.3569	5.9551	3.4204	-0.6934	3.9×10^{-4}
1.0023	0.6003	3.5026	5.5862	3.4123	-0.7074	4.7×10^{-4}
1.0022	0.5503	3.6696	5.2078	3.3943	-0.7254	5.6×10^{-4}
1.0021	0.5003	3.8649	4.8169	3.3644	-0.7484	6.8×10^{-4}
1.0020	0.4504	4.0955	4.4134	3.3184	-0.7773	8.0×10^{-4}

The function $a(q)$, defined by Eq. (3.12) for a given M_{tot}, has been plotted as a solid curve in the top panels of Figures 3.8 and 3.9, and the Keplerian orbital frequency associated with this separation (and relevant M_{tot}) has been plotted as a solid curve in the second panel of Figures 3.8 and 3.9. For both sequence 'D' and sequence 'E,' the analytically derived curves are consistently offset by 3 - 5% from our numerical model results. But overall, the analytically predicted functional behavior of $a(q)$ and $\Omega(q)$ is in very good agreement with our results. This is reassuring as it provides a degree of validation for both our numerical code and the approximations that were adopted by earlier investigators when deriving the more easily manipulated analytic expressions.

Finally, in the bottom two panels of Figures 3.8 and 3.9, the diamond symbols display the variation of J_{tot} and E_{tot} with q along sequence 'D' and sequence 'E,' respectively. The solid curve drawn in the $J_{\mathrm{tot}}(q)$ panel of both figures shows the behavior predicted by our "spinning sphere" expression for the total system angular momentum (3.6) when used in conjunction

with the $a(q, M_{\rm tot})$ behavior prescribed by Eq. (3.12). Again, for a given $M_{\rm tot}$ there appears to be very good agreement between the functional behavior of $J_{\rm tot}(q)$ displayed by our numerical model results and the analytic expressions. There is also a systematic offset between the two. In either case it is clear that, unlike the behavior displayed by $a(q)$ and $\Omega(q)$, the system's total angular momentum does not vary monotonically with q along a conservative mass-transfer evolutionary trajectory. Note, in particular, that if the system mass ratio q is initially close to unity, $J_{\rm tot}$ *increases* as q decreases along the displayed trajectory. This result is unphysical. It signifies that slow evolution along a synchronously rotating, conservative mass-transfer trajectory can occur only if, at the onset of mass-transfer, $q < q_{\rm crit}$, where the value of $q_{\rm crit}$ for a given $M_{\rm tot}$ is prescribed by the location of the maximum of the $J_{\rm tot}(q)$ curve. For our model sequences 'D' and 'E,' we see that $q_{\rm crit} \lesssim 2/3$, consistent with the mass-transfer stability limit that has already received much attention in the literature.
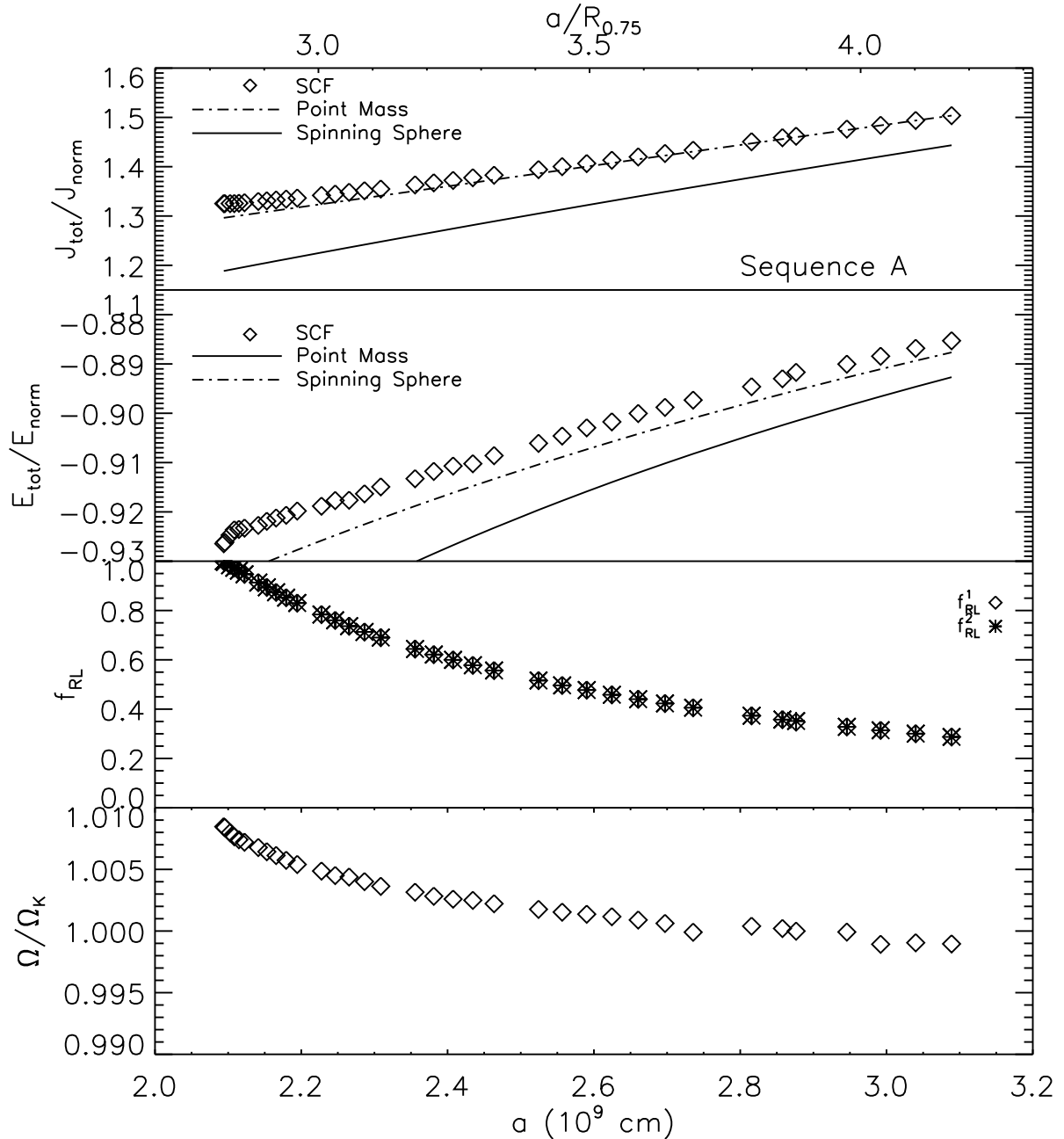
Figure 3.5 (*Top panel*) Normalized total angular momentum, $J_{\rm tot}/J_{\rm norm}$, (*second panel*) normalized total energy, $E_{\rm tot}/E_{\rm norm}$, (*third panel*) the Roche-lobe filling factor, $f_{\rm RL}$, for the secondary (asterisks) and primary (diamonds) stars, and (*bottom panel*) the normalized orbital angular velocity, $\Omega/\Omega_{\rm K}$, are plotted as a function of binary separation for models $A1$ through $A35$ along inspiral sequence 'A' ($M_{\rm tot} = 1.5M_\odot$; $q = 1$). Data for the individual models is drawn from Tables 3.3 and 3.4; the separation a is labeled in units of 10^9 cm along the bottom axis and as a ratio to $R_{0.75}$ along the top axis. The solid curves in the top two panels display the analytic functions $J_{\rm pm}(a)/J_{\rm norm}$ and $E_{\rm pm}(a)/E_{\rm norm}$ given, respectively, by Eqs. (3.5) and (3.9) for a "point-mass" sequence of the specified total mass and mass ratio; and the dot-dashed curves display the analytic functions $J_{\rm ss}(a)/J_{\rm norm}$ and $E_{\rm ss}(a)/E_{\rm norm}$ appropriate for a "spinning spheres" sequence given, respectively, by Eqs. (3.6) and (3.10).
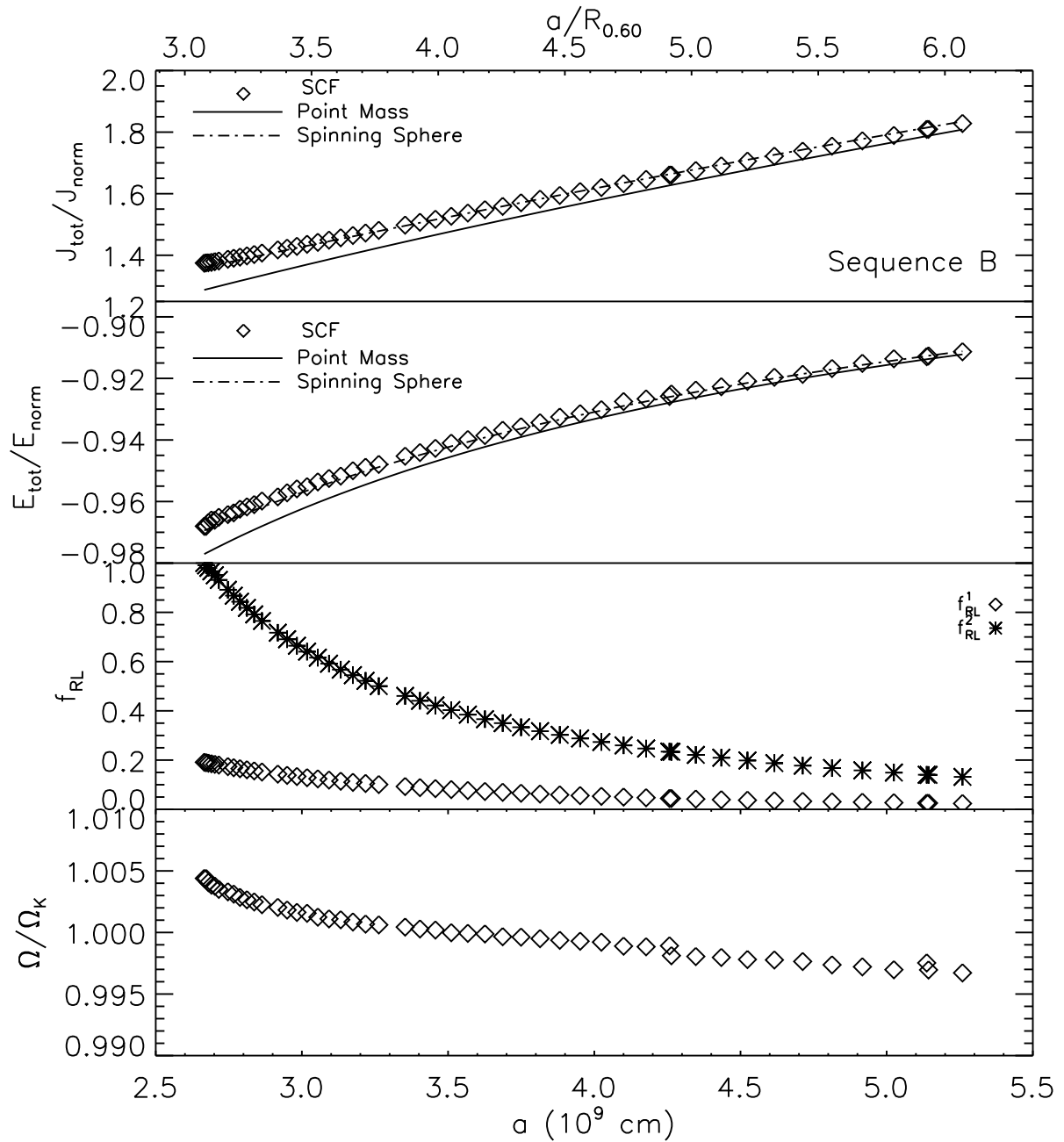
Figure 3.6 Same as Fig. 3.5 but for models $B1$ through $B49$ along the inspiral sequence 'B' ($M_{\text{tot}} = 1.5M_\odot$; $q = 2/3$), as tabulated in Tables 3.5 and 3.6; along the top axis, the separation a is labeled as a ratio to $R_{0.60}$.
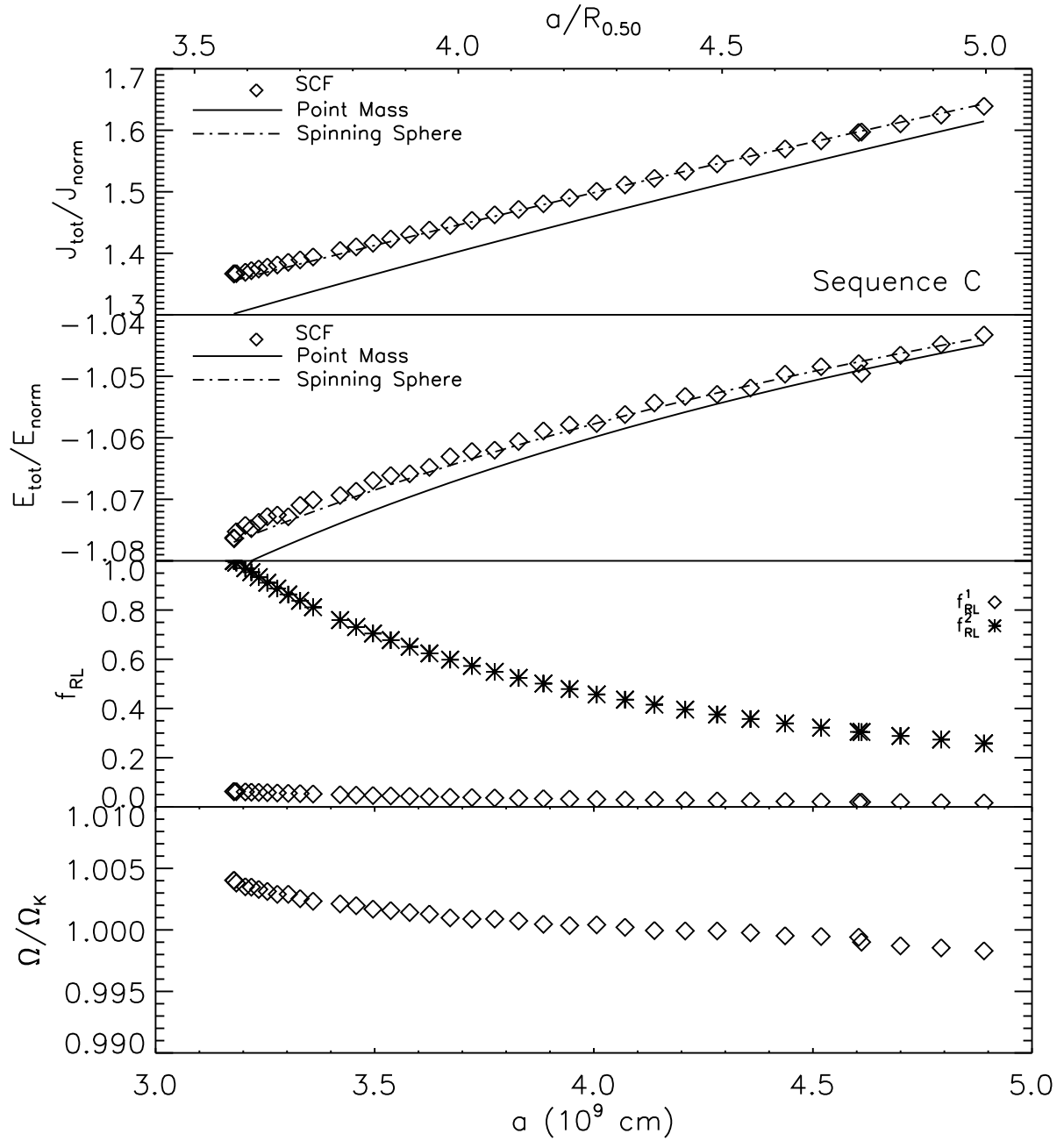
Figure 3.7 Same as Fig. 3.5 but for models $C1$ through $C36$ along the inspiral sequence 'C' ($M_{\text{tot}} = 1.5M_\odot$; $q = 1/2$), as tabulated in Tables 3.7 and 3.8; along the top axis, the separation a is labeled as a ratio to $R_{0.50}$.
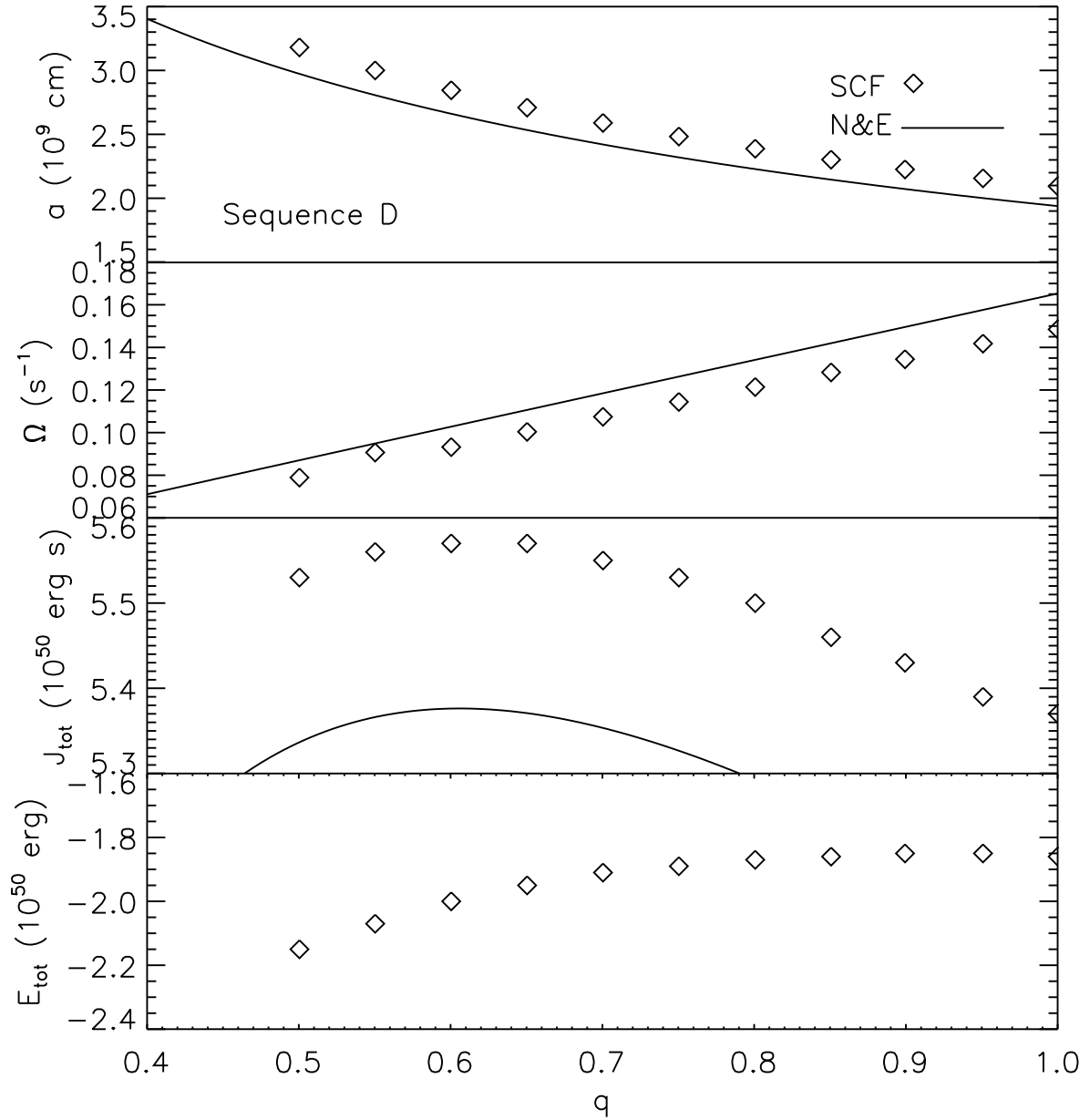
Figure 3.8 System parameters a, Ω, J_{tot}, and E_{tot} at contact as a function of mass ratio, q, for DWD systems having a total mass of $1.5 M_{\odot}$. Solid curves in the top three panels show predicted behavior based on Nauenberg's (1972) and Eggleton's (1983) approximate, analytic expressions as discussed in the text.
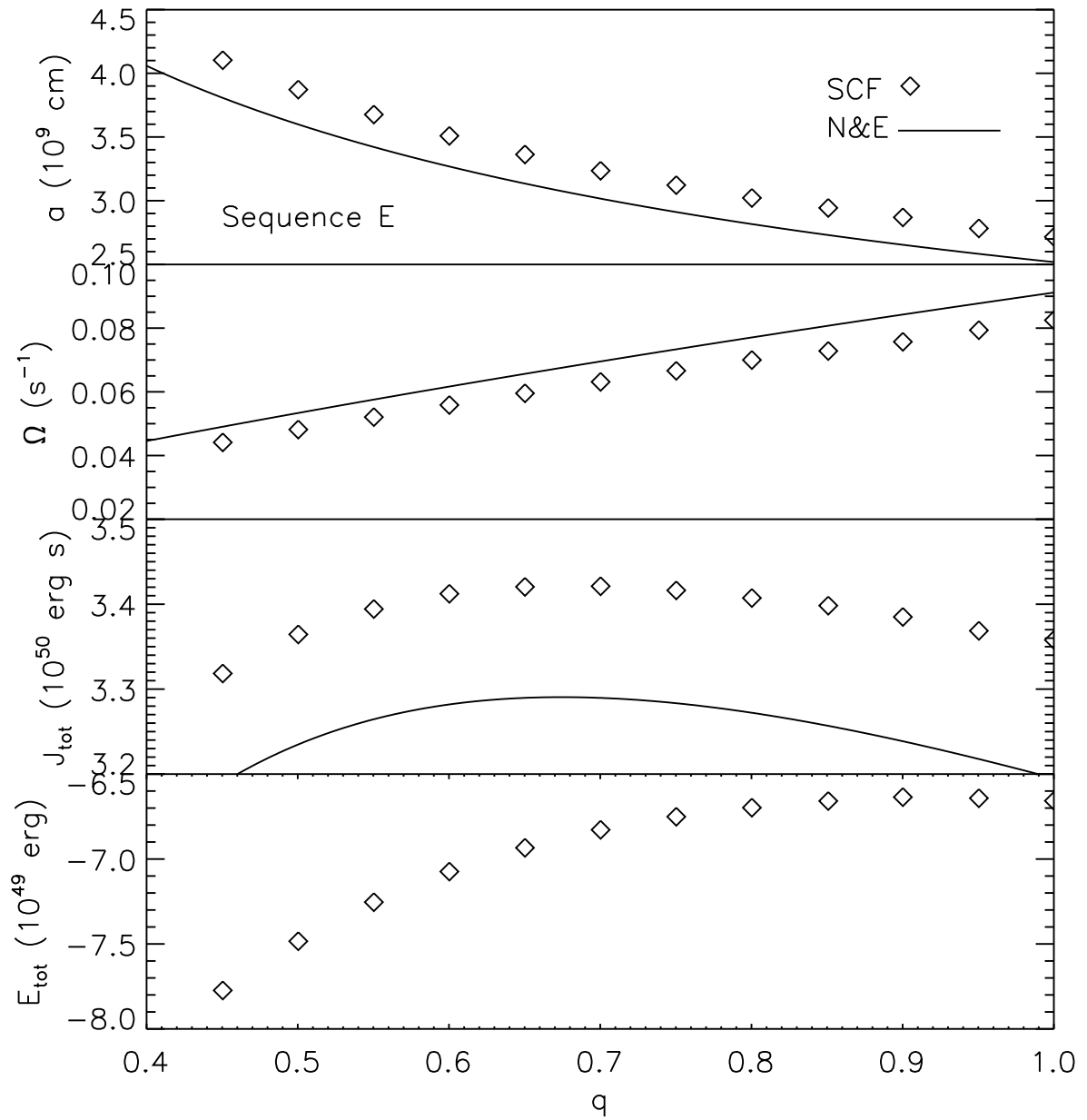
Figure 3.9 Same as Figure 3.8, but for DWD systems having a total mass of $1.0 M_\odot$.

4. Hydrodynamic Techniques

There are two different philosophies for implementing numerically evolving hydrodynamics. In the first the fluid is divided into parts, and individual components or particles of the fluid are tracked as they move through space. This approach is called the Lagrangian method and is the method used in the SPH simulations described in Section 1.5. In the second technique the region of interest is divided into a grid. The fluid values are defined for each cell on the grid and the fluid is evolved by advecting it through the grid. This grid based approach is the Eulerian method. Both the Lagrangian and Eulerian methods have advantages and disadvantages that need to be considered when selecting the better method for the problem to be solved. The Lagrangian method only tracks the fluid particles making it useful if you have voids in the simulation where there is little to no fluid because no computational time is used on these regions since there are no particles. However, the minimally resolvable density of the fluid is directly related to the number of particles used in the simulation. The Eulerian method must spend an equal amount of computational time on each cell regardless of the amount of fluid in the cell, even if it contains no fluid. If the problem does not match the chosen grid well, this can lead to large inefficiencies in the code from calculating areas of little physical interest. Since the Eulerian approach assigns scalar densities in all cells, the minimally resolvable density in a region is not tied to the number of cells, hence a greater range of densities can be covered in an Eulerian simulation than in the Lagrangian method. In the mass transferring DWD simulations the density of the material in the stream between the stars is many orders of magnitude lower than the central densities of the star, especially for the initial stream at the onset of mass transfer. By using the Eulerian method, we hope to be able to do more accurate simulations of the stream than

have been done with previous Lagrangian codes and therefore allow the system to evolve more slowly into the mass transfer.

4.1 Summary of Hydrodynamics Code

Our hydrodynamics code is a 3D explicit Eulerian hydrodynamics code developed principally by Patrick Motl. A detailed description of the code can be found in Motl (2001), Motl et al. (2002) and D'Souza et al. (2006). The code is implemented on a fixed uniform cylindrical grid, with the option of conducting the simulation in a rotating frame. Scalar quantities are defined on cell centers and vector quantities are defined on cell faces. The code tracks the following fluid quantities: density, ρ; angular momentum density, A_m; vertical momentum density, T_m; radial momentum density, S_m; and the entropy tracer, τ. The entropy tracer is defined in terms of the internal energy per unit mass, ϵ, the density, and the ratio of specific heats, γ by the expression,

$$\tau \equiv (\epsilon\rho)^{\frac{1}{\gamma}}. \tag{4.1}$$

In a later modification to the code the total energy density, E, is also tracked. The gravitational potential is calculated using a Fast Fourier Transform that reduces the Poisson equation to a group of independent 2D Helmholtz equations that are then solved using an alternating direction implicit (ADI) solver. The boundary conditions are calculated using the compact cylindrical Green's function expansion described in Cohl & Tohline (1999).

The main physical equations used to advance the simulation are:

$$\frac{\partial \rho}{\partial t} + \rho \vec{\nabla} \cdot \vec{v} = 0 \tag{4.2}$$

$$\frac{\partial S_m}{\partial t} + \nabla \cdot (S_m \vec{v}) = -\frac{\partial P}{\partial \varpi} - \rho \frac{\partial \Phi_{eff}}{\partial \varpi} + \frac{A_m^2}{\rho \varpi^3} + 2\Omega \frac{A_m}{\varpi} \tag{4.3}$$

$$\frac{\partial T_m}{\partial t} + \nabla \cdot (T_m \vec{v}) = -\frac{\partial P}{\partial z} - \rho \frac{\partial \Phi_{eff}}{\partial z} \tag{4.4}$$

$$\frac{\partial A_m}{\partial t} + \nabla \cdot (A_m \vec{v}) = -\frac{\partial P}{\partial \theta} - \rho \frac{\partial \Phi_{eff}}{\partial \theta} - 2\Omega S_m \varpi \tag{4.5}$$

$$\frac{\partial \tau}{\partial t} + \vec{\nabla} \cdot (\tau \vec{v}) = 0 \tag{4.6}$$

$$\Phi_{eff} = \Phi - \frac{1}{2}\Omega^2 \varpi^2 \tag{4.7}$$

$$\nabla^2 \Phi = 4\pi G\rho, \tag{4.8}$$

where Eq. (4.2) represents mass conservation, Eq. (4.3) - Eq. (4.5) represent conservation of the three momentum components, Eq. (4.6) is the energy conservation equation for an adiabatic fluid, Eq. (4.7) is the definition of the effective potential in the rotating frame, Φ_{eff}, and Eq. (4.8) couples the gravitational potential through the Poisson equation to the density. These equations are implemented numerically using second order accurate methods. For additional details and tests of the code see Motl (2001).

4.2 Zero Temperature Equation of State

The hydrodynamics code, hereafter hydrocode, was initially implemented for a polytropic equation of state (EOS). The polytropic EOS is defined as

$$P = \kappa \rho^{n+1/n} = \kappa \rho^\gamma \tag{4.9}$$

where κ is constant and n is the polytropic index. In the literature, n=3/2 polytropes are often used to approximate white dwarf structures. As shown in the top right panel of Figure 1.1, this may be acceptable for low-mass white dwarfs. The polytropic EOS is useful because it is simple to implement and allows scaling to different physical values after the calculation. However, there are weaknesses in using polytropes. The polytropic EOS does not enforce the proper mass-radius relation for white dwarfs and solutions with the more massive star being larger in radius than the less massive star are acceptable solutions to the polytropic EOS. Implementing a ZTWD EOS allows for more physically realistic DWD binaries to be investigated. We have implemented the ZTWD EOS into the current version of the hyrdrocode through a series of relatively minor changes. In the original version the pressure

for the polytropic gas was calculated from the entropy tracer. The use of the entropy tracer can be removed and the pressure can be calculated directly from the density using Eq. (2.1). Extra care must be taken to ensure that the hydrocode and SCF code are using the same normalizations for the dimensionless units used in the two codes. Additionally, the way the speed of sound is calculated needs to be updated to account for the new equation of state. The sound speed is used to calculate the maximum size of the timestep that will yield stable solutions. The adiabatic sound speed, c_s, is defined as,

$$c_s^2 = \frac{\partial P}{\partial \rho}. \tag{4.10}$$

Evaluating Eq. (4.10) using Eq. (2.1) for the pressure, the sound speed is shown to be,

$$c_s^2 = \frac{8A}{3B} \frac{\left(\frac{\rho}{B}\right)^{\frac{2}{3}}}{\left[1 + \left(\frac{\rho}{B}\right)^{\frac{2}{3}}\right]^{\frac{1}{2}}} = \frac{8A}{3B} \frac{x^2}{[1 + x^2]^{\frac{1}{2}}}. \tag{4.11}$$

The zero temperature equation of state is based on the assumption that the degeneracy pressure is significantly greater than the thermal pressure of the gas. In the initial equilibrium models this is a valid assumption. However, the accreting fluid can reach supersonic speeds as it approaches the surface of the accreting star. This will create shocks as it impacts the surface. These shocks generate large amounts of thermal energy, creating regions where the initial assumption may break down and the degeneracy pressure is no longer much greater than the thermal pressure. To solve this we will track two pressures, the degeneracy pressure, P_{deg}, and a thermal gas pressure, P_{gas}.

The fluid in the simulation is modeled using a combination of a zero-temperature Fermi fluid and an ideal gas. The total pressure, P, is the sum of pressure from the zero-temperature fluid, P_{deg}, and the ideal gas, P_{gas}. The zero temperature white dwarf equation of state gives the electron degeneracy pressure P_{deg} as a function of only the density, ρ, by the relation in Eq. (2.1). The internal energy density of the degenerate electron gas, E_{deg}, is given by the

relation,

$$E_{deg} = A\left[8x^3\left((x^2+1)^{1/2}-1\right) - \left(x(2x^2-3)(x^2+1)^{1/2}+3\sinh^{-1}x\right)\right], \quad (4.12)$$

as described in (Benz et al., 1990). Additionally, the kinetic energy density of the gas, E_k, in the rotating frame can be defined as

$$E_k = \frac{1}{2}\rho v^2, \quad (4.13)$$

where v is the velocity in the rotational frame. The total energy density of the fluid, E, is defined as

$$E = E_{deg} + E_{gas} + E_k, \quad (4.14)$$

where E_{gas} is the internal energy density of the ideal gas component of the fluid. Initially E_{gas} and P_{gas} are set to zero and E can be calculated directly from ρ and $\vec{v}$. Conservation of energy is given by

$$\frac{\partial E}{\partial t} + \nabla \cdot (E\vec{v}) = -\nabla \cdot (P\vec{v}) - \rho\vec{v} \cdot \nabla\Phi_{eff}. \quad (4.15)$$

The second term on the left is treated in the advection subroutine. The right hand side terms are then updated in the source subroutine through,

$$E_{n+1} = E_n - \left(\nabla \cdot (P\vec{v}) + \rho\vec{v} \cdot \nabla\Phi_{eff}\right)\delta t. \quad (4.16)$$

where E_n is the current value of energy density, E_{n+1} is the value being calculated, and δt is the time step size between the two iterations. The discrete form of the derivatives in Eq. (4.16) are

$$\begin{aligned}
\nabla \cdot (p\vec{v}) = {} & \frac{1}{\varpi d\varpi}\left[\left(\frac{\varpi P S_m}{\rho}\right)_{\varpi+\frac{1}{2}} - \left(\frac{\varpi P S_m}{\rho}\right)_{\varpi-\frac{1}{2}}\right] \\
& + \frac{1}{\varpi d\theta}\left[\left(\frac{P A_m}{\varpi\rho}\right)_{\theta+\frac{1}{2}} - \left(\frac{P A_m}{\varpi\rho}\right)_{\theta-\frac{1}{2}}\right] \\
& + \frac{1}{dz}\left[\left(\frac{P T_m}{\rho}\right)_{z+\frac{1}{2}} - \left(\frac{P T_m}{\rho}\right)_{z-\frac{1}{2}}\right]
\end{aligned} \quad (4.17)$$

and

$$\rho\vec{v}\cdot\nabla\Phi_{eff} = \frac{1}{4\varpi d\varpi}\left[\left(S_m\varpi\right)_{\varpi+\frac{1}{2}}+\left(S_m\varpi\right)_{\varpi-\frac{1}{2}}\right]\left[\Phi_{eff}^{\varpi+1}-\Phi_{eff}^{\varpi-1}\right] \quad (4.18)$$

$$= \frac{1}{4dz}\left[\left(T_m\right)_{z+\frac{1}{2}}+\left(T_m\right)_{z-\frac{1}{2}}\right]\left[\Phi_{eff}^{z+1}-\Phi_{eff}^{z-1}\right]$$

$$= \frac{1}{4\varpi^2 d\theta}\left[\left(A_m\right)_{\theta+\frac{1}{2}}+\left(A_m\right)_{\theta-\frac{1}{2}}\right]\left[\Phi_{eff}^{\phi+1}-\Phi_{eff}^{\phi-1}\right].$$

With updated values of E, E_{deg}, and E_k, the internal energy density of the ideal gas, can be calculated from Equation (4.14) as

$$E_{gas} = E - E_{deg} - E_k. \quad (4.19)$$

The pressure of the polytropic component of the gas, P_{gas}, is defined as

$$P_{gas} = (\gamma - 1)E_{gas}. \quad (4.20)$$

An additional factor is added to Eq. (4.20) to eliminate spurious effects from developing and dominating the behavior in the low density regions. These effects can develop since E_{gas} is initially derived from the difference of nearly identical numbers and its accuracy is limited by machine precision. In practice, the value of P_{gas} in the simulation is calculated through the relation

$$P_{gas} = (\gamma - 1)E_{gas}\left[1 - \frac{\rho_p}{\rho}\right] \text{ for } \rho \geq \rho_p$$

$$P_{gas} = 0 \text{ for } \rho < \rho_p \quad (4.21)$$

where ρ_p/ρ_* is defined to be 10^{-8} in the simulations presented in Chapter 5. The value of ρ_p/ρ_* was chosen by weighing the accuracy of the solution gained versus the reduction in timestep size required.

Table 4.1 displays the timestep size for 3 values of ρ_p/ρ_*: 10^{-7}, 10^{-8}, and 10^{-9}. The average timestep in the table is calculated for between approximately 0.25 and 0.35 orbital periods. The first column indicates the value of ρ_p/ρ_* used in the simulation, the second

column is the final timestep used in the calculation, the third is the time at the final timestep, the fourth and fifth columns are the initial timestep and time, and the final column shows the average value of the timestep over the 0.1 orbit interval. The three simulations were all conducted with identical initial conditions and with all parameters in the code identical except ρ_p/ρ_* was varied. The reduction in timestep between the first two is less than a factor of 2. When ρ_p/ρ_* is reduced by another order of magnitude, the timestep size is reduced by a factor of 5. This is a significant amount of additional time and will limit the number of orbits that are possible to run in a simulation. Figure 4.1 displays the value and time rate of change of the binary separation, a, as a function of time. Figure 4.2 displays the time rate of change of the total angular momentum and the value of central density of the accretor as a function of time for the simulations identified in Table 4.1. The values of the plotted quantities vary significantly when changing between ρ_p/ρ_* of 10^{-7} and 10^{-8}. The plots for 10^{-8} and 10^{-9} show much better agreement in all quantities. The close agreement between results when $\rho_p/\rho_* = 10^{-8}$ and $\rho_p/\rho_* = 10^{-9}$ and the increase of a factor of 5 in time led to the choice of ρ_p/ρ_* being 10^{-8}. Figure 4.3 shows the density (left) and pressure (right) contours at a time of t/P_o=0.4 for the 3 test simulations. The most obvious difference is in the $\rho_p/\rho_* = 10^{-9}$ case where, in the extremely low density regions, $\rho < 1\mathrm{g/cm}^3$, the pressure is dominated by the thermal pressure that is absent in the other two cases.

Finally, the total pressure of the fluid is then calculated as a sum of the two individual pressures,

$$P = P_{gas} + P_{deg}. \tag{4.22}$$

The temperature, T, of the gas can be calculated from P_{gas} using the ideal gas law giving,

$$T = \frac{P_{gas}\mu}{\rho\Re}, \tag{4.23}$$

where μ is the mean molecular weight and $\Re$ is the gas constant (8.3145×10^7 erg/deg $\cdot$ mol).

Table 4.1 Variation of timestep size with ρ_p/ρ_*

ρ_p/ρ_*	Timestep	Orbits	Timestep	Orbits	Average Timestep
10^{-7}	56800	0.3458	45300	0.2453	8.73133×10^{-6}
10^{-8}	60400	0.3460	43300	0.2460	5.84299×10^{-6}
10^{-9}	323600	0.3458	237900	0.2458	1.1668×10^{-6}
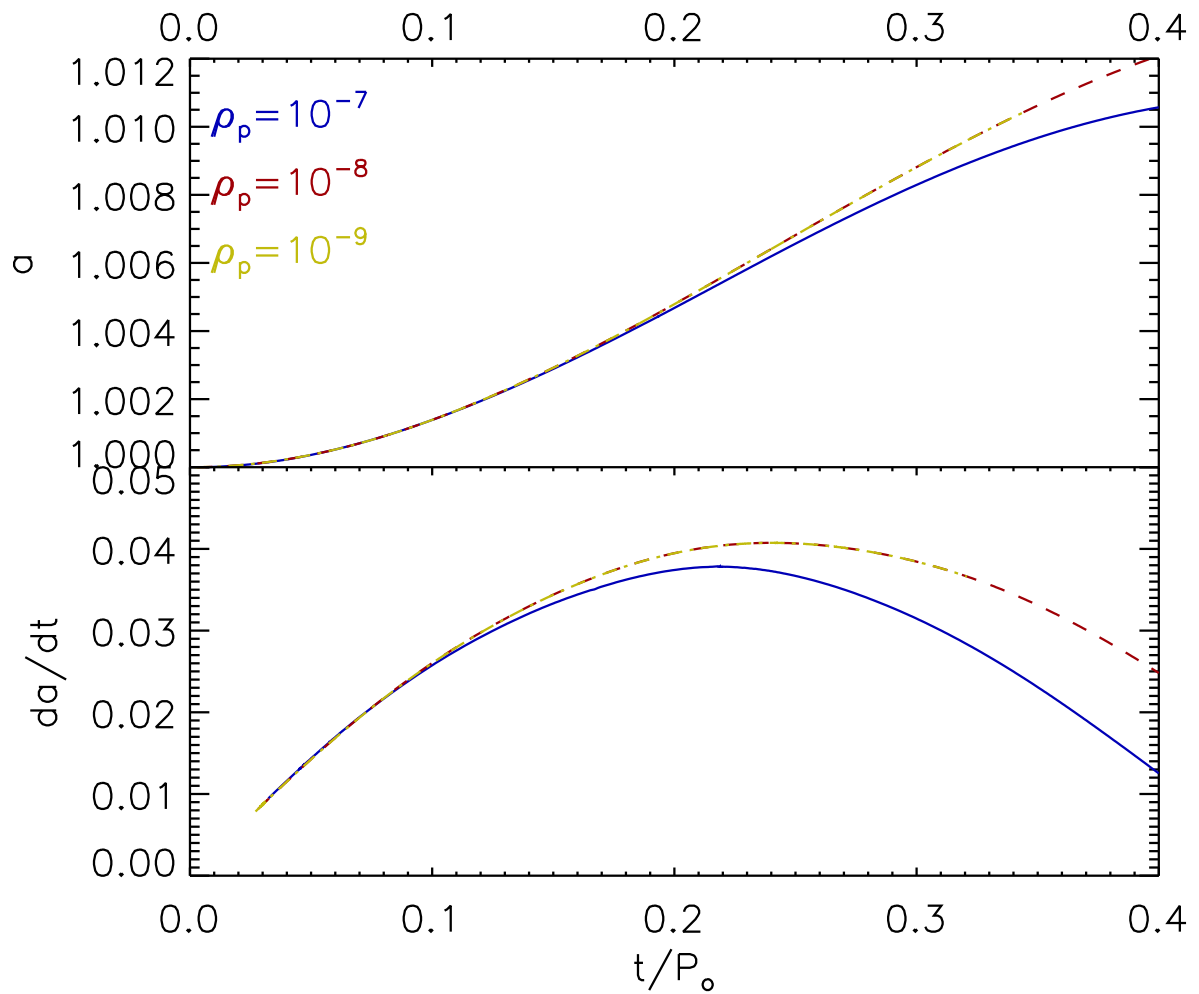
Figure 4.1 Top: The binary separation normalized to the initial separation as a function of time in orbital periods for a q=2/3 simulation. The three curves represent simulations run with identical conditions except that the value of ρ_p/ρ_* was varied to the value specified in the legend. Bottom: The time variation of the normalized separation for the same simulations in the top.
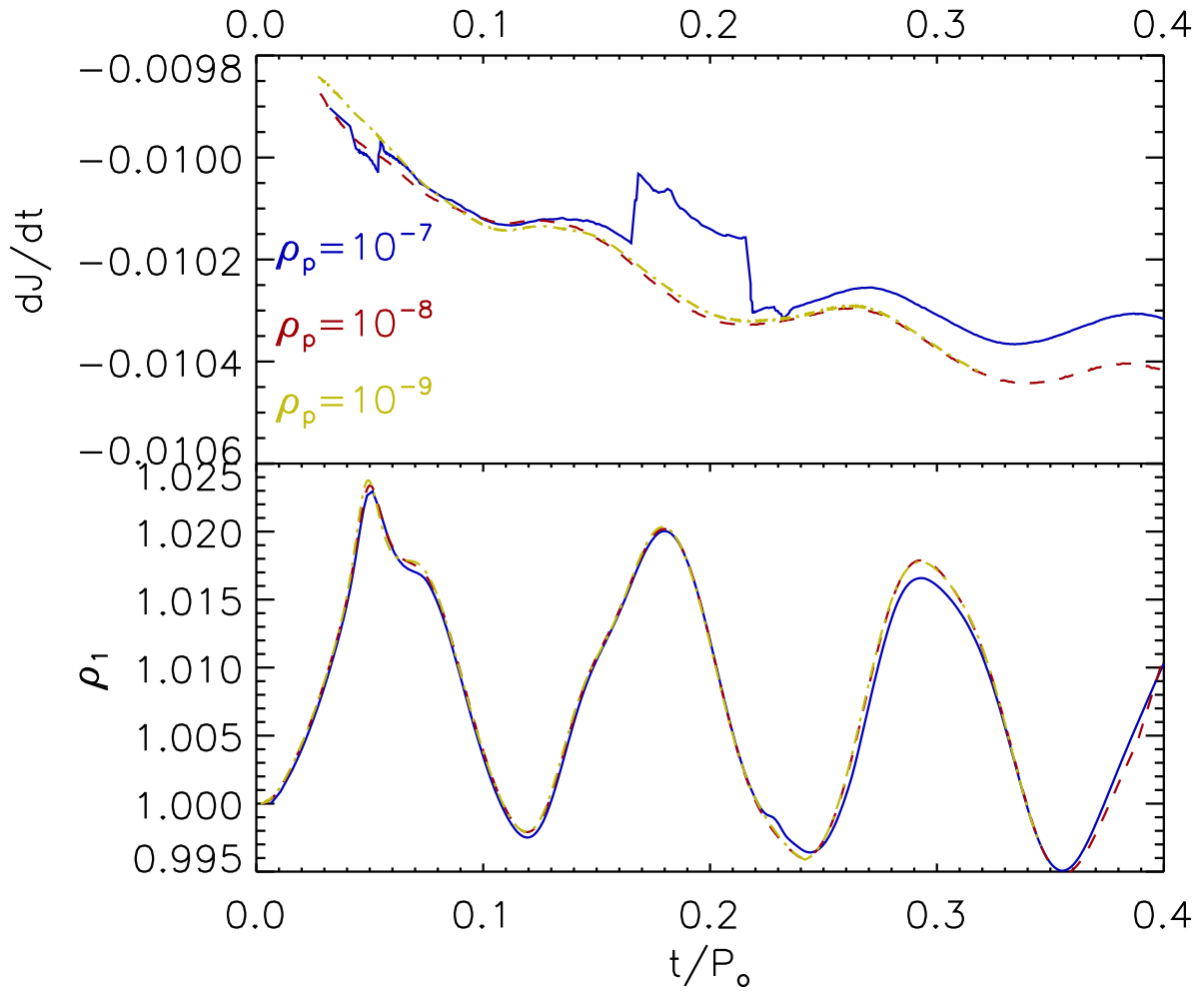
Figure 4.2 Same simulations as Figure 4.1. Top: Time variation of the total angular momentum normalized to the initial angular momentum. Bottom: The value of the central density of the accretor normalized to the initial central density.
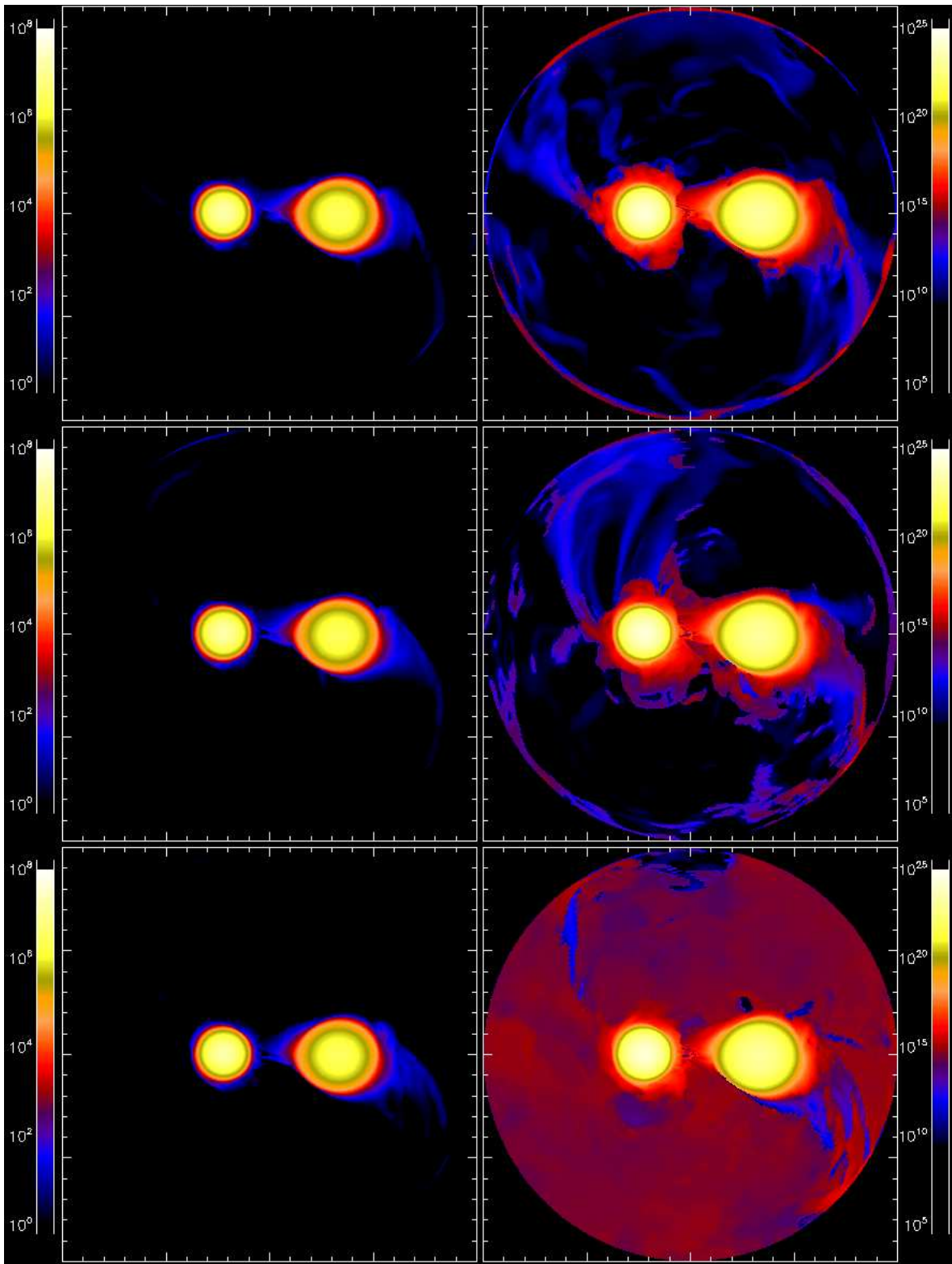
Figure 4.3 Equatorial slices of the simulations in Figures 4.1-4.2 0.4 orbital periods into the simulations. Top Row: The left image is the density contour in the equatorial plane in g/cm^3 for ρ_p/ρ_* of 10^{-7}. The right image is the pressure in dyne/cm^2 for the same ρ_p/ρ_*. Middle Row: Same as above except ρ_p/ρ_* equals 10^{-8}. Bottom Row: Same as above except ρ_p/ρ_* equals 10^{-9}.

5. Binary Merger Simulations

5.1 Previously Published Hydrocode Simulations

In D'Souza et al. (2006) and Motl et al. (2007) the stability of mass transfer in the binary systems is investigated using an n = 3/2 polytropic equation of state and the same hydrodynamics code used in this work. Direct impact accretion in systems with initial mass ratios of q= 1.3 and 0.5 are investigated in D'Souza et al. (2006), and Motl et al. (2007) examine the q=0.4 case. In these simulations nearly equilibrium initial conditions were created and the systems were driven into Roche lobe over fill. This driving was done by removing a small amount of angular momentum from each cell at each time step. The amount removed was set so that the angular momentum decreased at a constant rate, 1% per orbit being typical. The driving was then stopped once a desired level of contact is reached.

In the simulations q=1.3, after the initial driving was stopped, the mass transfer rate continued to grow throughout the simulation until the donor was tidally disrupted after 12 orbits. An initial binary system with a mass ratio of q=0.5 was evolved with several different driving rates. D'Souza et al. (2006) demonstrated that varying the level of Roche lobe overflow created by driving can substantially change the outcome of the system. The simulations were all driven at 1.0% for 2.7 orbits and then the driving was cut off immediately for case A, continued until 5.3 orbits for case B, and the driving was continued throughout for case C. In cases A and B, the mass transfer system underwent a period during which the binary separation remains steady and the mass transfer rate changes slowly. Eventually the separation increased and the system could no longer be followed due to numerical limitations of the grid. However, these periods of relatively stable mass transfer lasted for on the order of 10 orbits in case B and 30 orbits in case A. In the constantly driven case C, the mass

transfer rate increased throughout the simulation until the donor was disrupted in 8.5 orbits. In Motl et al. (2007) a system with an initial mass ratio of q=0.4 was driven at a rate of 1% for 1.16 orbits. In this case the mass transfer rate increased for the first 10 orbits and then began to decrease and leveled off to a constant rate at around 30 orbits. This system was followed through over 40 orbits with no indication that a merger or tidal disruption was imminent.

These results indicate that stable - or at least more slowly evolving - mass transfer than was seen in the previous SPH simulations is possible with a near equilibrium initial condition. However, the previous polytropic simulations with the hydrocode were done at significantly different mass ratios than the mass ratio in the published SPH simulations of DWDs.

5.2   q = 0.7 Polytrope

We have carried out a series of polytropic simulations to better compare the zero temperature equation of state results with polytropic results. The 3 polytropic simulations were all started with an identical initial state with a mass ratio of q=0.7. The first two simulations, Q0.7a and Q0.7b, were conducted using the same version of the hydrocode that was used in D'Souza et al. (2006) and in Motl et al. (2007), but with different initial conditions. The Q0.7a system was driven at a rate of 1% for 2.28 orbits. The density in the equatorial plane at 6 different times is shown in Figure 5.1. Plots of global scalar quantities and their derivatives are shown in Figures 5.2 - 5.5 for Q0.7a, Q0.7b, and Q0.7c.

As shown in Figure 5.3 by the blue curves, after the driving is stopped in the Q0.7a evolution, the binary separation steadily decreases as the mass transfer rate increases for 10 more orbits. During this time the angular momentum of the accretor (middle panel of Figure 5.4) is increasing as infalling donor material spins it up. After 12 orbits the separation decreases and mass transfer rate increases quickly as the donor is tidally disrupted and forms a thick disk around the accretor. In order to investigate whether the driving pushed the

system too far into contact for the system to have a chance to recover, as seen in some of the simulations in D'Souza et al. (2006), the system was restarted and driven for only 1.7 orbits in case Q0.7b (gold curves in Figures 5.2-5.5). As shown in Figure 5.5, this reduced the mass transfer rate by an order of magnitude between Q0.7a and Q0.7b within 1 orbital period after the driving was stopped. However, the mass transfer rate increased steadily while the binary separation decreased. After approximately 10 orbits the mass transfer rate reaches the rate initially present in Q0.7a. After this time, Q0.7b evolves almost identically to Q0.7a with an 8 orbit time shift. This supports the conclusion that for a system with q=0.7 initially, mass transfer is dynamically unstable and a merger/tidal disruption will result if mass transfer is begun regardless of the depth of initial contact.

The third case, Q0.7c, has identical driving to Q0.7a, but has a modified EOS that incorporates an ideal gas that can be heated through shocks. The addition of this heating creates a low density common envelope around the binary during the phase of mass transfer. The addition of this common envelope results in a higher mass transfer rate (red curves in Figure 5.5) in the early orbits and leads to the system merging somewhat sooner (red curves in Figure 5.3), but still in the same qualitative way as in Q0.7a and Q0.7b. All 3 polytropic simulations indicate that a DWD binary with a mass ratio of q=0.7 will result in a tidal disruption of the donor, although the system can survive in a mass transferring state for many orbits if the initial conditions are close enough to equilibrium and if the system is not driven too far into contact initially.

5.3   q = 2/3 Zero Temperature

The first hydrodynamic run using an initial model from the SCF code with a zero temperature EOS was conducted using the same EOS as presented in the SCF code. Model B3 (M_{tot}=1.5 $M_\odot$) from chapter 3.1 served as the initial model for this evolution which will hereafter be referred to as evolution Q2/3a. This ZTWD EOS only accounts for the electron
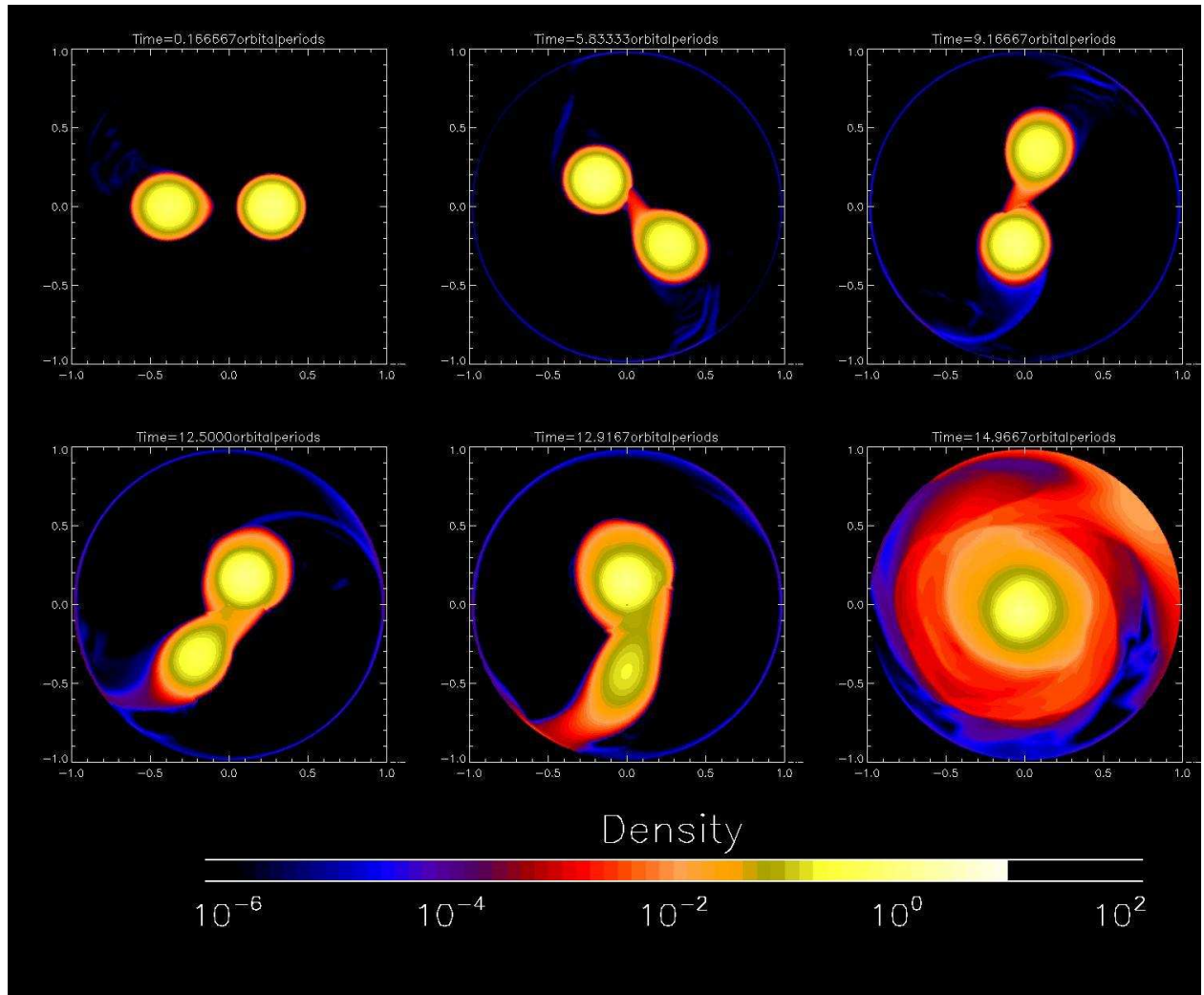
Figure 5.1 Mass density in the equatorial plane for simulation Q0.7a, an n=3/2 binary system with an initial mass ratio q=0.7. The binary is initially just beyond semi-contact and has angular momentum removed at 1% per orbit for 2.28 orbits to begin mass transfer. The mass transfer rate grows slowly until the last couple of orbits when the donor is tidally disrupted and a core-disk structure is created.
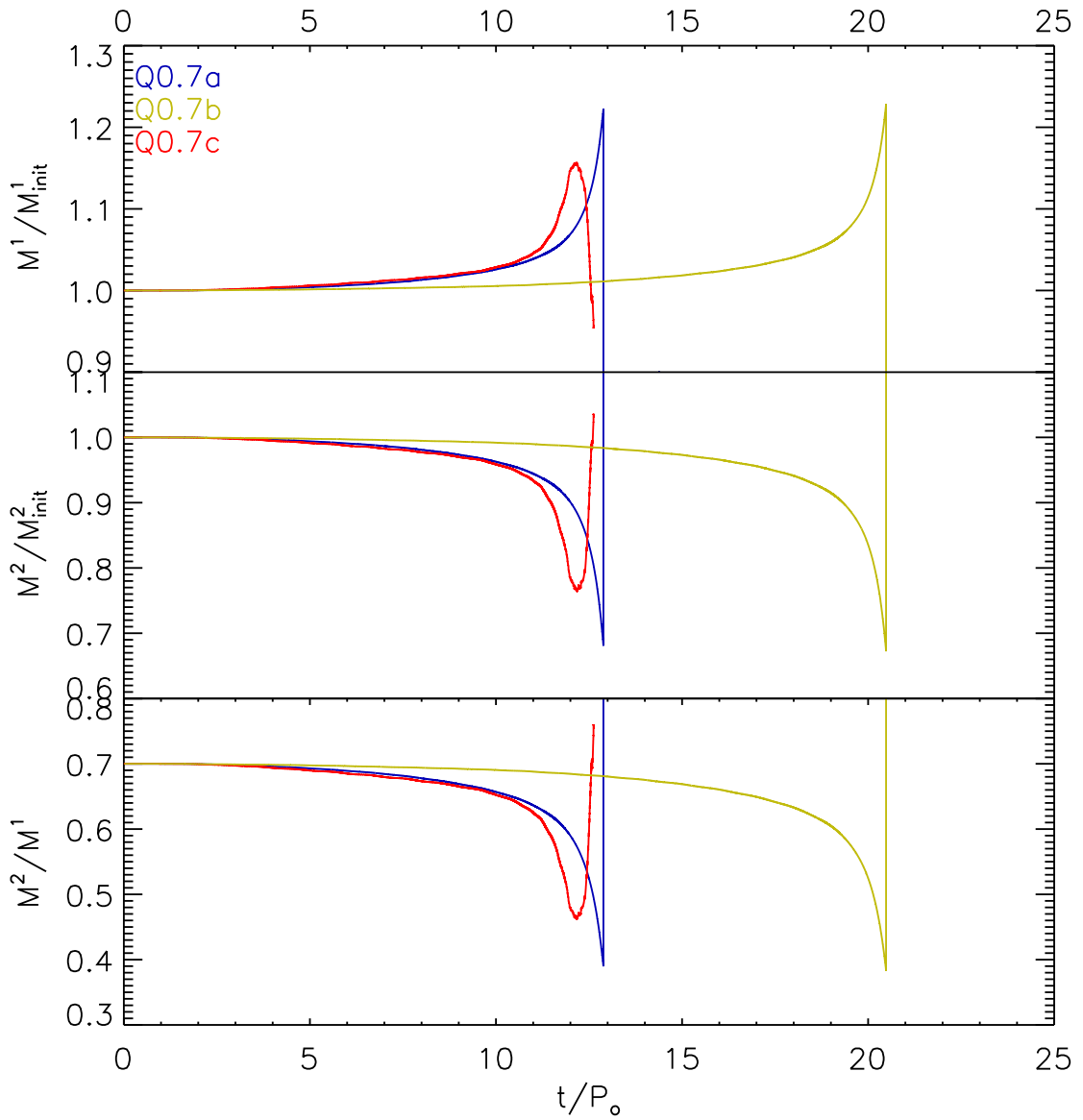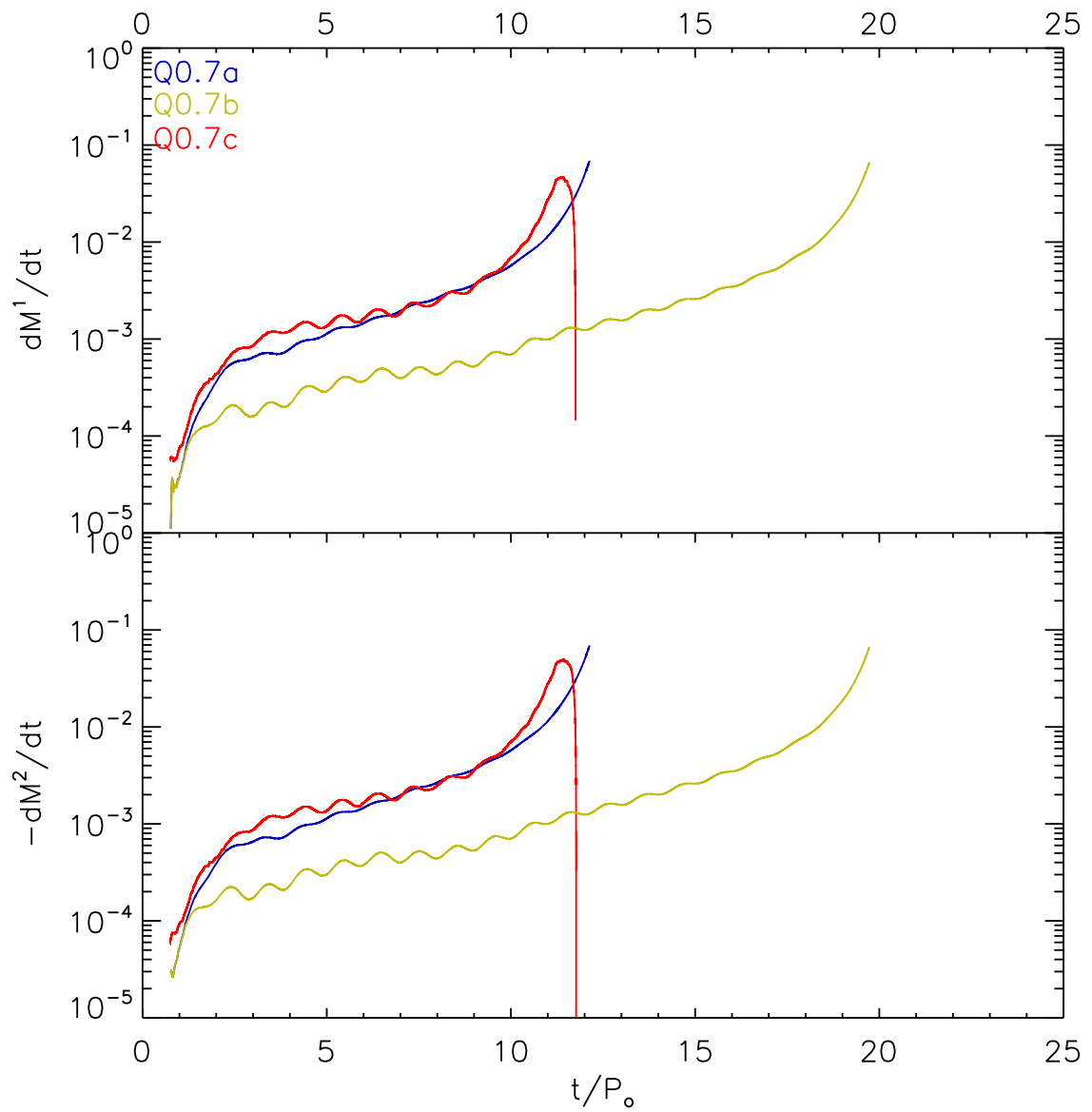
Figure 5.2 Top: The mass of the accretor vs. time for 3 different polytropic binary evolutions with an initial mass ratio of q=0.7. The mass is normalized to the initial mass and the time is displayed in orbital periods of the initial binary system. Middle: Mass of the donor normalized to the initial donor mass. Bottom: Mass ratio of the donor to accretor, q.
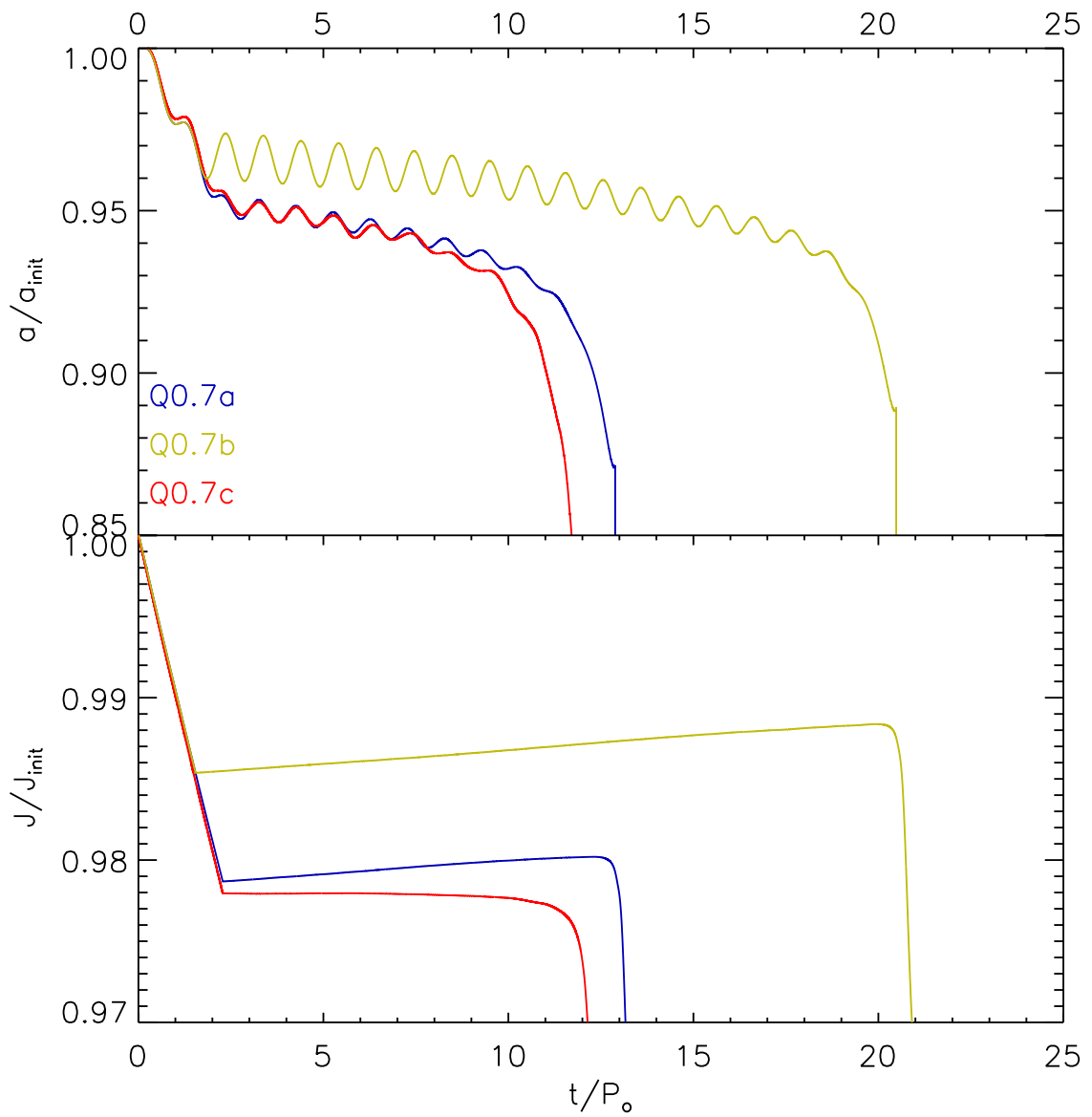
Figure 5.3 Top: The binary separation vs. time for 3 different polytropic binary evolutions with an initial mass ratio of q=0.7. The separation is normalized to the initial separation and the time is displayed in orbital periods of the initial binary system. Bottom: Total angular momentum of the binary system normalized to the initial value.
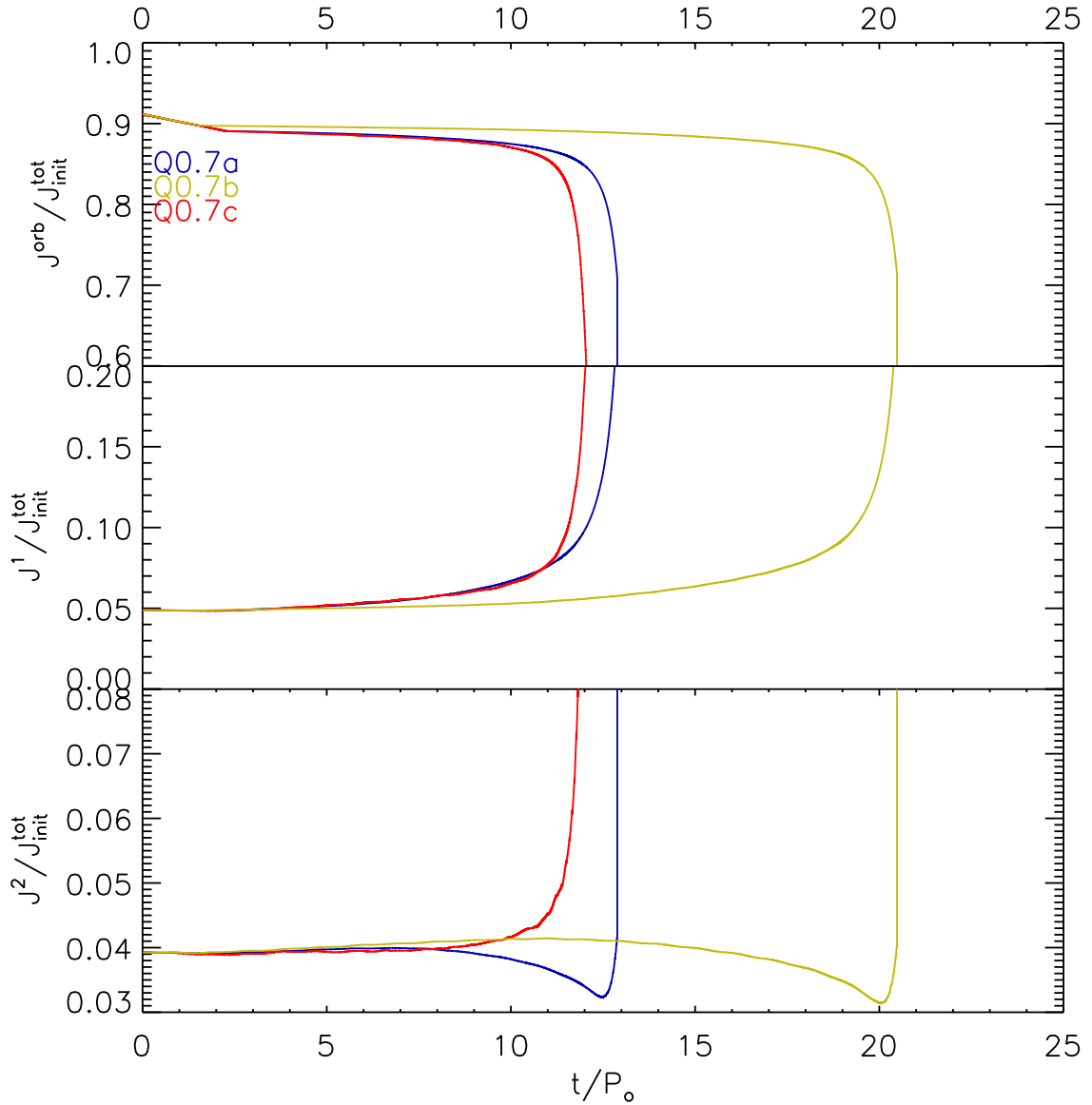
Figure 5.4 Top: The orbital angular momentum vs. time for 3 different polytropic binary evolutions with an initial mass ratio of q=0.7. The orbital momentum is normalized to the initial total momentum and the time is displayed in orbital periods of the initial binary system. Middle: The spin angular momentum of the accretor normalized to the initial total angular momentum. Bottom: Spin angular momentum of the donor normalized to the initial total angular momentum.

Figure 5.5 Top: The time rate of change of the mass of the accretor for 3 different polytropic binary evolutions with an initial mass ratio of q=0.7. The mass transfer rate is displayed in units of total mass of the binary per orbital period and time is displayed in initial orbital periods. Bottom: The time rate of change of the mass of donor.

degeneracy pressure and therefore pressure is only a function of density and has no temperature dependence. This simulation corresponds closely to the purely polytropic evolutions Q0.7a and Q0.7b described in §5.2. This model leaves out a substantial amount of physics that could have a large impact on the structure of the final merged object, but it provides a good starting point to examine the dynamics of the mass transfer and compare with the polytropic results.

Figure 5.6 shows the density in the equatorial plane at 6 different points in time during the Q2/3a evolution. The evolution was initially driven at 1% for 2.25 orbits and then continued with no driving. During the first 8 orbits the system slowly develops a mass transfer stream. The stream slowly increases in density and thickness and during this period. The structure of the donor and accretor change very little, with the exception of a small mound forming on the accretor where the stream is impacting. Around 10 orbits the donor begins to develop noticeable distortions on its surface. As shown in the upper right-hand panel of Figure 5.6, for example, the accretor has devoloped a clear triangle distortion. The blue curve in Figures 5.12 to 5.16 plot global scalar quantities as a function of time for evolution Q2/3a. In Figure 5.16 it is seen that, during the time when the surface distortions appear on the donor, the mass transfer rate begins to level off, suggesting that these surface waves feed back into the binary system and affect the eventual outcome. Around 15 orbits, the mass transfer begins to increase again and by 18 orbits the donor tidally disrupts. This final state is qualitatively very similar to evolutions Q0.7a and Q0.7b. When the donor tidally disrupts at 18 orbits, the donor material forms a thick disk around the accretor with the accretor surviving without any drastic changes to its structure.

The blue curve in the top panel of Figure 5.15 shows that during the merger the central density of the accretor increases by 40%. The bottom panel of Figure 5.15 shows the mass of an isolated white dwarf with a central density equal to the value in the upper panel. The change in central density during the merger would have corresponded to approximately a

6% increase in mass of an isolated white dwarf. However the mass in the core/disk system is significantly higher than the initial 0.9 $M_\odot$ present in the accretor. This additional mass has only a small effect on the central density and the core because it is largely rotationally supported. After the merger, the system is evolved through several more orbital periods until the disk settles into a structure that is approximately symmetric in the azimuthal direction. In Figure 5.7 the azimuthally averaged density in the equatorial plane is plotted as a function of radial distance from the center. Figure 5.8 shows the same azimuthally averaged density as Figure 5.7, but displayed as a meridional (ϖ, z) plane contour plot to examine the vertical structure of the system. A distinct high density core with a value that declines rapidly with radial distance out to a r $\approx 5 \times 10^8$ can be seen along with a lower density disk in which the density tapers off more slowly. The central core remains nearly spherical with no additional vertical structure above it and the disk has a thickness approximately equal to the diameter of the core. Figure 5.9 displays the angular frequency of the azimuthally averaged material in the equatorial plane as a fraction of the Keplerian frequency. The Keplerian frequency is defined as

$$\Omega_K \equiv \sqrt{\frac{1}{\varpi}\frac{d\overline{\Phi}}{d\varpi}}, \tag{5.1}$$

where $\overline{\Phi}$ is the azimuthally averaged gravitational potential. A ratio of 1 for the frequency to the Kepler frequency would represent material that is completely rotationally supported. The lower the ratio, the greater part the gas pressure plays in maintaining the structure. In the region that corresponds to the peak in the density, the ratio of frequencies is very small dropping to almost zero at the center. This indicates that the central object is almost entirely pressure supported. In the disk region the ratio is 0.8, indicating that the rotational support of this material is preventing it from further compressing onto the core. Given enough time, various effects could remove angular momentum from the disk and cause it to

accrete onto the central core, but the time scale for this is longer than can be carried out by these computationally expensive simulations.

5.4 q = 2/3 Zero Temperature Plus Ideal Gas

In the extremely high density region in the interior of the white dwarf, the electron degeneracy pressure will dominate over the thermal pressure of the gas even at extremely high temperatures, allowing the zero temperature approximation to be a useful tool for many systems. However, the thermal pressure will begin to dominate in the low density and high temperature regions on the surface of the stars and in the void between them. The accretion stream is a low density feature that greatly affects the eventual outcome of the binary system and adding the thermal pressure is a crucial step in obtaining more physically realistic results for the DWD mass transferring systems. Here, the initial system from §5.3 is run again with the same driving, but using the modified equation of state to include heating through shocks, as described in §4.2. This evolution will be referred to as Q2/3b.

Figures 5.10 and 5.11 show the density (left) and temperature (right) distributions in the equatorial plane at 6 times throughout the Q2/3b evolution. In the top panel of Figure 5.10 it should be noted that the temperature everywhere is initially zero because the simulation is started from a zero temperature approximation from the SCF calculation. Comparing the density contours in Figures 5.10 and 5.11 with the ones presented in Figure 5.6, the most obvious visual difference is the presence of a low density common envelope when heating is added (evolution Q2/3b) that is completely absent in the zero temperature case (evolution Q2/3a). In the left-middle frame of Figure 5.10, the higher density component of the accretion stream has a density and thickness very similar to the accretion stream in the second panel of Figure 5.6. However, an envelope of material several times thicker than the stream with a density 1-100 g/cm^3 surrounds the stream. This 1-100 g/cm^3 feature isn't present in Figure 5.6 as the density drops from 10^3 g/cm^3 to below 1 g/cm^3 within a couple of grid

cells. In addition, the well-defined surface waves seen in the zero temperature case are absent when the ideal gas component is added. In the third panel of Figure 5.6, a clear triangular structure is seen in the accretor at 12.5 orbits and this additional structure is destroyed by 16.6 orbits when the donor begins to tidally disrupt as seen in the fourth frame. In the middle and bottom rows of Figure 5.10 there is no indication of additional structure on the donor, and even the bulge that formed where the accretion stream impacted the donor that is seen in Figure 5.6 is absent. However, the higher density structure in the two simulations is qualitatively similar in the two cases. The density contours in Figure 5.11 and the last 3 frames of Figure 5.6 show that the disruption of the donor is qualitatively very similar in the two simulations.

The temperature of the core of the accretor and the entire donor remain at or below 10^7 K throughout the entire Q2/3b simulation, even during the disruption and merger. The extremely low density gas that fills the void between the stars and the spot were the accretion stream impacts the accretor are the hottest locations. The gas heated at the base of the accretion stream eventually flows around the accretor creating a hot outer layer that is slowly diffusing further into the core of the donor. This increase in temperature provides additional pressure support for the accretor and, despite matter being added, as the gold curves in Figure 5.15 show, the central density of the accretor actually decreases by 10% during the phase of mass transfer. During the disruption of the donor, as shown in the middle and bottom rows of Figure 5.11, the donor material forms a layer of cool gas around the heated outer layers of the accretor. As the system heats up both stars expand slightly. This expansion of the outer layers of the donor causes the initial mass transfer rate to be higher than in the zero temperature model (see the gold curves in Figure 5.16). However, the mass transfer rate grows more slowly in this simulation and the binary survives four orbits longer than in the zero temperature simulation.

As with the polytropic simulations Q0.7a-Q0.7c, the integrated scalar quantities in Fig-

ures 5.12 to 5.16 look very similar with a four orbit offset. The behavior of the central density of the accretor (Figure 5.15) is the notable exception. The vertical structure is also altered significantly by the addition of the heating. Figure 5.17 shows the same azimuthally averaged density of the final core/disk structure as displayed in Figure 5.8 for the zero temperature simulation. The addition of the heating created a high density envelope around the entire system. This envelope doubles the vertical extent of the structure around the core and the inner parts of the disk. Figures 5.18, 5.19, and 5.20 show the azimuthally averaged Ω/Ω_k, density, and temperature on a path leading from the center of the core along the vertical (blue) and radial (red) directions. These figures can be compared with Figure 5 in Yoon et al. (2007). Plots of the average temperature have very similar peak temperatures of $10^{8.5}$K at a distance of 5×10^8 cm. This agreement is somewhat surprising because Yoon et al. (2007) implements a nuclear reaction network in their hydrocode to provide additional energy. The density structure also matches that seen by Yoon et al. (2007). This agreement indicates that the final outcome of DWD systems is not strongly influenced by nuclear energy generated during the merger. Additionally, if a DWD binary system results in a merger or tidal disruption the final stages of the merger are similar for systems with equal masses and mass ratios even if the initial conditions vary for the simulation. This indicates that simulations of the mergers can be generally applied to DWD systems since the results do not vary widely with small changes in the system parameters or with additional physics.

Looking at the maximum temperature reached at different density levels can give insight into the potential importance of nuclear reactions since they are highly dependent on both temperature and density. Figure 5.21 shows the maximum temperature at various times for five different density contours. While the peak temperature throughout most of the simulation is over 10^9K, this only occurs in the lowest density contours and this would limit Carbon-Oxygen (CO) nuclear burning. By comparison, the maximum temperature at 10^7g/cm^3 is over two orders of magnitude lower throughout most of the simulation. To

further estimate the importance that nuclear reactions might play in the simulation, simple nuclear reaction rates can be calculated post simulation. These post-calculated rates could be significantly different than results if the rates where implemented during the hydrodynamic evolution. If the rates were implemented in the hydrocode, the additional energy would add thermal energy to the gas which could further increase the reaction rates, but could also cause the gas to expand and cool. Additionally, by adding the rates as a post process there is no way to account for the transformation of elements during the reactions. With these caveats, this approximation gives a good estimate to the amount of additional energy that could be generated by nuclear reactions during a DWD merger.

Padmanabhan (2000) provides several reaction rates for burning of elements up to C and O. The following reactions from Padmanabhan (2000) were implemented.

$$\epsilon_{pp} = \frac{2.4 \times 10^4 \rho X_H^2}{T_9^{2/3}} e^{-3.380/T_9^{1/3}} \text{ erg g}^{-1} \text{ s}^{-1}, \tag{5.2}$$

where X_H is the mass fraction of hydrogen in the gas and T_9 is the temperature in billions of degrees Kelvin.

$$\epsilon_{CNO} = \frac{4.4 \times 10^{25} \rho X_H X_m}{T_9^{2/3}} e^{-15.228/T_9^{1/3}} \text{ erg g}^{-1} \text{ s}^{-1}, \tag{5.3}$$

where, X_{He} is the mass fraction of Helium and X_m is the mass fraction of elements heavier than helium.

$$\epsilon_{3\alpha} = \frac{5.1 \times 10^8 \rho^2 X_{He}^3}{T_9^3} e^{-4.4027/T_9} \text{ erg g}^{-1} \text{ s}^{-1} \tag{5.4}$$

$$\epsilon_{\alpha^{12}C} = \frac{1.5 \times 10^{25} \rho X_{He} X_{^{12}C}}{T_9^2} e^{-32.12T_9^{-1/3}-(0.286T_9)^2} \text{ erg g}^{-1} \text{ s}^{-1} \tag{5.5}$$

$$\epsilon_{\alpha^{16}O} = \frac{6.69 \times 10^{26} \rho X_{He} X_{^{16}O}}{T_9^{2/3}} e^{-39.757T_9^{-1/3}-(0.631T_9)^2} \text{ erg g}^{-1} \text{ s}^{-1} \tag{5.6}$$

$$\epsilon_{^{12}C^{12}C} = \frac{1.43 \times 10^{42}Q\eta\rho X_{^{12}C}^2}{T_9^{3/2}}e^{-84.165/T_9^{1/3}} \text{ erg g}^{-1}\text{ s}^{-1} \tag{5.7}$$

where, Q is the energy released during the reaction channel and η is the probability of the channel being taken.

$$^{12}C + ^{12}C \rightarrow {}^{20}Ne + \alpha \quad (\text{Q} = 4.616\text{MeV}, \eta = 0.44)$$
$$\rightarrow {}^{23}Na + p \quad (\text{Q} = 2.238\text{MeV}, \eta = 0.56) \tag{5.8}$$

$$^{16}O + ^{16}O \rightarrow {}^{31}P + p \quad (\text{Q} = 7.677\text{MeV}, \eta = 0.61)$$
$$\rightarrow {}^{31}S + n \quad (\text{Q} = 1.453\text{MeV}, \eta = 0.18)$$
$$\rightarrow {}^{28}Si + \alpha \quad (\text{Q} = 9.593\text{MeV}, \eta = 0.21) \tag{5.9}$$
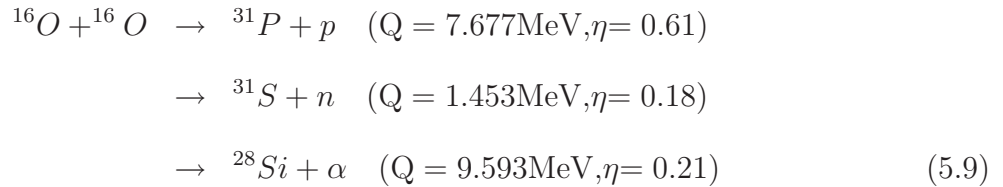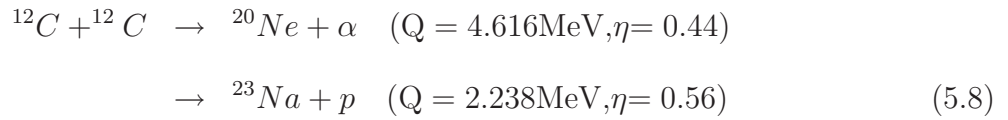
$$\epsilon_{^{16}O^{16}O} = \frac{1.3 \times 10^{52}Q\eta\rho X_{^{16}O}^2}{T_9^{2/3}}e^{\left(-135.93T_9^{-1/3}-0.629T_9^{2/3}-0.445T_9^{4/3}+0.0103T_9^2\right)} \text{ erg g}^{-1}\text{ s}^{-1} \tag{5.10}$$

The rate of energy generation depends greatly on the composition of the material in the star. Three different compositions are examined: an equal mixture of C and O, an equal mixture of C and O with $X_{He} = 10^{-4}$, and an equal mixture of C and O with a $X_{He} = 10^{-4}$ and a $X_H = 10^{-8}$. Figure 5.22 shows (across the top of the figure) the density, temperature, thermal energy density, and (across the bottom) the 3 nuclear energy generation rates during the mass transferring stage at 12.5 orbits into the simulation. In the case with only CO the nuclear energy generation rate is completely negligible compared to the amount of thermal energy that has been generated through shocks. Adding the 10^{-4} fraction of He increases the rates and the hot outer layer of the accretor may have noticeable effects from the extra

energy. If there is a small amount of H present, the nuclear energy generation would be comparable to that from the shocks. Figure 5.23 plots the same quantities at 22 orbits into the simulation, which is during the merger. At this time the CO burning would create an amount of energy similar to the thermal energy from the shock, but only in a narrow region at the surface of the accretor. The width of this region and its intensity expand if He and H are added to the composition.

Despite the differences in initial conditions and included physics, the final objects for the 0.9 $M_\odot$ and 0.6 $M_\odot$ DWD mergers agree quite well with previously published results. The accretor remains a cold core surrounded by a hot rapidly rotating thick disk and a cooler outer disk.
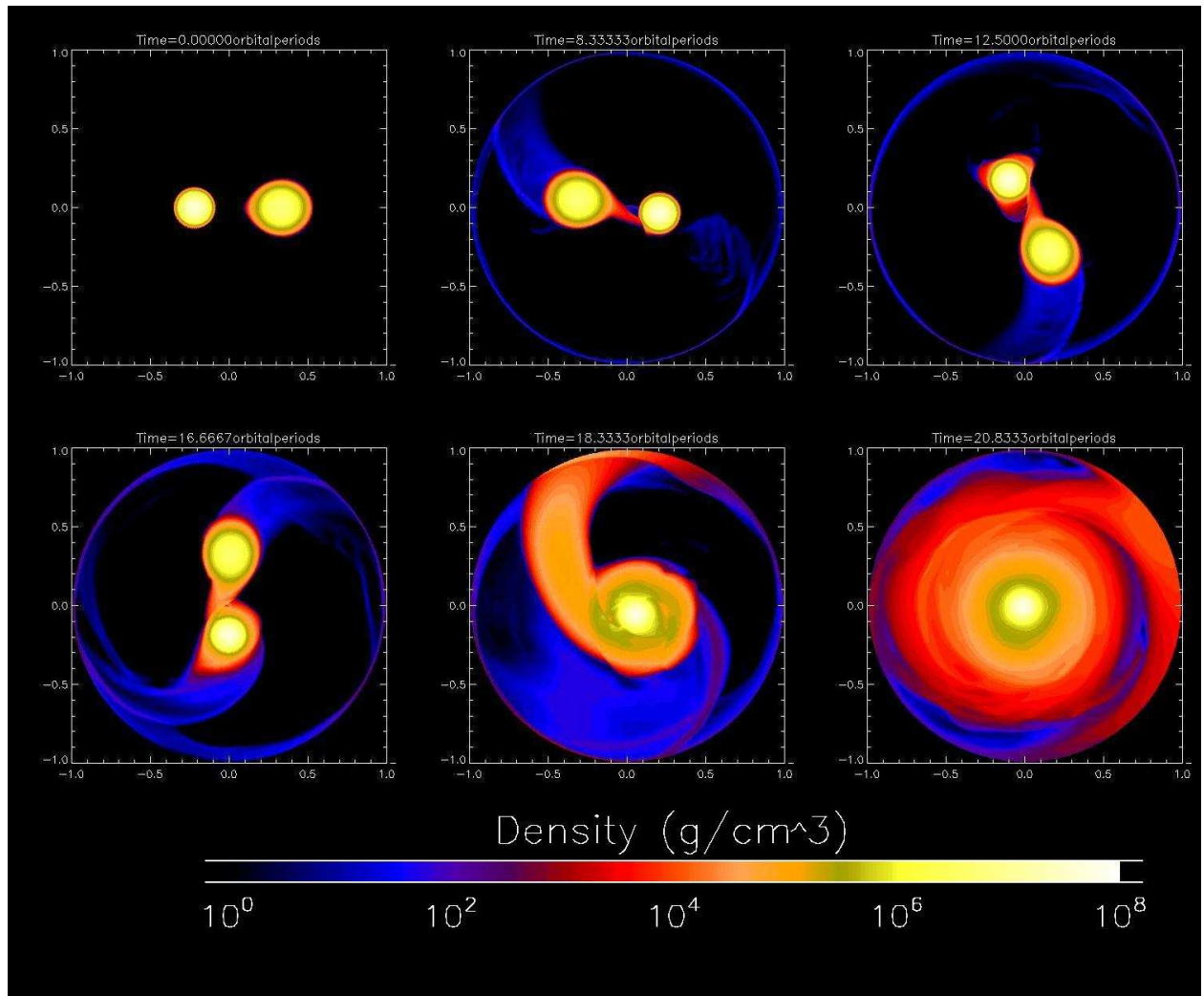
Figure 5.6 Density contours in the equatorial plane for simulation Q2/3a, a DWD binary system constructed with the ZTWD equation of state and an initial mass ratio q=2/3.
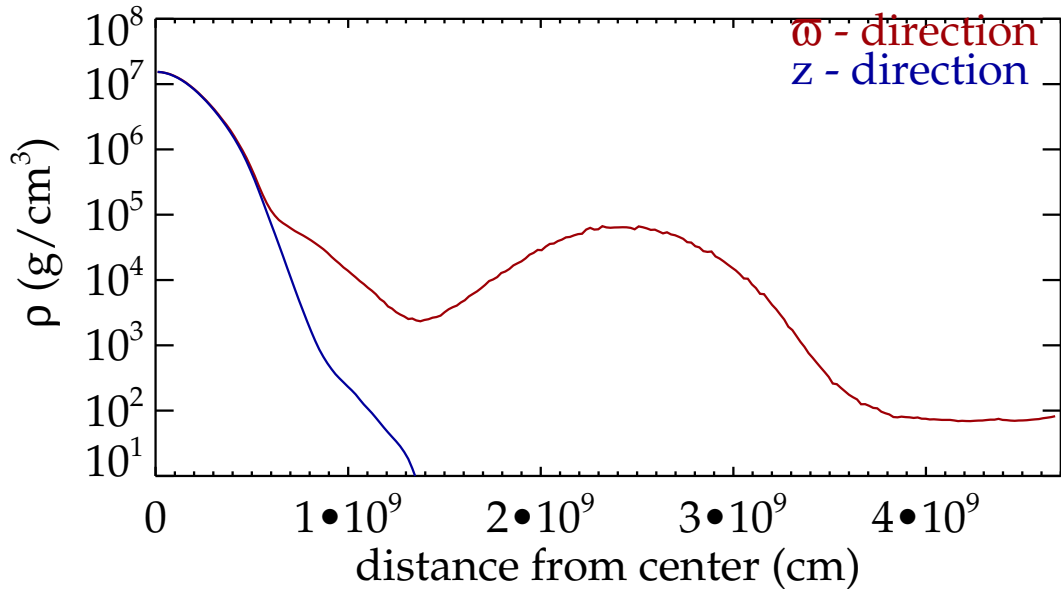
Figure 5.7 Azimuthally averaged density in the equatorial plane plotted as a function of distance from the center of the merged object at a time of 12.59 minutes (20.83 orbits) for the simulation Q2/3a, a DWD binary system constructed with the ZTWD equation of state and an initial mass ratio q=2/3.
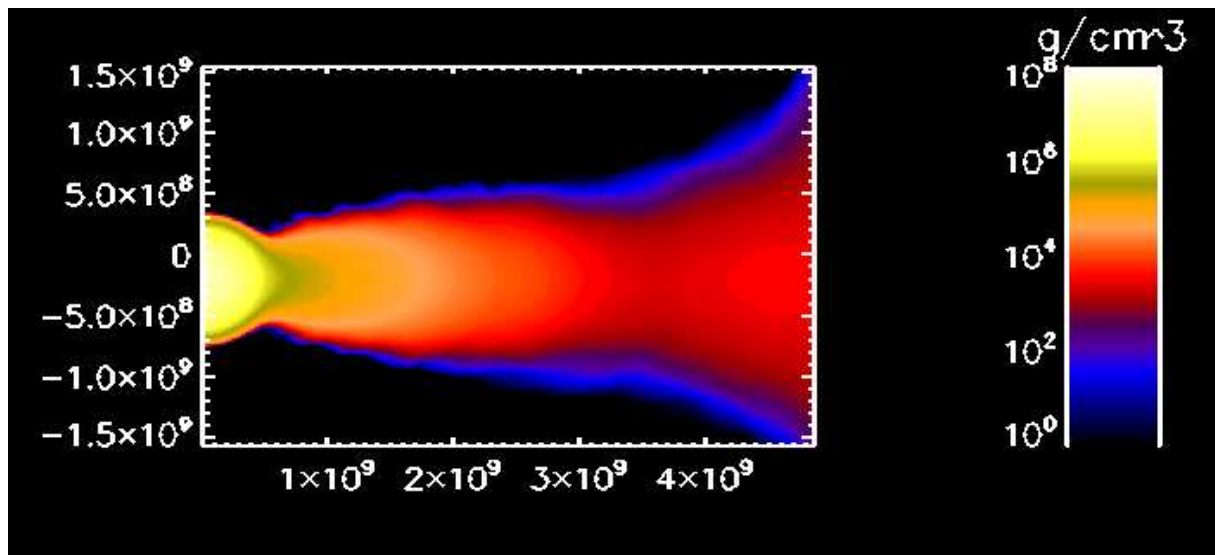
Figure 5.8 Meridional (ϖ,z) profile of the azimuthally averaged density at a time of 12.59 minutes (20.83 orbits) for simulation Q2/3a, a DWD binary system constructed with the ZTWD equation of state and an initial mass ratio q=2/3.
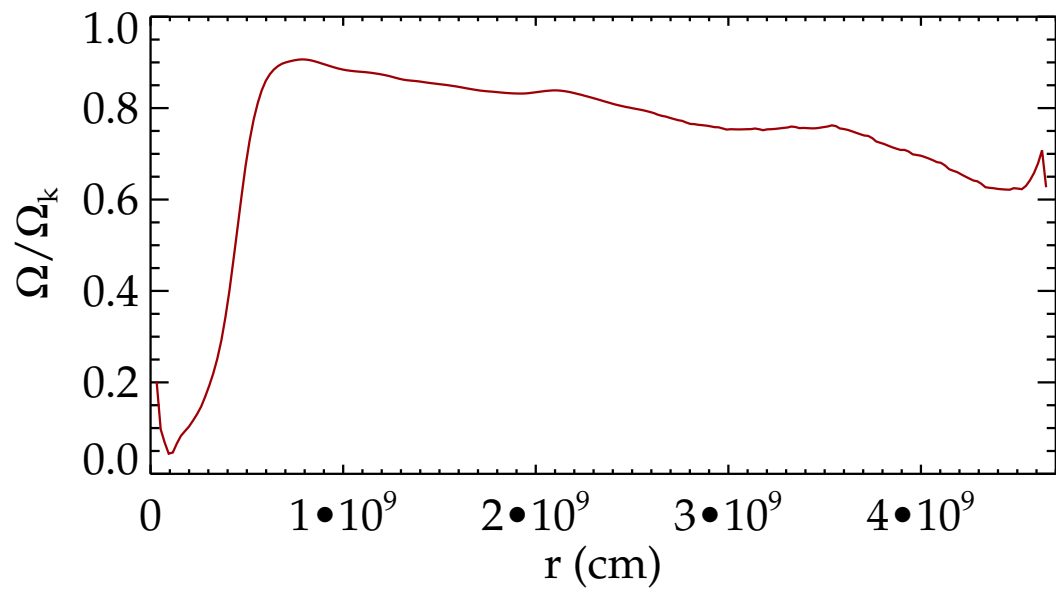
Figure 5.9 Angular velocity in the equatorial plane as a fraction of the Keplerian angular velocity at a time of 12.59 minutes (20.83 orbits) for simulation Q2/3a, a DWD binary system constructed with the ZTWD equation of state and an initial mass ratio q=2/3. A lower ratio of Ω/Ω_K indicates that the system is mainly supported by gas pressure and not rotation. A ratio of 1 indicates total rotational support.
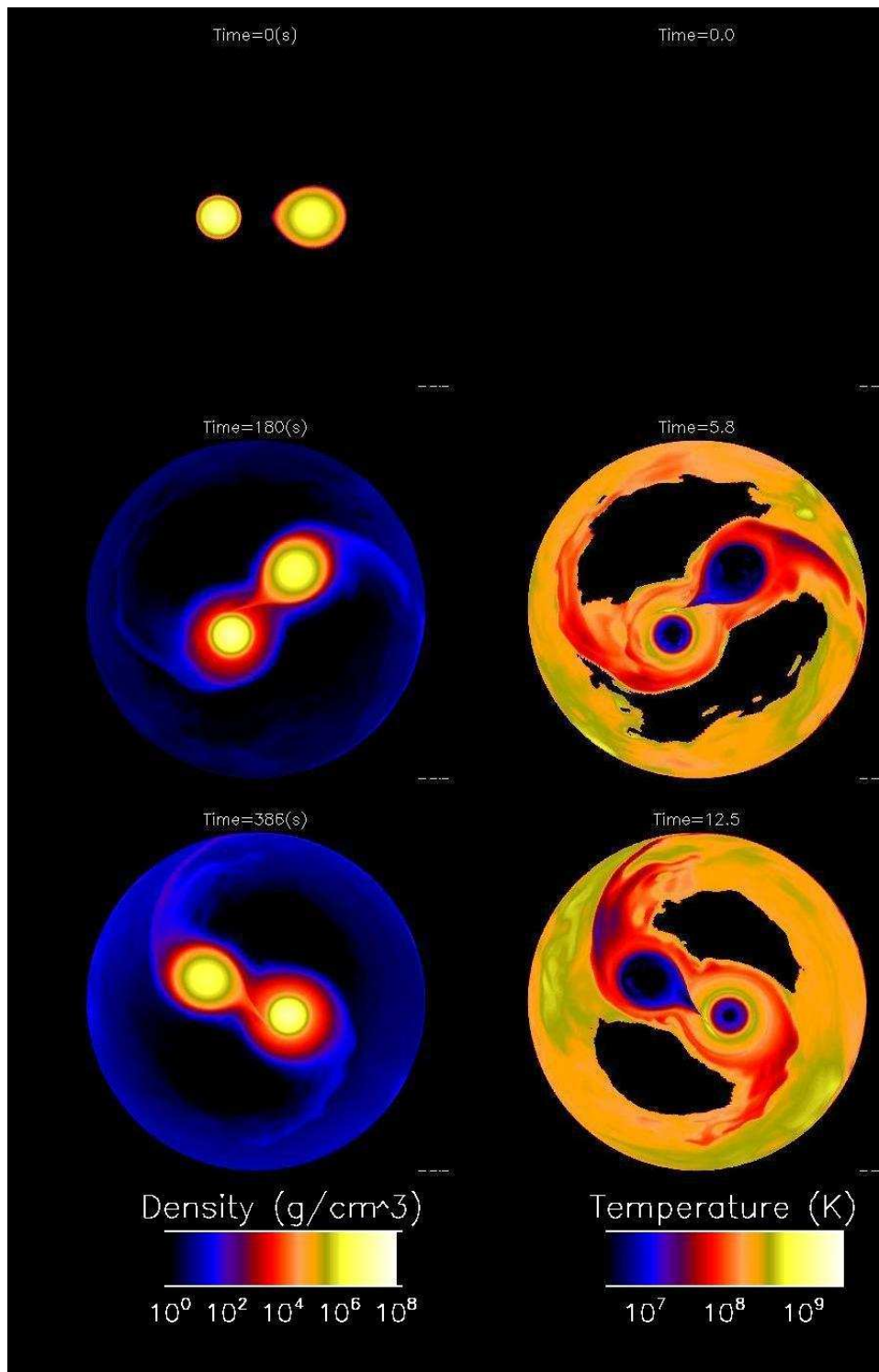
Figure 5.10 Left: Density contours in the equatorial plane for the Q2/3b simulation of a q=2/3 DWD binary with a ZTWD plus ideal gas equation of state at three different times. Right: Temperature contours in the equatorial plane for the same Q2/3b simulation.
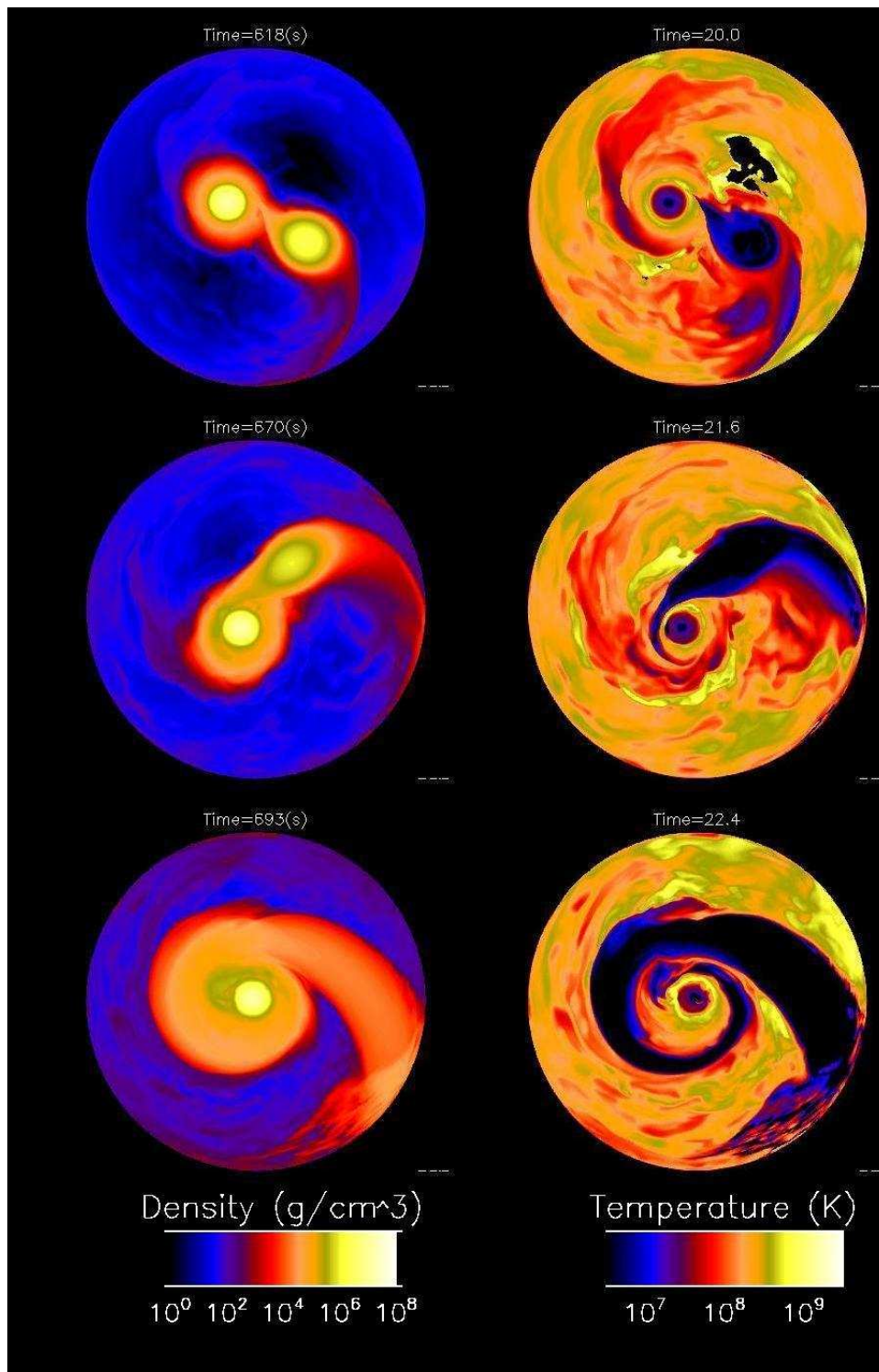
Figure 5.11 A continuation of Figure 5.10 Left: density contours in the equatorial plane for the Q2/3b simulation at three different times. Left: Temperature contours in the equatorial plane for the same Q2/3b simulation.
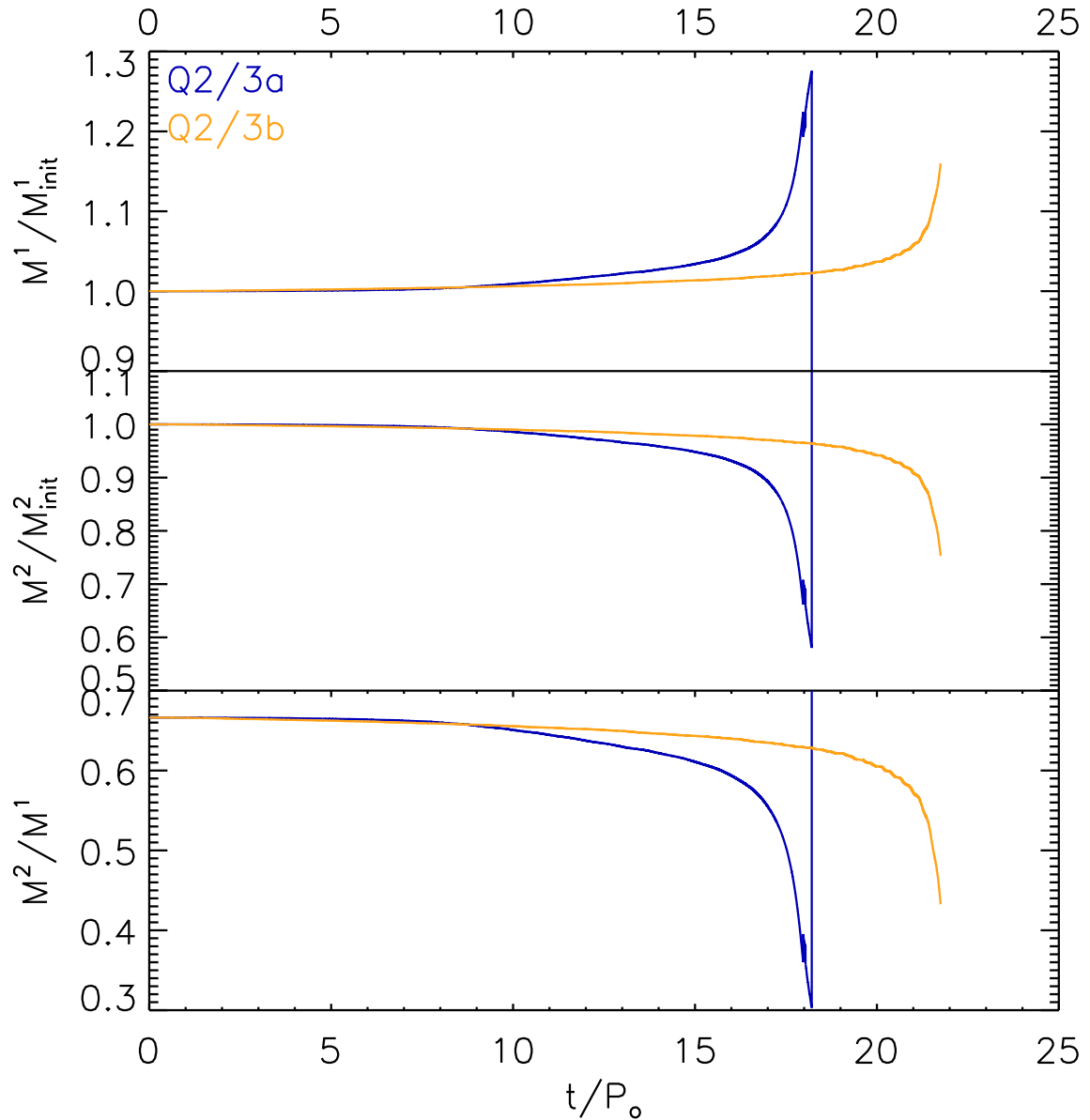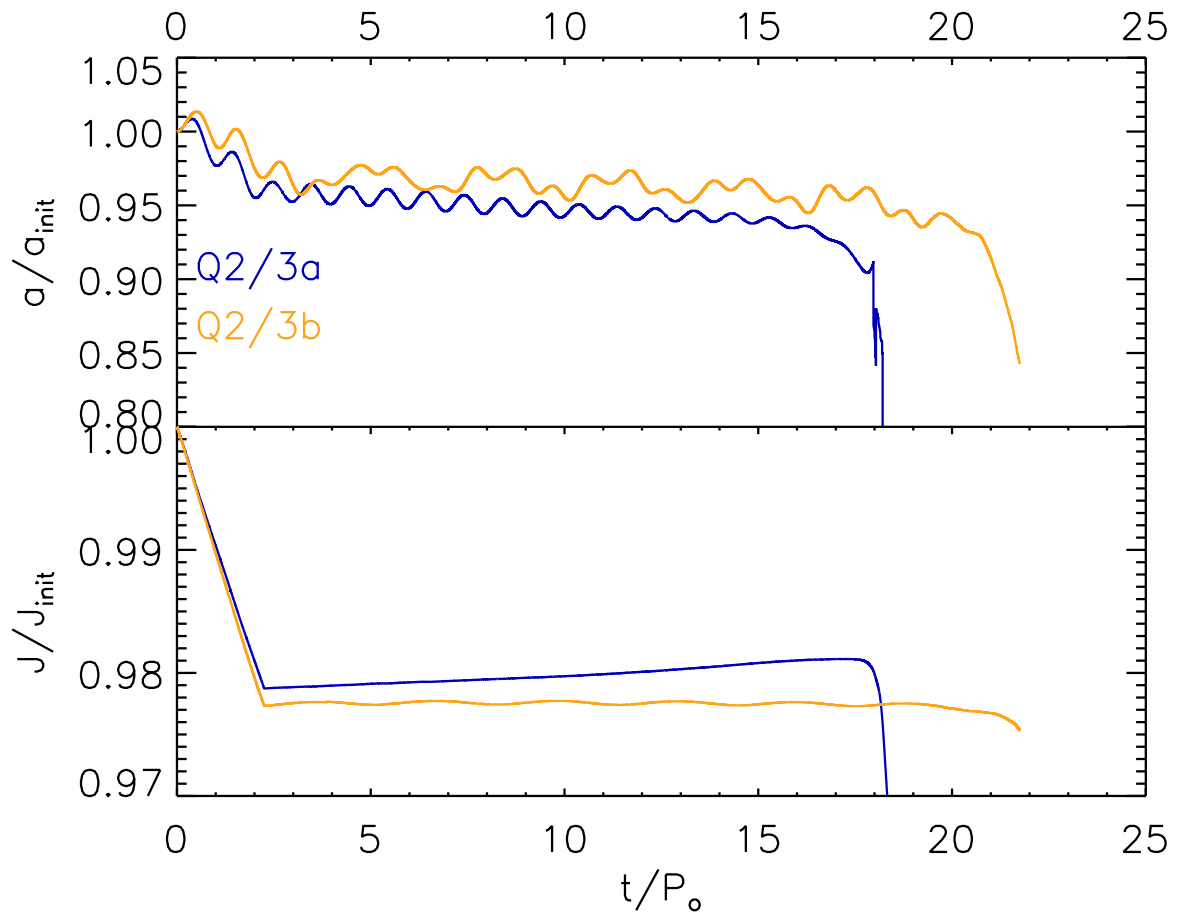
Figure 5.12 Top: The mass of the accretor vs. time for a q=2/3 DWD binary with a total mass of $1.5 M_\odot$. Q2/3a has a ZTWD EOS and Q2/3b has a ZTWD plus ideal gas EOS. The mass is normalized to the initial mass and the time is displayed in orbital periods of the initial binary system. Middle: Mass of the donor normalized to the initial donor mass. Bottom: Mass ratio of the donor to accretor, q.

Figure 5.13 Top: The binary separation vs. time for a q=2/3 DWD binary with a total mass of $1.5M_\odot$. Q2/3a has a ZTWD EOS and Q2/3b has a ZTWD plus ideal gas EOS. The separation is normalized to the initial separation and the time is displayed in orbital periods of the initial binary system.
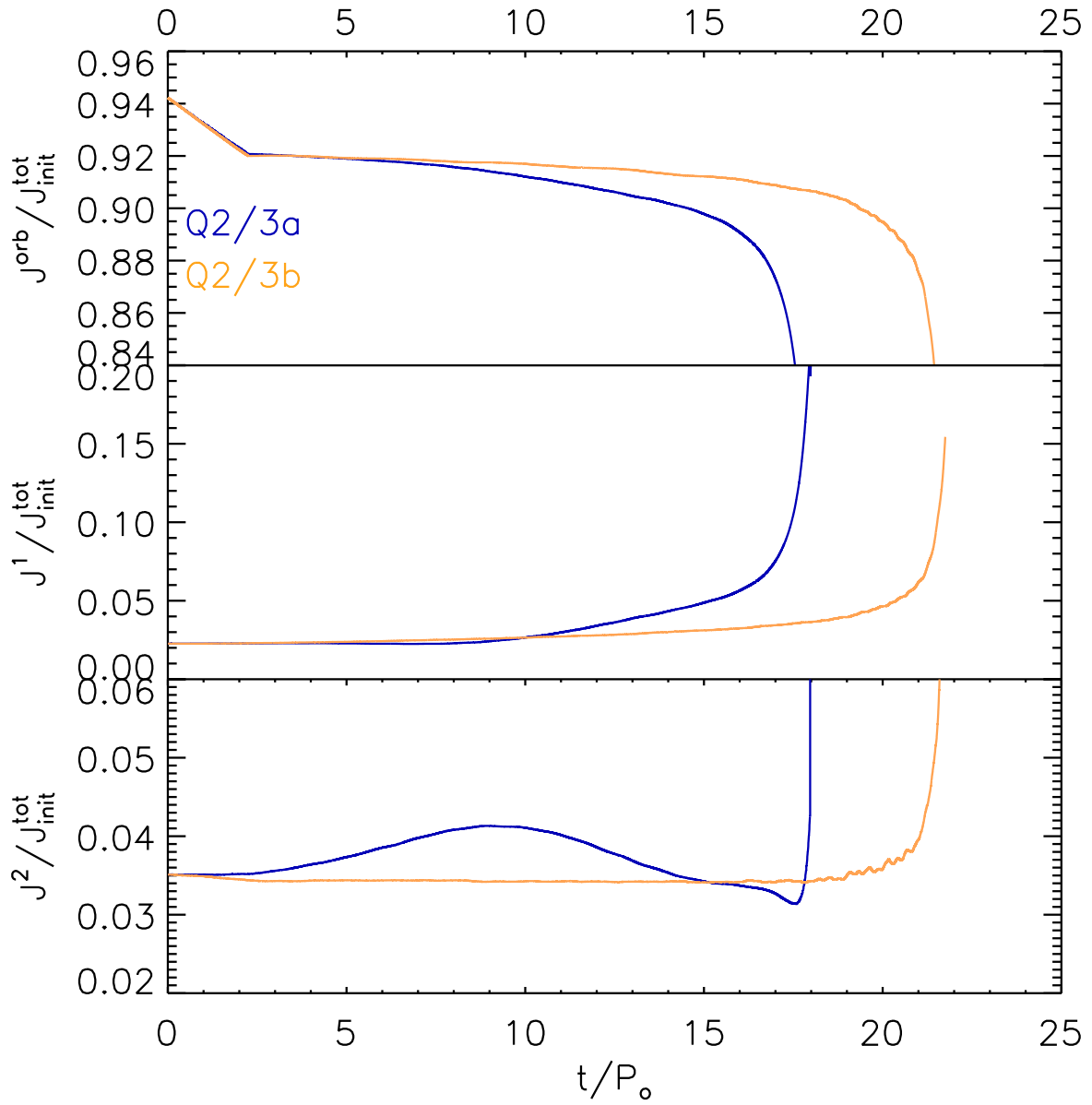
Figure 5.14 Top: The orbital angular momentum vs. time for a q=2/3 DWD binary with a total mass of $1.5M_\odot$. Q2/3a has a ZTWD EOS and Q2/3b has a ZTWD plus ideal gas EOS. The orbital momentum is normalized to the initial total momentum and the time is displayed in orbital periods of the initial binary system. Middle: The spin angular momentum of the accretor normalized to the initial total angular momentum. Bottom: Spin angular momentum of the donor normalized to the initial total angular momentum.
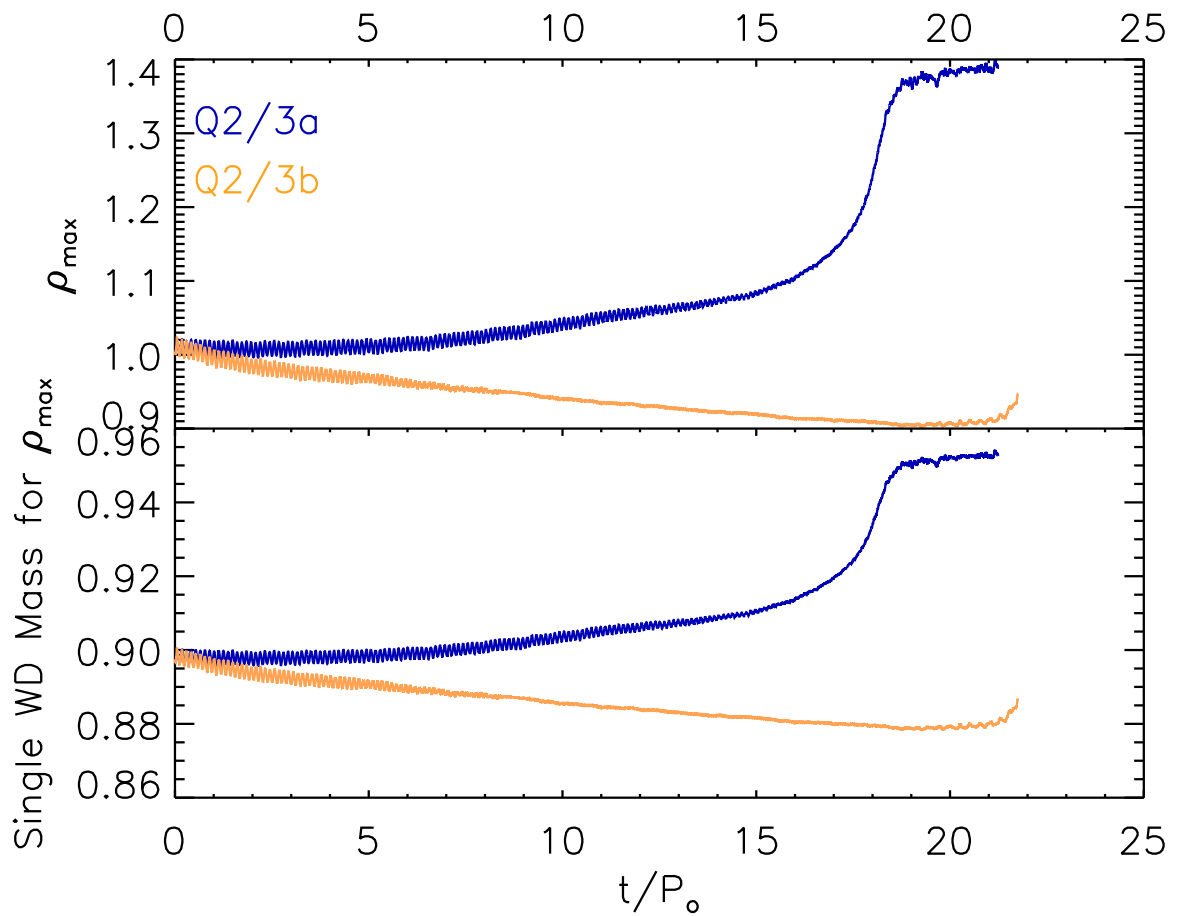
Figure 5.15 Top: The maximum density of the accretor vs. time for a q=2/3 DWD binary with a total mass of $1.5 M_\odot$. Q2/3a has a ZTWD EOS and Q2/3b has a ZTWD plus ideal gas EOS. The density is normalized to the initial maximum density of the accretor. Bottom: The mass of a non-rotating ZTWD with a central density that corresponds to the maximum central density in the top panel as a function of time in orbital periods.
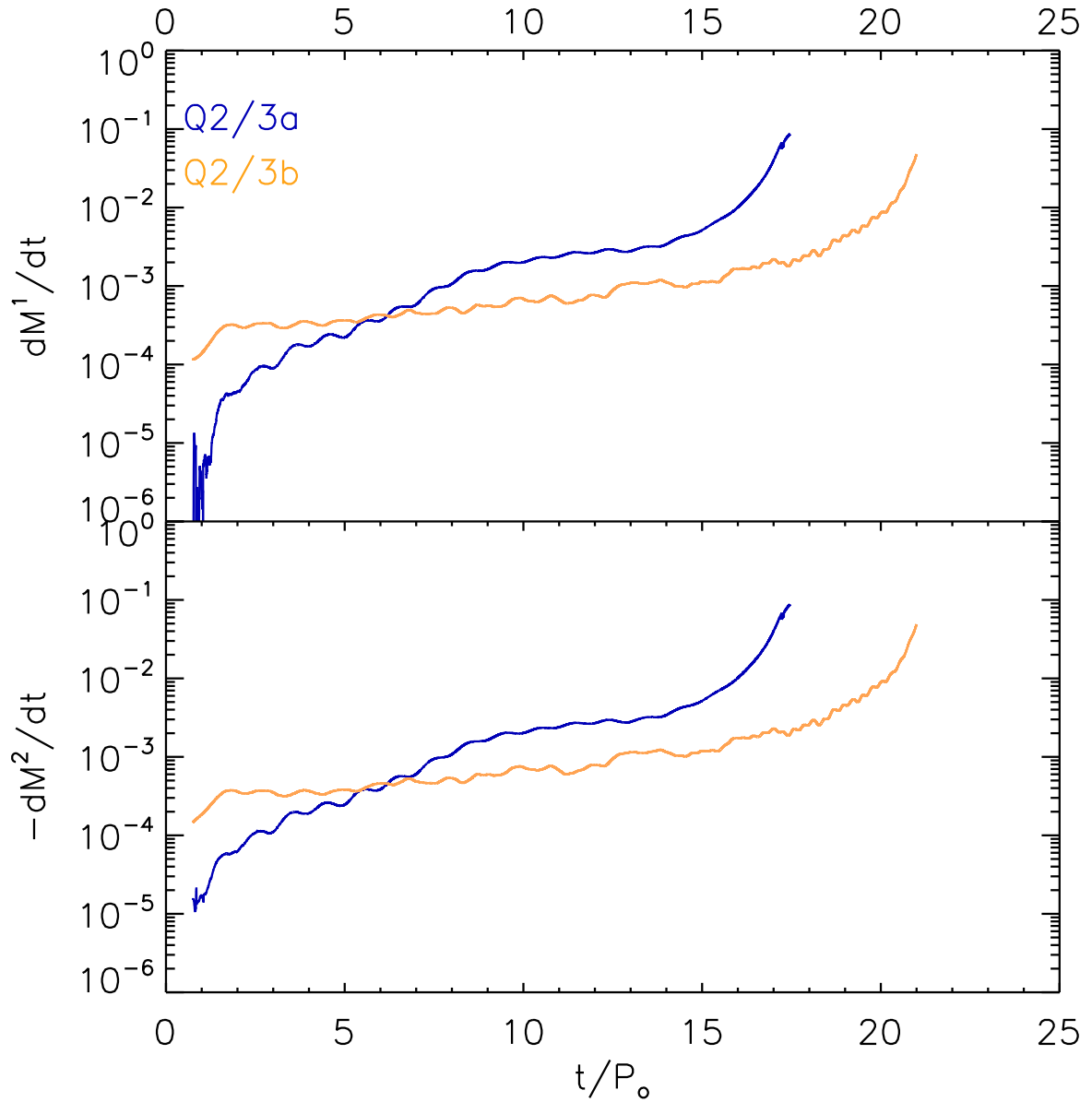
Figure 5.16 Top: The time rate of change of the mass of the accretor for a q=2/3 DWD binary with a total mass of $1.5 M_\odot$. Q2/3a has a ZTWD EOS and Q2/3b has a ZTWD plus ideal gas EOS. The mass transfer rate is displayed in units of total mass of the binary per orbital period and time is displayed in initial orbital periods. Bottom: The negative of the time rate of change of the mass of donor.
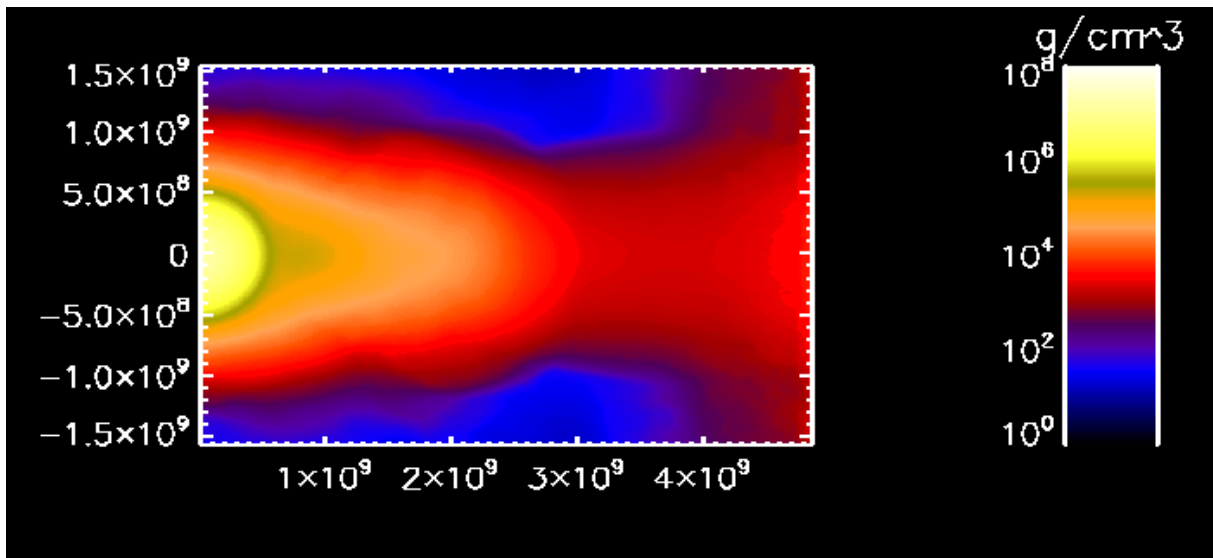
Figure 5.17 Meridional (ϖ,z) profile of the azimuthally averaged density at a time of 22.4 orbits for simulation Q2/3b, a DWD binary system constructed with the ZTWD plus ideal gas EOS and an initial mass ratio q=2/3.
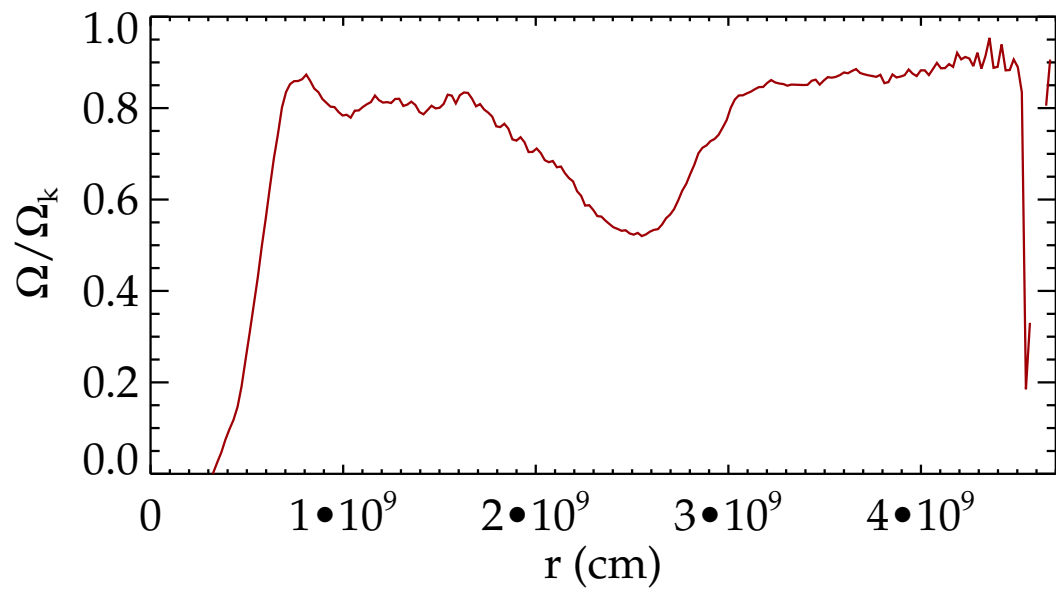
Figure 5.18 Angular velocity in the equatorial plane as a fraction of the Keplerian angular velocity at a time of 22.4 orbits for simulation Q2/3b, a DWD binary system constructed with the ZTWD plus ideal gas equation of state and an initial mass ratio q=2/3. A lower ratio of Ω/Ω_K indicates that the system is mainly supported by gas pressure and not rotation. A ratio of 1 indicates total rotational support.
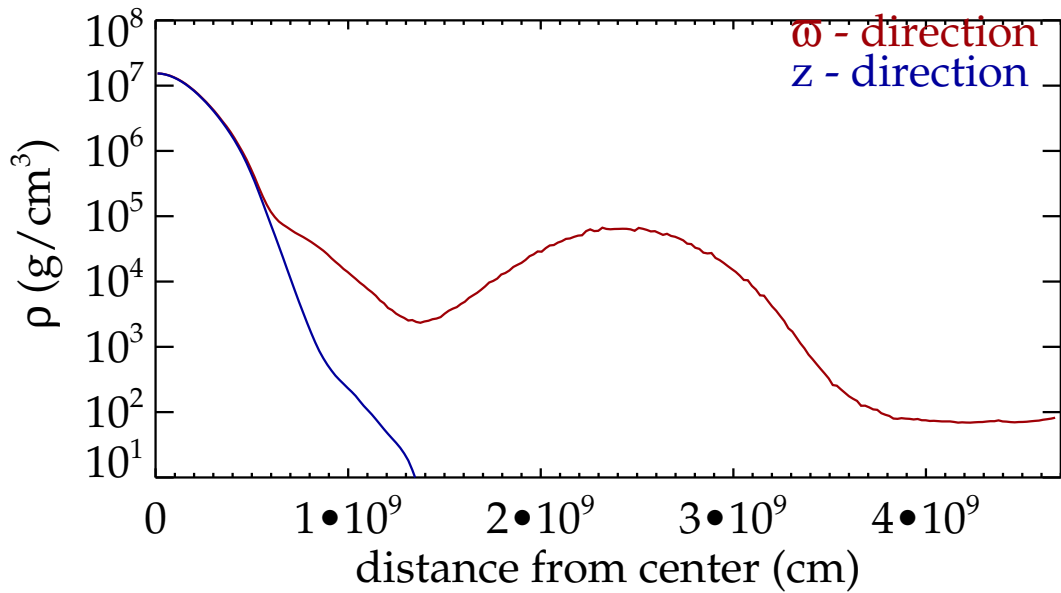
Figure 5.19 Azimuthally averaged density in the equatorial plane at a time of 22.40 orbits for simulation Q2/3b, a DWD binary system constructed with the ZTWD plus ideal gas EOS and an initial mass ratio q=2/3.
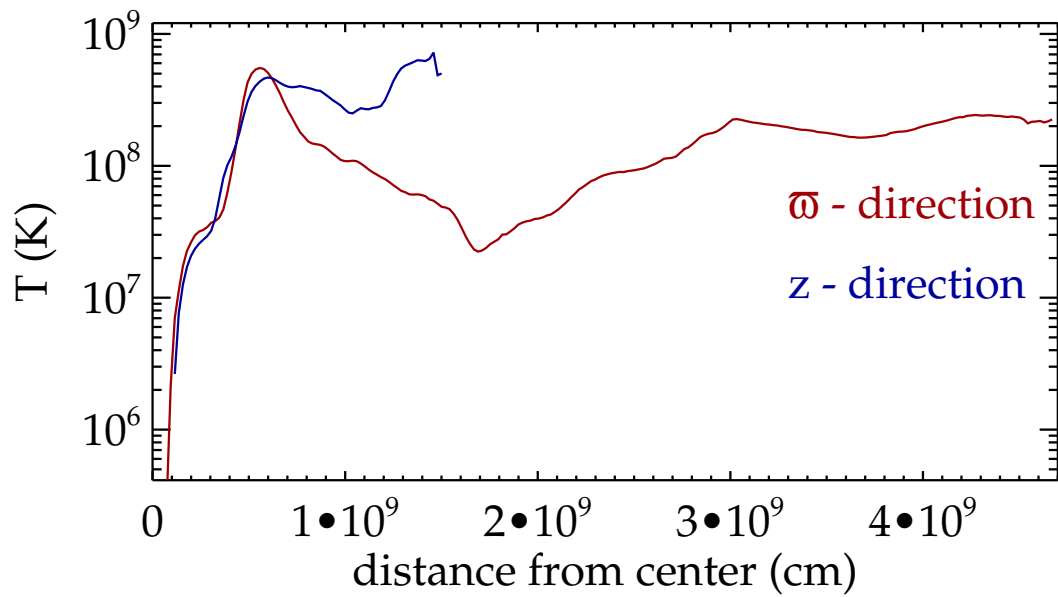
Figure 5.20 Azimuthally averaged temperature in the equatorial plane plotted as a function of distance from the center of the accretor at a time of 22.40 orbits for simulation Q2/3b, a DWD binary system constructed with the ZTWD plus ideal gas EOS and an initial mass ratio q=2/3.
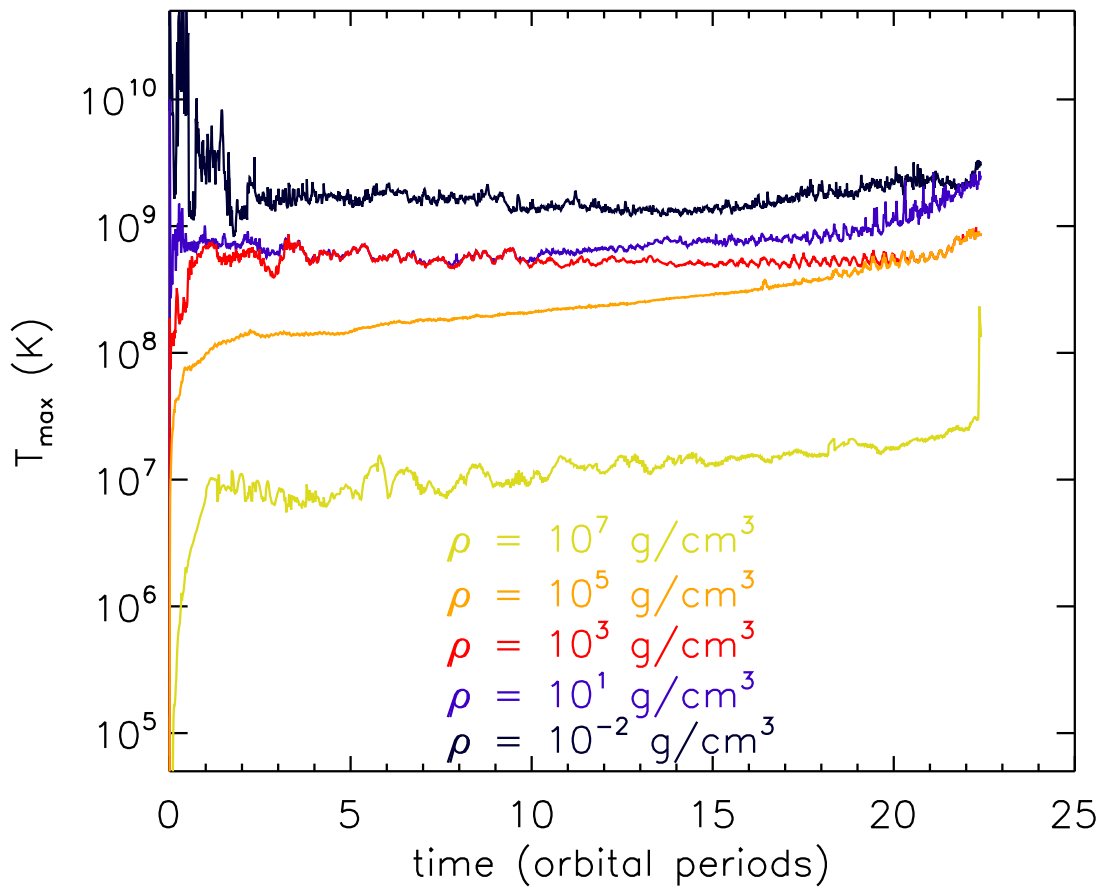
Figure 5.21 Each curve represents the maximum temperature at a give time for material with a density less than or equal to the corresponding density label in the legend. For example the red curve is the maximum value of the temperature in all cells with a density less than or equal to 10^3 g/cm^3 at the time on horizontal axis.
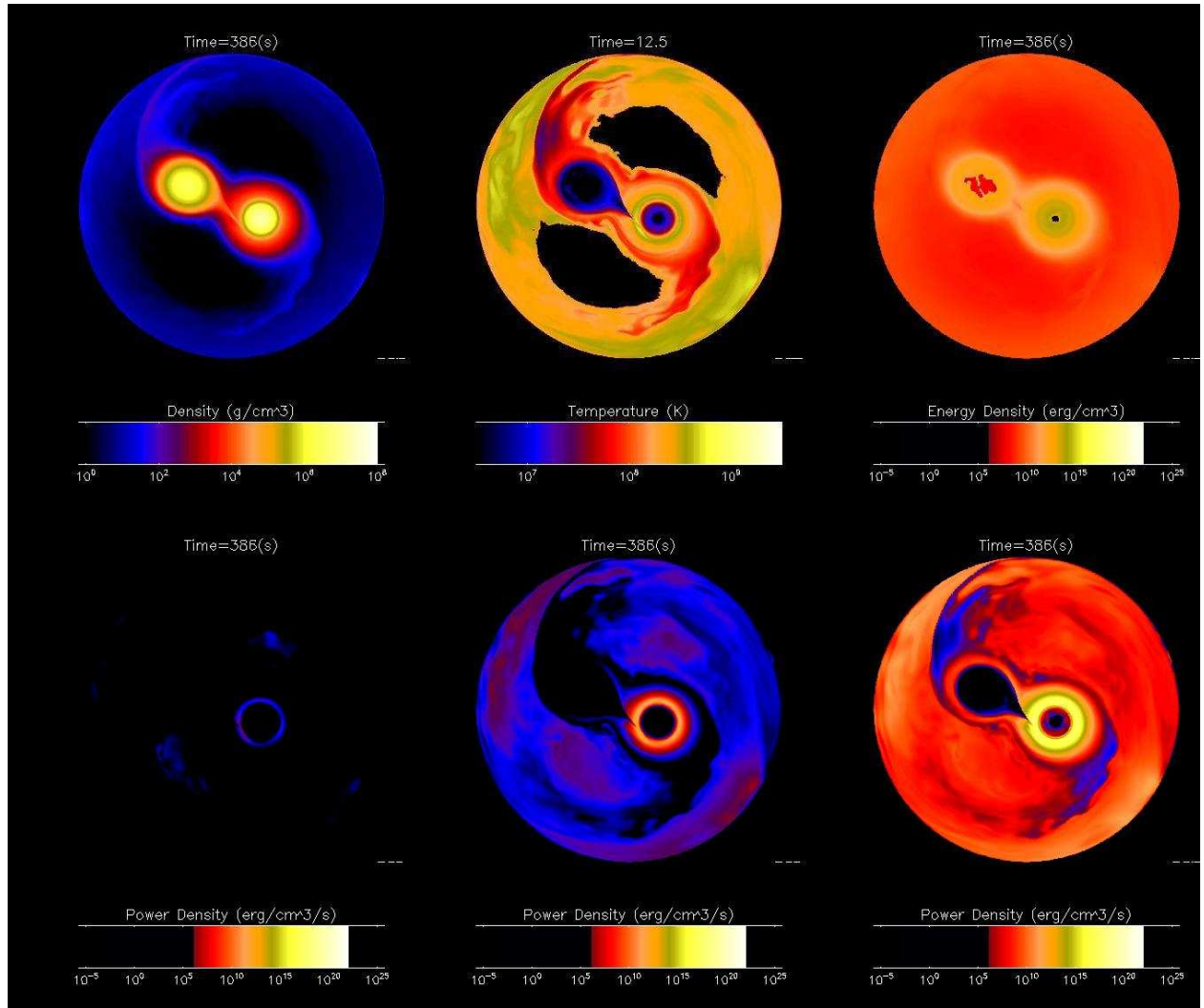
Figure 5.22 Contour plots in the equatorial plane for a q=2/3 DWD binary simulation, Q2/3b, with a total mass of $1.5M_\odot$ and a ZTWD plus ideal gas EOS at a time of 12.5 orbital periods (386s). Top Left: Mass density. Top Center: Temperature. Top Right: Energy density of the ideal gas. Bottom Left: Power density from nuclear reactions assuming the system has an equal amount of C and O and no other elements, Bottom Center: Same as the left panel except with $X_{He} = 10^{-4}$ added. Bottom Right: Same as the center panel except with $X_H = 10^{-8}$ added.

Figure 5.23 Same as Figure 5.22 except at an evolution time of 22.0 orbital periods (683s).
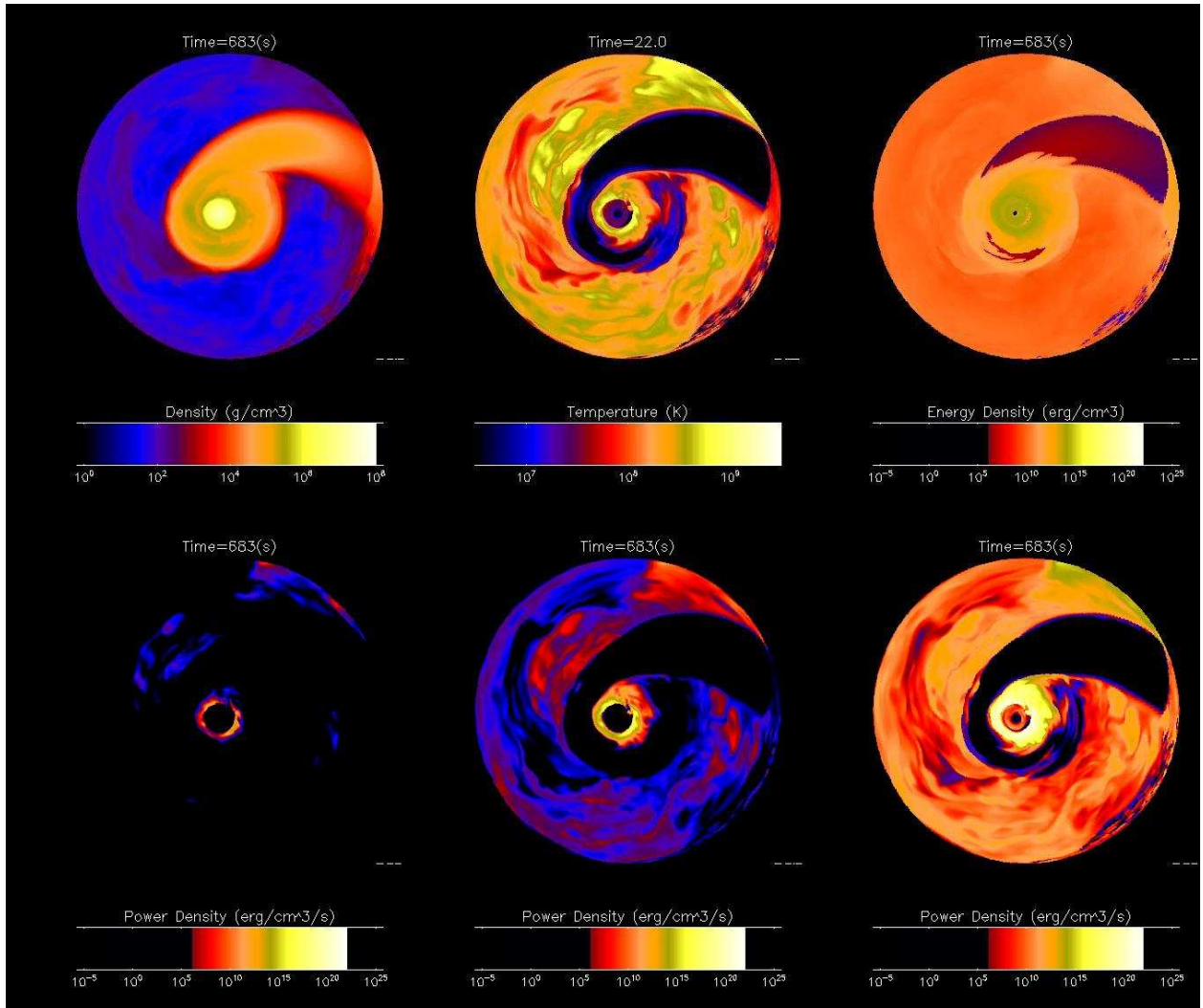
6. Conclusions

Based on the earlier work of Hachisu (1986a,b) and Hachisu, Eriguchi, & Nomoto (1986a) we have developed a self-consistent-field technique that can be used to construct equilibrium models of synchronously rotating DWD binaries having a range of total masses, mass ratios, and binary separations. In addition to effects introduced by synchronous rotation, the distorted structure of both stars in each converged model is governed by the zero-temperature white dwarf equation of state (2.1) and a self-consistently determined, Newtonian gravitational field. In an effort to illustrate the technique's capabilities, we have constructed a set of models along five sequences: Three sequences ('A', 'B', and 'C') mimic the last segment of the detached "inspiral" phase of DWD binary evolutions during which both M_{tot} and q are held constant as a decreases; and two sequences ('D' and 'E') mimic a semi-detached "conservative mass transfer" phase of evolution during which M_{tot} is held fixed and the less massive star stays in marginal contact with its Roche lobe, but q steadily decreases while a steadily increases.

Along each inspiral sequence, the functional dependence of J_{tot} and E_{tot} on the orbital separation can be well understood in terms of simple analytical expressions that describe two spinning spherical white dwarfs in circular orbit about one another. For a given total mass and separation, the calculated orbital frequencies along each inspiral sequence deviate measurably from associated Keplerian frequencies only in models for which the Roche-lobe filling factor of the less-massive star is $\gtrsim 60\%$. But, at least for the sequences examined here, the deviation from Keplerian frequencies is never more than 1% even at contact.

Along both conservative mass-transfer sequences, we have documented how a, Ω, J_{tot} and E_{tot} vary with the system mass ratio as q decreases by roughly a factor of two, from $q = 1.0$ down to $q \lesssim 0.5$. Along each sequence we have compared our numerically determined values

of a at various values of q with the analytic $a(q)$ function (3.12) that is derived by setting the radius of the less massive star, as specified by the Nauenberg (1972) mass-radius relation, equal to the Roche-lobe radius, as approximated by Eggleton (1983). Qualitatively, our results show the same $a(q)$ behavior that is predicted by this analytic expression. However, at a given q the value of a derived from our models is consistently $\sim 8\%$ larger than the value obtained from Eq. (3.12). The analytic expression could be brought into closer quantitative agreement with our numerical results if the leading coefficient in Eq. (3.12) is increased by 8%, that is, if the expression's leading coefficient is changed from 0.0229 to 0.0247. This modification will, in turn, decrease the Keplerian frequency obtained from the analytic $a(q)$ expression by $\sim 9\%$, simultaneously bringing the analytically predicted orbital frequency into much closer agreement with our numerically determined values of Ω. Along both of our conservative mass-transfer sequences, the plot of $J_{\mathrm{tot}}(q)$ displays an extremum at a value of $q \lesssim 2/3$. The location of this extremum is almost certainly identifying the value of q_{crit} that is relevant along both sequences.

We have demonstrated that both an n=3/2 polytropic binary with a mass ratio of q=0.7 and a DWD binary with a total mass of 1.5 $M_\odot$ and a mass ratio of q=2/3 are dynamically unstable after the onset of mass transfer. In both the polytropic and DWD binaries the onset of mass transfer led to the eventual tidal disruption of the donor with most of the donor material forming a disk around the accretor, which has remained mostly intact.

In the simulation with the ZTWD plus ideal gas EOS, Q2/3b, we find that mass transfer can occur for many orbits before the eventual tidal disruption. During this phase of steady mass transfer the outer layers of the accretor are heated to $\sim 10^8$K. However, this heating does not penetrate into the higher density regions of the accretor and the interior remains between $\sim 10^5$-10^7K. If a composition of pure C and O is assumed, there should not be significant energy generation from nuclear fusion during the mass transfer phase. The addition

of small amounts of He and H can increase the expected levels of nuclear fusion, but only in the hot outer layer of the accretor.

The final merged structure from the Q2/3b simulation is a cold ($< 3 \times 10^7$K) core of accretor material that is pressure supported. Around this core is a hot ($\sim 5 \times 10^8$K) envelope of material that is also primarily pressure supported. This pressure supported inner object lies at the center of a disk with a thickness slightly larger than the diameter of the core and with a radius that is approximately 6 times greater than that of the core. This disk is primarily supported by rotation and has a temperature of 10^7K-10^8K. The temperatures and densities in the hottest region are favorable for the fusion of C and O, but in a very small region and not at a rate high enough to lead to an explosive event. Therefore, for the total mass and mass ratio examined in this simulation it is unlikely that a supernova would occur during or immediately following the merger. This does not rule out DWD mergers as progenitors to Type Ia supernovae. Viscous effects within the disk will cause the disk material to accrete onto the core over a longer period of time. If the time scale for accretion of the disk is shorter than the time scale for significant cooling of the gas then density and temperatures could reach values that would result in a delayed supernova.

Bibliography

Balay, S., Buschelman, K., Eijkhout, V., Gropp, W., Kaushik, D., Knepley, M., McInnes, L., Smith, B., and Zhang, H. 2004, PETSc Users Manual, ANL-95/11 - Revision 2.1.5

Benz, W., Cameron, A. G. W., Press, W. H., & Bowers, R.L. 1990, ApJ, 348,647

Chandrasekhar, S. 1935, MNRAS, 95, 207

Chandrasekhar, S. 1967, *An Introduction to the Study of Stellar Structure*, New York: Dover

Cohl, H. and Tohline, J. 1999, ApJ, 527, 86

Cox, A. N. 2000, *Allen's Astrophysical Quantities*, 4th edition, New York: Springer-Verlag

D'Souza, M. C. R., Motl, P. M., Tohline, J. E., & Frank, J. 2006, ApJ, 643, 381

Eggleton, P. P. 1983, ApJ, 268, 368

Even, W., & Tohline, J. E. 2009, ApJS, 184, 248

Guerrero, J., Garcia-Berro, E., & Isern, J. 2004, A&A, 413, 257

Hachisu, I. 1986a, ApJS, 61, 479

Hachisu, I. 1986b, ApJS, 62, 461

Hachisu, I., Eriguchi, Y., & Nomoto, K. 1986a, ApJ, 308, 161

Hachisu, I., Eriguchi, Y., & Nomoto, K. 1986b, ApJ, 311, 214

Livio, M. 2000, in *Type Ia Supernovae: Theory and Cosmology*, ed. J. C. Niemeyer, & J. W. Truran (Cambridge Univ. Press), 33

Marsh, T. R., Nelemans, G., & Steeghs, D. 2004, MNRAS, 350, 113

Motl, M. P., 2001, Dissertation, Louisiana State University

Motl, M. P., Tohline, J. E., Frank, J., 2002, ApJS, 138, 121

Motl, M. P., Frank, J., Tohline, J. E., & D'Souza, M. C. R. 2007, ApJ, 670, 1314

Nauenberg, M. 1972, ApJ, 175, 417

Nelemans, G., Portegies Zwart, S.F., Verbunt, F., & Yungleson, L. R. 2001, A&A, 368, 939

New, C. B. Kimberly, and Tohline, Joel E. 1997, ApJ, 490, 311

Ostriker, J.P., and Mark, J W-K. 1964, ApJ, 151, 1075

Padmanabhan, T., 2000 ,Theoretical Astrophysics Volume I: Astrophysical Processes, Cambridge University Press

Ramsay, G., Brocksopp, C., Groot, P. J., Hakala, P., Lehto, H., Marsh, T. R., Napiwotzki, R., Nelemans, G., Potter, S., Slee, B., Steeghs, D., & Wu, K. 2007, ASP Conference Series, 15th *European Workshop on White Dwarfs*, 372, 425 (arXiv:astro-ph/0610357v1)

Ruciński, S. M. 1988, AJ, 95, 1895

Segretain, L., Chabrier, G., & Mochkovitch, R. 1997, ApJ, 481, 355

Verbunt, F., & Rappaport, S. 1988, ApJ, 332, 193

Yoon, S.-C., Podsiadlowski, Ph., & Rosswog, S. 2007, MNRAS, 380, 933

Zapolsky, H. S., & Salpeter, E. E. 1969, ApJ, 158, 809

Appendix A: White Dwarf Mass-Radius Relationship

A.0.1   The Chandrasekhar Mass

Chandrasekhar (1935) was the first to construct models of spherically symmetric stars using the equation of state defined by Eq. (2.1) and, in so doing, demonstrated that the maximum mass of an isolated, nonrotating white dwarf is $M_{\mathrm{ch}} = 1.44(\mu_e/2)M_\odot$, where μ_e is the number of nucleons per electron and, hence, depends on the chemical composition of the WD. A concise derivation of M_{ch} (although, at the time, it was referred to as M_3) is presented in Chapter XI of Chandrasekhar (1967), where we also find that the expressions for the two key coefficients in Eqs. (2.1) and (2.2) are,

$$A \equiv \frac{\pi m_e^4 c^5}{3h^3}, \tag{A.1}$$

$$B\mu_e^{-1} \equiv \frac{8\pi m_p}{3}\left(\frac{m_e c}{h}\right)^3. \tag{A.2}$$

Numerical values for A and $B\mu_e^{-1}$ are given here in Table B.1 along with values of the physical constants c, h, m_e, and m_p that we have used (column 2) and that Chandrasekhar (1967) used (column 3) to determine the values of A and $B\mu_e^{-1}$. The derived analytic expression for the limiting mass is,

$$\mu_e^2 M_{\mathrm{ch}} = 4\pi m_3\left(\frac{2A}{\pi G}\right)^{3/2}\frac{\mu_e^2}{B^2} = 1.14205 \times 10^{34}\ \mathrm{g}, \tag{A.3}$$

where the coefficient,

$$m_3 \equiv \left(-\xi^2\frac{d\theta_3}{d\xi}\right)_{\xi=\xi_1(\theta_3)} = 2.01824, \tag{A.4}$$

represents a structural property of $n = 3$ polytropes ($\gamma = 4/3$ gases) whose numerical value can be found in Chapter IV, Table 4 or Chandrasekhar (1967). We note as well that

Chandrasekhar (1967) identified a characteristic radius, ℓ_1, for WDs given by the expression,

$$\ell_1\mu_e \equiv \left(\frac{2A}{\pi G}\right)^{1/2}\frac{\mu_e}{B} = 7.71395 \times 10^8 \text{ cm} \,. \tag{A.5}$$

A.0.2 The "Nauenberg" Mass-Radius Relationship

Nauenberg (1972) derived an analytic approximation for the mass-radius relationship exhibited by isolated, spherical WDs that obey the ZTWD equation of state given in Eq. (2.1). Specifically, he offered an expression of the form,

$$R = R_0\left[\frac{(1 - n^{4/3})^{1/2}}{n^{1/3}}\right], \tag{A.6}$$

where,

$$n \equiv \frac{M}{(\mu m_\mu)N_0} \,, \tag{A.7}$$

$$N_0 \equiv \frac{(3\pi^2\zeta)^{1/2}}{\nu^{3/2}}\left[\frac{hc}{2\pi G(\mu m_\mu)^2}\right]^{3/2} = \frac{\mu_e^2 m_p^2}{(\mu m_\mu)^3}\left[\frac{4\pi\zeta}{m_3^2\nu^3}\right]^{1/2}M_{\text{ch}} \,, \tag{A.8}$$

$$R_0 \equiv (3\pi^2\zeta)^{1/3}\left[\frac{h}{2\pi m_e c}\right]N_0^{1/3} = \frac{(\mu_e m_p)}{(\mu m_\mu)}\left[\frac{4\pi\zeta}{\nu}\right]^{1/2}\ell_1 \,, \tag{A.9}$$

m_μ is the atomic mass unit (see Table B.1), μ is the mean molecular weight of the gas, and ζ and ν are two adjustable parameters in Nauenberg's analytic approximation, both of which are expected to be of order unity. By assuming that the average particle mass denoted by Chandrasekhar (1967) as $(\mu_e m_p)$ is identical to the average particle mass specified by Nauenberg (1972) as (μm_μ) and, following Nauenberg's lead, by setting $\nu = 1$ and[*],

$$\zeta = \frac{m_3^2}{4\pi} = 0.324142 \,, \tag{A.10}$$

in Eq. (A.8) we see that,

$$(\mu m_\mu)N_0 = M_{\text{ch}} \,. \tag{A.11}$$

---

[*]Actually, Nauenberg (1972) sets $\zeta = 0.323$.

Hence, the denominator in (A.7) becomes the Chandrasekhar mass. Furthermore, expressions (A.9) and (A.6) become, respectively,

$$\mu_e R_0 = m_3(\ell_1 \mu_e) = 1.55686 \times 10^9 \text{ cm},$$
(A.12)

and,

$$R = R_0 \left\{ \frac{[1 - (M/M_{\text{ch}})^{4/3}]^{1/2}}{(M/M_{\text{ch}})^{1/3}} \right\}.$$
(A.13)

Finally, by adopting the values of $M_\odot$ and $R_\odot$ listed in Table B.1, we obtain essentially[†] the identical approximate, analytic mass-radius relationship for ZTWDs presented in Eqs. (27) and (28) of Nauenberg (1972):

$$\frac{R}{R_\odot} = \frac{0.0224}{\mu_e} \left\{ \frac{[1 - (M/M_{\text{ch}})^{4/3}]^{1/2}}{(M/M_{\text{ch}})^{1/3}} \right\},$$
(A.14)

where,

$$\frac{M_{\text{ch}}}{M_\odot} = \frac{5.742}{\mu_e^2}.$$
(A.15)

A.0.3 The "Eggleton" Mass-Radius Relationship

Verbunt & Rappaport (1988) introduced the following approximate, analytic expression for the mass-radius relationship of a "completely degenerate ... star composed of pure helium" (*i.e.*, $\mu_e = 2$), attributing its origin to Eggleton (private communication):

$$\frac{R}{R_\odot} = 0.0114 \left[\left(\frac{M}{M_{\text{ch}}} \right)^{-2/3} - \left(\frac{M}{M_{\text{ch}}} \right)^{2/3} \right]^{1/2} \left[1 + 3.5 \left(\frac{M}{M_p} \right)^{-2/3} + \left(\frac{M}{M_p} \right)^{-1} \right]^{-2/3},$$
(A.16)

where M_p is a constant whose numerical value is $0.00057 M_\odot$. This "Eggleton" mass-radius relationship has been used widely by researchers when modeling the evolution of semi-detached

---

[†]The numerical coefficients that appear here in Eqs. (A.14) and (A.15) differ slightly from the ones presented in Eqs. (27) and (28), respectively, of Nauenberg (1972) presumably because the values of the physical constants — such as $M_\odot$ and $R_\odot$ — that we have adopted in this paper (see Table B.1) are slightly different from the values adopted by Nauenberg.

binary star systems in which the donor is a ZTWD. Since the Nauenberg (1972) mass-radius relationship (A.14) is retrieved from Eq. (A.16) in the limit $M/M_p \gg 1$, it seems clear that Eggleton's contribution was the insertion of the term in square brackets involving the ratio M/M_p which, as Marsh et al. (2004) phrase it, "allows for the change to a constant density configuration at low masses (Zapolsky & Salpeter, 1969)." Here we have only constructed binary star systems in which the internal structure of both stars is governed by the ZTWD equation of state (2.1). Hence it is appropriate for us to compare the properties of our modeled systems to behaviors predicted by the "Nauenberg," not the "Eggleton," mass-radius relationship.

Appendix B: Physical Constants

Table B.1. Physical Constants

Constants[a] (1)	This Paper[b] (2)	Chandrasekhar (1967)[c] (3)
c (cm s^{-1})	$2.99792 \times 10^{+10}$	2.9978×10^{10}
h (erg $\cdot$ s)	6.62608×10^{-27}	6.62×10^{-27}
m_e (g)	9.10939×10^{-28}	9.105×10^{-28}
m_p (g)	1.67262×10^{-24}	1.672×10^{-24}
m_μ (g)	1.66054×10^{-24}	$\cdots$
G (cm^3 g^{-1} s^{-2})	6.6726×10^{-8}	6.62×10^{-8}
$M_\odot$ (g)	1.9891×10^{33}	1.985×10^{33}
$R_\odot$ (cm)	6.955×10^{10}	6.951×10^{10}
A (dynes cm^{-2})	6.00228×10^{22}	6.01×10^{22}
$B\mu_e^{-1}$ (g cm^{-3})	9.81011×10^5	9.82×10^5
$\ell_1 \mu_e$ (cm)	7.71395×10^8	7.705×10^8

[a]Speed of light, c; Planck's constant, h; mass of the electron, m_e; mass of the proton m_p; atomic mass unit, m_μ; universal gravitational constant, G; solar mass, $M_\odot$; solar radius, $R_\odot$; as used in the ZTWD equation of state (2.1), $A = \pi m_e^4 c^5 / 3h^3$ and $B\mu_e^{-1} = 8\pi m_e^3 c^3 m_p / 3h^3$; the characteristic WD length scale, $\ell_1 \mu_e = (2A/\pi G)^{1/2}(\mu_e/B)$.

[b]Drawn from Cox (2000).

[c]Drawn from Appendix I, Table 32 of Chandrasekhar (1967).

Appendix C: List of Variables

Table C.1. List of Variables

Variable	Definition
A_m	Angular momentum density
a	Separation of binary
a_{crit}	Separation of binary at which one star overfills its Roche lobe
C	Bernoulli constant
c_p	Specific heat
c_s	Speed of sound
E	Energy Density
E_b	Binding energy of a star
E_{deg}	Energy density from electron degeneracy
E_K	Kinetic energy density
E_{orb}	Kinetic energy of 2 point mass stars in a circular orbit
E_{pm}	Binding plus kinetic energy for 2 point mass stars in a circular orbit
E_{tot}	Total energy
F	Negative of the effective potential
f_{RL}	Ratio of the volume of a star to its Roche lobe volume
H	Enthalpy per unit mass
I	Moment of inertia
J_{pm}	Angular momentum of 2 point masses in a circular orbit
J_{ss}	Angular momentum of 2 synchronously rotating spheres in a circular orbit
J_{spin}	Angular momentum in the rotation of the star
J_{tot}	Total angular momentum
K	Kinetic energy
k	Radius of gyration
ℓ	Ratio of the radius of the donor to binary seperation
M_1	Mass of the accretor
M_2	Mass of the donor
M_{ch}	Chandrasekhar mass limit
M_{tot}	Total mass of the system
$M_\odot$	Solar Mass
n	Polytopic index
N_z	Number of grid cells in the vertical dimension
N_θ	Number of grid cells in the azimuthal dimension
N_ϖ	Number of grid cells in the radial dimension
P	Pressure
P_{deg}	Degeneracy pressure
P_{gas}	Ideal gas pressure
Q	Effective energy released in a nuclear reaction
q	Ratio of donor mass to accretor mass
R	Radius
R_1	Radius of the accretor

Table C.1.   - Continued

Variable	Definition
R_2	Radius of the donor
$R_\odot$	Solar radius
r	Spherical radial coordinate
$\vec{r}$	Position vector
$\vec{r}_1$	Position vector from the center of mass of the accretor
$\vec{r}_2$	Position vector from the center of mass of the donor
$\Re$	Gas Constant
S_m	Radial momentum density
T	Temperature
T_m	Vertical momentum density
t	Time
U	Internal energy
V	Volume
VE	Virial error
$\vec{v}$	Velocity
W	Gravitational potential energy
x	Dimensionless parameter, $\left(\frac{\rho}{B}\right)^{1/3}$
X	Mass fraction of an element
X_m	Mass fraction of elements heavier than helium
Z	Cylindrical vertical coordinate
γ	Ratio of specific heats
ϵ	Nuclear energy generation rate
η	Fractional probability of a given channel in a nuclear reaction
θ	Cylindrical azimuthal coordinate
κ	Polytropic constant
μ	Mean molecular weight
μ_e	Ratio of nucleons to electrons
Π	Globally averaged pressure
ρ	Mass density
ρ_p	Density cut-off for calculating the ideal gas pressure
ρ_*	Maximum density of the donor
τ	Entropy Tracer
Φ	Gravitational potential
Φ_{eff}	Effective potential in the rotating frame
Φ_R	Roche potential
Ω	Binary orbital frequency
Ω_k	Kepler frequency
ϖ	Cylindrical radial coordinate
ϖ_*	Distance from the outer edge of the donor to the center of mass of the system

Appendix D: Letter of Permission

Before your article can be published in an American Astronomical Society (AAS) journal, we require you to grant and assign the entire copyright in it to the AAS. The copyright consists of all rights protected by the copyright laws of the United States and of all foreign countries, in all languages and forms of communication, including the right to furnish the article or the abstracts to abstracting and indexing services, and the right to republish the entire article in any format or medium. In return, the AAS grants to you the non-exclusive right of republication, subject only to your giving appropriate credit to the journal in which your article is published. This non-exclusive right of republication includes your right to allow reproduction of parts of your article wherever you wish, and permits you to post the published (PDF) version of your article on your personal web site.

(http://www.iop.org/EJ/journal/-page=extra.3/APJ)

Vita

Wesley Paul Even was born in Gilbertville, Iowa, on September 2, 1980. He earned his bachelor's degree in physics in 2003 from the University of Northern Iowa. In August of 2003, he enrolled at Louisiana State University. He received his master's degree in 2008, and expects to receive his doctoral degree in May 2010.